Michigan Technological University
Digital Commons @ Michigan Tech

Dissertations, Master's Theses and Master's Reports

2017

Search for High-Energy Gamma Rays in the Northern Fermi Bubble Region with the HAWC Observatory

Hugo Alberto Ayala Solares
Michigan Technological University, hayalaso@mtu.edu

Recommended Citation

SEARCH FOR HIGH-ENERGY GAMMA RAYS IN THE NORTHERN FERMI

BUBBLE REGION WITH THE HAWC OBSERVATORY

By

Hugo Alberto Ayala Solares

A DISSERTATION

Submitted in partial fulfillment of the requirements for the degree of

DOCTOR OF PHILOSOPHY

In Physics

MICHIGAN TECHNOLOGICAL UNIVERSITY

2017

This dissertation has been approved in partial fulfillment of the requirements for the

Degree of DOCTOR OF PHILOSOPHY in Physics.

Department of Physics

Dissertation Advisor: *Dr. Petra Huentemeyer*

Committee Member: *Dr. Brian Fick*

Committee Member: *Dr. David Nitz*

Committee Member: *Dr. Iosif Pinelis*

Department Chair: *Dr. Ravi Pandey*

Contents

List of Figures

List of Tables

Preface

The results of this thesis are obtained from data taken with the High Altitude Water Cherenkov (HAWC) Gamma-Ray Observatory. It is a collaboration between more than 100 scientists and engineers from institutions in the United States and Mexico. The time offset analysis and the core reconstruction analysis using a NKG function in Chapter 4, as well as the analyses and results in Chapters 5 and 6, are my original work with the help of many collaborators.

Results of chapter 5 have been submitted to the Astrophysical Journal as "Search for Very High Energy Gamma Rays from the Northern *Fermi* Bubble Region with HAWC"[11].

Acknowledgments

A mi madre, padre y hermanos: Gracias por el apoyo incondicional que siempre me han dado y por apoyarme en mi sueño de convertirme en un científico. Los amo.

To my thesis advisor, Petra Huentemeyer, for giving me the opportunity to work on the HAWC collaboration since my undergraduate program. Thank you for all the advices and for sharing your experiences as a scientist. Thank you also for sharing some time with me to watch the World Cups.

Thank you to my undergraduate advisors, Alfonso Serrano, Raul Hernandez and Julio Gutierrez for their advices, help and opportunities on doing research.

To Michelle Hui and Hao Zhou. Thank you for sharing your knowledge and the help you gave me when I had problems with my analysis.

Thanks to the members of HAWC Collaboration. Thank you Robert Lauer and Francisco Salesa for working together in the Calibration Group. Thank you John Pretz, for helping me understand the HAWC software and the reconstruction algorithms. Thank you Segev BenZvi, for helping me with the data challenge code and for all your Python tips. Thank you Dan Fiorino, for helping me understand the background estimation and proofreading my work and analysis. Thank you also to Brenda Dingus,

Abstract

Gamma-ray astronomy is the study of very energetic photons, from $E = m_e c^2 \approx 0.5 \times 10^6 \,\text{eV}$ to $\geqslant 10^{20} \text{eV}$. Due to the large span of the energy range, the field focuses on non-thermal processes that include the acceleration and propagation of relativistic particles, which can be found in extreme environments such as pulsars, supernova remnants, molecular clouds, black holes, etc.

The High Altitude Water Cherenkov (HAWC) observatory is an instrument designed for the study of gamma rays in the energy range of $\sim 100\,\text{GeV}$ to $100\,\text{TeV}$. Using data from the HAWC observatory, a study for the search of very high energy gamma rays in the northern *Fermi* Bubble region was made. The *Fermi* Bubbles are large extended regions in the gamma-ray sky located above and below the galactic plane that present a hard emission between $1\,\text{GeV}$ and $100\,\text{GeV}$. No significant excess is found an upper bounds at 95% C.L. are obtained. The implications of this result are that certain processes explaining the Fermi Bubble formation from the center of our galaxy are excluded. I will discuss and compare the scenarios that still present a possible hypothesis of the Fermi Bubble origin.

Chapter 1

Gamma-Ray Astrophysics: The High-Energy Universe

1.1 Introduction

The study of astrophysics relies to a large degree on the observation of the electromagnetic spectrum. This spectrum covers a sizable range of energies, going from $>1\,\mathrm{peV}$ to $>\mathrm{TeV}$. Depending on the place in the electromagnetic spectrum, the radiation receives a different name as seen in Figure 1.1.

Traditional astronomy observes the radiation from ultraviolet, visible, infrared and x-rays. These forms of radiation are produced, mainly, by hot objects (e.g. stars)
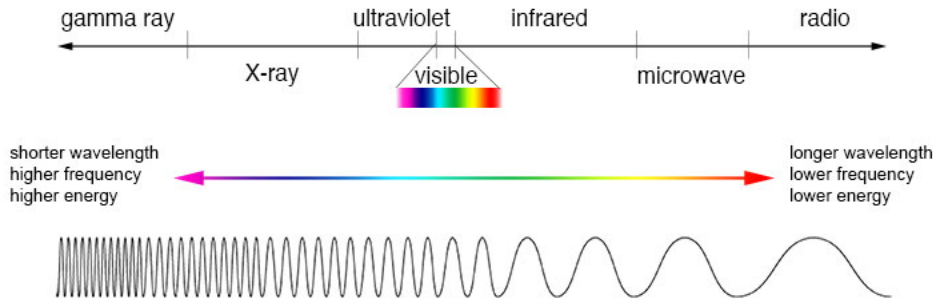
Figure 1.1: Electromagnetic spectrum. Gamma rays are the highest energy photons, while radio waves are the lowest. Visible light corresponds to a small part of the range in the electromagnetic spectrum. (Credit: NASA's Imagine the Universe)

and are described by the blackbody radiation:

$$F = \frac{2hc^2}{\lambda^5} \frac{1}{e^{hc/\lambda kT} - 1} \tag{1.1}$$

where λ is the wavelength of the photon, T is the temperature of the blackbody, k is the Boltzmann constant, h is the Planck constant, c is the speed of light and F is the photon flux. This is defined as thermal emission, since the radiation depends on the temperature of the object. In extreme environments, thermal emission can produce photons in the keV range. However, the production of high energy photons of >GeV requires non-thermal processes. These processes produce radiation through collision of particles, decay of particles or acceleration of particles. The detection of these highly energetic photons gave rise to a new field in astronomy in the 1960s.

Gamma ray astrophysics is one of the most recent research areas in astronomy. It studies photons that span over 14 decades of energy, from $E = m_e c^2 \approx 0.5 \times 10^6 \, \text{eV}$

to $\geqslant 10^{20}$ eV. The consequence of this broad energy range is reflected in a the great variety of topics, related to non-thermal processes including the acceleration and propagation of relativistic particles. Gamma-ray astronomy provides a new window to test fundamental physics that cannot be studied with the current particle accelerators on Earth. This is because gamma rays are produced in extreme physical conditions, such as shock waves, environments with huge gravitational and electromagnetic fields, turbulent plasmas, etc.

The study of gamma rays is divided depending on the energy of the photon. By definition, a low energy (LE) gamma-ray photon is of the order of MeV, a high energy (HE) photon has an energy of GeV, while a very high energy (VHE) photon has an energy of TeV [12]. The focus of this thesis is on the HE and VHE gamma-ray photons.

1.2   Gamma-Ray Production Mechanism

1.2.1   Cosmic-Ray Acceleration

One of the most important features of gamma-ray astronomy is that it is a link to another field of astrophysics: cosmic rays. Cosmic rays are relativistic particles, that can be accelerated to high energies in really extreme environments in the universe.

The acceleration of charged particles is described by the Lorentz Force equation:

$$\frac{d}{dt}(\gamma m \mathbf{v}) = q(\mathbf{E} + \mathbf{v} \times \mathbf{B}), \tag{1.2}$$

where q is the charge of the particle moving with velocity $\mathbf{v}$ inside an electric field $\mathbf{E}$ and magnetic field $\mathbf{B}$; m is the mass of the particle and γ is the Lorentz factor.

In most astrophysical environments and plasmas, Coulomb interactions are negligible and work done on the particles is mainly done by time-varying magnetic and electric fields. In plasmas, the former is dominant.

One of the main mechanisms for particle acceleration is called *diffusive shock acceleration* [13]. This process, also known as first-order Fermi acceleration, involves the propagation of strong shock waves through interstellar medium. The shocks are non-linear disturbances that transfer energy and momentum to particles through plasma processes.

Due to instabilities in the medium and in the magnetic fields in both sides of the shock, cosmic rays can cross the shock several times. In each crossing time or collision, the particles average energy after the collision is $\langle E \rangle = \beta \langle E_0 \rangle$, with $\langle E_0 \rangle$ being the initial energy of the particles. After k collisions, the average energy is $\langle E \rangle = \langle E_0 \rangle \beta^k$ and the number of particles in the system is described by $N = N_0 P^k$, where N_0 is the initial

number of particles an P is the probability that the particle remains in the system. Combining both equations, the total number of cosmic ray particles above the energy E is

$$\frac{\ln(N/N_0)}{\ln(\langle E \rangle / \langle E_0 \rangle)} = \frac{\ln P}{\ln \beta}. \tag{1.3}$$

Inverting this function results in an integrated value of the number of particles.

$$\frac{N(\geq E)}{N_0} = \left(\frac{E}{E_0} \right)^{\ln P / \ln \beta}. \tag{1.4}$$

Differentiated with respect to the energy gives

$$N(E)\, dE \propto E^{-1 + \ln P / \ln \beta}\, dE. \tag{1.5}$$

This power-law distribution is the main feature of a non-thermal process. To get an idea of the values of P and β we assume that the shock is a strong shock, which means that the speed of the shock front is supersonic, $U \gg c_s$, where c_s is the speed of sound in the interstellar medium. We also assume that the gas is ideal and that the shock front is thin (Figure 1.2). The downstream is the region where the gas has been shocked; the upstream is the region where the shock has not interact with the gas.

From the reference frame of the shock front, the upstream region approaches the
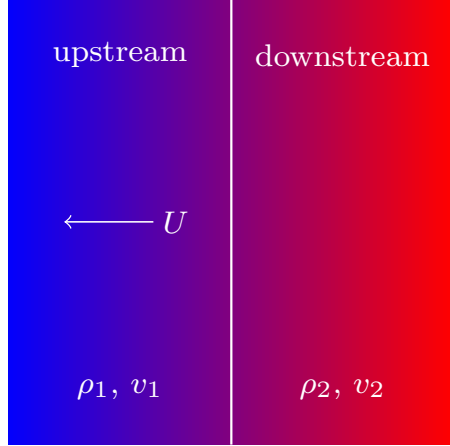
Figure 1.2: Schematic of a shock front where particle acceleration occurs. The shock front is represented as the white line and moves with speed U.

shock with speed $|U|$. Since the mass is conserved, the continuity equation in the shock front is applied:

$$\rho_1 v_1 = \rho_2 v_2, \tag{1.6}$$

where ρ_1, ρ_2 are the densities for the upstream and downstream, respectively; and v_1, v_2 are the velocities of the interstellar medium in the upstream and downstream.

Due to the previous assumptions, $\rho_2/\rho_1 = (\gamma + 1)/(\gamma - 1)$, and for a monatomic gas $\gamma = 5/3$. This means that $\rho_2/\rho_1 = 4$ or $v_2 = v_1/4 = U/4$.

From the point of view of the upstream, the downstream approaches the shock with speed $|v_1 - v_2| = 3U/4$. The same speed is observed from the point of the downstream of the approaching speed of the upstream. This is the most important part of the process: particles are always having face-on collisions and therefore gaining energy.

The average gain in energy of a particle crossing the shock front in a round trip is:

$$\left\langle \frac{\Delta E}{E} \right\rangle = \frac{4V}{3c},\tag{1.7}$$

where $V = 3U/4$ is the approaching speed of the particle (The change in energy is proportional to the speed, hence the name first-order acceleration). Then the value

$$\beta = \frac{\langle E \rangle}{\langle E_0 \rangle} = 1 + \frac{U}{c}.\tag{1.8}$$

The probability to remain in the system is calculated as follows. The total number of particles crossing the shock front with relativistic velocities is $nc/4$, where n is the number density of particles. In the downstream region, particles are advected away from the shock with speed $U/4$, so the number of particles lost in this region is $nU/4$. The ratio of this two quantities is the probability to escape the system and the probability to remain in the system becomes

$$P = 1 - \frac{U}{C}\tag{1.9}$$

Finally, for non-relativisitic shocks, the logarithm term in equation 1.5 becomes

$$\frac{\ln P}{\ln \beta} = \frac{\ln(1 - U/C)}{\ln(1 + U/C)} \approx -1\tag{1.10}$$

and equation 1.5 becomes

$$N(E)\,dE \propto E^{-2}\,dE. \tag{1.11}$$

This value of the spectral index is typical for regions close to cosmic-ray accelerators (See [13]).

1.2.2 Gamma Rays

Gamma rays are produced by the interaction of high-energy cosmic rays with different media in the universe. Understanding and interpreting the production mechanisms that give rise to gamma radiation is an important key of astrophysical observations. This is because the production mechanisms provide information about the origin, diffusion and propagation of cosmic rays. Charged cosmic rays, after being produced and accelerated, will be deflected by the interstellar magnetic fields as they diffuse and propagate through the galaxy. This prevents us from knowing the sources of cosmic rays since the latter do not point back to their origin. However, if the cosmic rays interact with their environment immediately after being produced, they can generate gamma rays which are not affected by magnetic fields. Hence the acceleration regions of cosmic rays can be investigated by studying gamma-ray observations.

Cosmic rays are hadronic —protons and nuclei— or leptonic —positrons and electrons—, so the gamma-ray production mechanisms are divided in leptonic or

hadronic processes. The processes are also divided by the type of media where the interaction occurs. The interactions can be with matter, radiation fields or magnetic fields. Since the primary cosmic rays follow a power-law spectrum distribution, the gamma-rays will, in general, follow the same distribution.

The main radiation mechanisms in the HE and VHE gamma rays are inverse Compton scattering, bremsstrahlung and decay of neutral pions. These processes are described below. Synchrotron radiation is another radiation mechanism that occurs at LE, when a high-energy electron interacts with magnetic fields. Since the thesis focus on HE and VHE, that process will not be described in detail.

1.2.2.1 Bremsstrahlung

Bremsstrahlung, or braking radiation, occurs when an electron decelerates when it passes near a charged particle or nucleus present in the interstellar gas and matter, giving energy off in the form of a gamma-ray photon.

The average energy loss rate of electrons due to bremsstrahlung is written as:

$$-\left(\frac{dE_e}{dt}\right) = \left(\frac{cm_p n}{X_0}\right) E_e, \tag{1.12}$$

where c is the speed of light, m_p is the mass of the proton, n is the number density
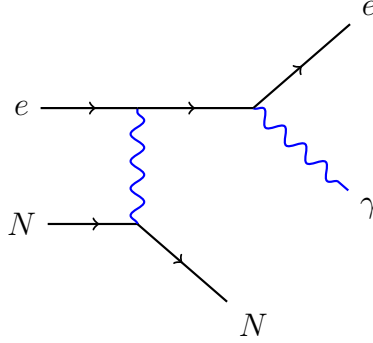
Figure 1.3: Feynman diagram of Bremsstrahlung. The electron interacts with the electric field of a nucleus. It looses energy in the form of a high-energy photon

of the ambient gas, X_0 is the radiation length —Defined as the average distance over which the ultrarelativsitc electron loses all but $1/e$ of its energy— and E_e is the energy of the electron. The radiation length is inversely proportional to the cross section σ_o of the interaction $X_0 = 7/9(n\sigma_o)^{-1}$. Bremsstrahlung causes electrons to have a lifetime of

$$\tau = \frac{E_e}{-dE_e/dt} \approx 4 \times 10^7 (n/\text{cm}^{-3})^{-1}\, yr \qquad (1.13)$$

which is independent of the energy of the electron. With this information, we see that the spectrum of electrons after losing energy through Bremsstrahlung, keeps the shape of the initial power-law spectrum $N_0(E_e)$.

$$N_e \propto \left| \frac{dE_e}{dt} \right|^{-1} \int N_0(E_e) dE_e \qquad (1.14)$$

In the case of relativistic electrons with energy E, they can interact with interstellar gas to produce photons with frequencies up to $\nu = E/h$ with an average energy of

$(1/3)E$.

1.2.2.2   Inverse Compton Scattering

This leptonic process occurs when a relativistic cosmic-ray electron interacts with a low-energy photon, for example from the cosmic background radiation, increasing the energy of the photon and becoming a gamma ray, while the electron loses energy. Figure 1.4 show one of the Feynman diagrams of this process.
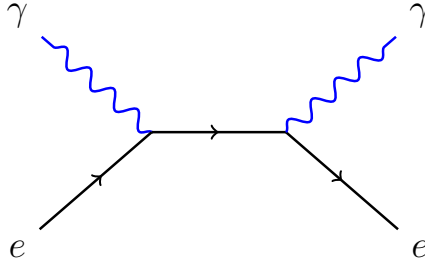
Figure 1.4: Inverse Compton Scattering

The process is governed by the cross section given by the Klein-Nishina formula:

$$\frac{d^2\sigma}{d\Omega d\epsilon} = \frac{3\sigma_T}{16\pi} \left(\frac{\epsilon}{\epsilon_0}\right)^2 \left(\frac{\epsilon_0}{\epsilon} + \frac{\epsilon}{\epsilon_0} - sin^2\theta\right) \times \delta\left[\epsilon - \frac{\epsilon_0}{1 + \epsilon_0(1 - cos\theta)}\right] \qquad (1.15)$$

where σ_T is the Thomson scattering cross section, ϵ is the energy is of the scattered photon in units of $m_e c^2$, ϵ_0 is the energy of the initial photon in units of $m_e c^2$ and θ is the angle of the scattered photon. The total cross section can be obtained by

integrating over all angles and energies of the scattered photon:

$$\sigma = \oint d\Omega \int d\epsilon \frac{d^2\sigma}{d\Omega d\epsilon} = \frac{3\sigma_T}{8\epsilon_0}\left[\left(1 - \frac{2}{\epsilon_0} - \frac{2}{\epsilon_0^2}\right)ln(1+2\epsilon_0) + \frac{1}{2} + \frac{4}{\epsilon_0} - \frac{1}{2(1+2\epsilon_0)^2}\right]$$

(1.16)

At $\epsilon_0 << 1$ the total cross section $\sigma \approx \sigma_T$ and this is referred to as the Thomson limit. When $\epsilon_0 >> 1$ the total cross section reduces to $\sigma \approx \frac{3\sigma_T}{8\epsilon_0}\ln(2e^{1/2}\epsilon_0)$.

Finally, if a isotropic distribution of photons is assumed, the spectrum of scattered photons can be calculated. A detailed description of this calculation is given in [14].

The result of the gamma-ray spectrum is given by

$$\frac{dN}{dtd\epsilon} = \frac{3\sigma_T m_e c^3}{4\gamma}\frac{n(\epsilon_0)}{\epsilon_0}\left[2q\,lnq + (1+2q)(1-q) + \frac{1}{2}\frac{(\Gamma_{\epsilon_0}q)^2}{1+q\Gamma_{\epsilon_0}}(1-q)\right]$$

(1.17)

where $\Gamma_{\epsilon_0} = 4\epsilon_0\gamma/mc^2$ is a dimensionless parameter that defines the domain of the scattering; $q = E/\Gamma_{\epsilon_0}(1-E)$ and E is the energy of the scattered photon.

The result of the spectrum in the Thomson Limit ($\Gamma_{\epsilon_0} << 1$) is

$$\frac{dN}{dtd\epsilon} = \frac{3\sigma_T c}{16\gamma^4}\frac{n(\epsilon_0)}{\epsilon_0^2}\left(2\epsilon\,ln\frac{\epsilon}{4\gamma^2\epsilon_0} + \epsilon + 4\gamma^2\epsilon_0 - \frac{\epsilon^2}{2\gamma^2\epsilon_0}\right)$$

(1.18)

1.2.2.3 Neutral Pion Decay

This process occurs when hadronic cosmic rays collide with interstellar media, produc-
ing among others neutral and charged pions. Neutral pions decay into two gamma-ray
photons. The diagram shown if figure 1.5 shows this process.
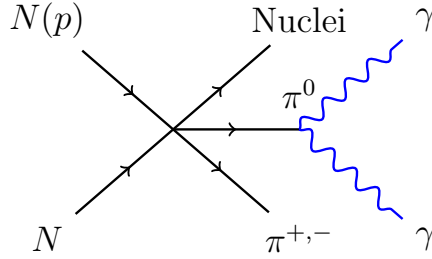
Figure 1.5: Collision of a cosmic ray with another particle. Neutral pions
decay into gamma rays.

The minimum kinetic energy of protons to produce neutral pions should be bigger
than $E_{th} = 2m_\pi c^2(1 + m_\pi/4m_p) \approx 280\,MeV$. The mean lifetime of the pion is
$\tau = 8.4 \times 10^{-17}\,s$. The gamma-ray emissivity depends on the convolution of the
differential cross-section of the interaction of inelastic collisions of protons with a
distribution of protons that are part of the ISM. This emissivity can be written as
follows:

$$q_\gamma(E_\gamma) = 2 \int_{E_{min}}^{\infty} \frac{q_\pi(E_\pi)}{\sqrt{E_\pi^2 - m_\pi^2 c^4}} dE_\pi \tag{1.19}$$

where $E_{min} = E_\gamma + m_\pi^2 c^4/4E_\gamma$, is the threshold pion energy. The emissivity of neutral

pions is given by

$$q_\pi(E_\pi) = c\, n_H \int \delta(E_\pi - \kappa_\pi E_{kin}) \sigma_{pp}(E_p) n_p(E_p) dE_p \qquad (1.20)$$

where n_H is the column density of hydrogen, κ_π is the fraction of the kinetic energy transferred to the pion per collision, σ_{pp} is the total cross section of inelastic pp and $n_p(E_p)$ is the proton spectrum with energy E_p.

1.3 Gamma-Ray Sources

There is a great variety of gamma-ray sources. Depending on their origin, they can be either galactic or extra-galactic. Galactic sources include supernova remnants, pulsars, pulsars wind nebulae, binary objects and large-scale structures like the galactic diffuse emission and the Fermi Bubbles. Extra-galactic sources include active galactic nuclei (AGN), gamma-ray bursts (GRBs) or starburst galaxies. These will be briefly discussed in the following.

1.3.1 Supernova Remnants

When a massive star $(M_* \gtrsim 8 M_\odot)$ goes through the end of its stellar evolution, it undergoes a powerful explosion, called a supernova. The explosion releases an energy

of the order $\sim 10^{44}$ J. This explosion last for an interval time of the order of seconds, but the expansion of the material from the dead star will continue up to $\sim 30,000$ of years, before the material merges with the interstellar media.

One of the main hypothesis in gamma-ray astronomy is that particle acceleration in supernova remnants is the main contribution to the cosmic rays present in the Galaxy. Ten percent of the energy of the supernova explosion is expected to be used to accelerate cosmic rays to high energies, as previously mentioned in section 1.2.1. These accelerated particles will interact with the surrounding media producing gamma rays.

The Crab Nebula is one of the most important supernova remnants in gamma-ray astronomy. This remnant exploded around the year 1054 and was registered by Chinese astronomers. It is still one of the brightest objects in gamma rays today and it is used as the standard candle for the field of gamma-ray astronomy.

1.3.2 Pulsars and Pulsar Wind Nebulae

In 1967, Jocelyn Bell was working on her PhD to study the scintillation in the solar wind produced by the interaction of radio waves from extragalactic sources (called quasars) with the wind. In her data she found a series of regularly spaced pulses 1.337 seconds apart. It was the first detection of a new phenomena and received the
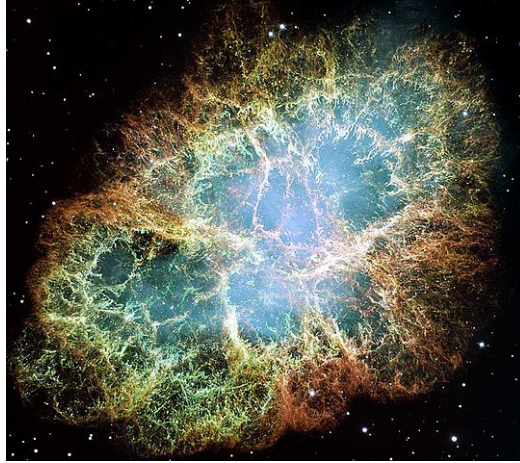
Figure 1.6: Crab Nebula seen by the Hubble Telescope. It is composed by
a supernova remnant, pulsar wind nebula and the pulsar. Credit: NASA

name of pulsar [15]. After a massive star goes supernova, the left-over of the star can
become a pulsar: a rapidly rotating neutron star with a strong dipole magnetic field.
The rotating magnetic field induces an electric field, which can accelerate particles to
high energies. The magnetic field can produce emission through synchroton radiation
when high energy electrons travel through it. The pulsar wind nebula is formed when
the accelerated particles produced by the pulsar interact with their sorroundings.
These particles, in the form of a wind, can produce shocks when interacting with
the interstellar medium and are able to accelerate particles up to PeV energies. The
electrons lose energy through synchrotron radiation or inverse Compton scattering.
Figure 1.6 shows a picture of the Crab Nebula.

1.3.3 Binary Systems

Most of the star-system found in the galaxy are composed of more than one star. A few of this systems are able to emit in high-energy gamma rays. In these few cases, the system consists of a compact object —such as a neutron star or black hole— and a massive star. In general, the gravity from the compact object pulls matter from the companion star. Particle acceleration occurs either by a relativistic jet, or by a pulsar wind colliding with stellar wind, which then causes non-thermal emission. Five binary systems have been detected in the VHE gamma-ray regime [16]. The binaries are PSR B1250-63 [17], LS 5039 [18], LS I +61º303 [19], HESS J0632+057 [20] and 1FGL J1018.6-5856 [21].

1.3.4 Large Extended Sources

1.3.4.1 Diffuse Emission

The galactic diffuse gamma-ray emission is the gamma-ray radiation produced by the interaction of leptonic and hadronic cosmic rays with the interstellar gas and photon fields [22, 23]. The production of gamma rays from pion decay and bremsstrahlung depend on the distribution of gas in the galaxy. Gamma rays from inverse Compton

scattering are formed by the interaction of electrons with photon fields such as the cosmic microwave background radation (CMBR) or the interstellar light. Studying the diffuse emission allows to probe the distribution and propagation of cosmic rays in our galaxy. At energies between $200\,\mathrm{MeV}$ and $100\,\mathrm{GeV}$, the diffuse emission constitutes the principal component of the gamma-ray sky. At higher energies, in the TeV-range, resolved and unresolved sources dominate the gamma-ray flux. The main processes at these VHEs are pion decay and inverse Compton scattering.

1.3.4.2 Giant Molecular Clouds

Giant Molecular Clouds can be considered a subset of Diffuse Emission. They provide the material which leptonic and hadronic cosmic rays can interact with and produce gamma rays. One of the current hypothesis is that the cosmic-ray spectrum measured at Earth is a representative measurement of the cosmic-ray flux in the whole Galaxy. Studying the spectral energy distribution of gamma rays emitted by Molecular Clouds (MCs) is a way to probe this hypothesis and to measure the distribution of cosmic rays in distant parts of the Galaxy[24, 25]. A preliminary analysis of potential emission from MCs will be discussed in chapter 6.

1.3.4.3   Fermi Bubbles

In 2010, two large bubble-like structures above and below the galactic center in the data from the Fermi LAT Telescope were discovered [26, 27] (See chapter 2 for brief description of the Fermi Telescope). Since then, many studies and simulations have tried to understand their origin and the gamma-ray production mechanisms. More information and an analysis to search for VHE gamma rays from the Northern Fermi Bubble Region is presented in chapter 5.

1.3.5   Extra-galactic Sources

Gamma-ray production not only occurs in our Galaxy. Active galactic nuclei (AGN) are galaxies with a central nucleus that is brighter than the rest of the galaxy. Radio observations of this objects have shown evidence of collimated jets from the center of the galaxy. They are formed by relativistic charged particles. These particles produce emission in non-thermal processes. AGNs with jets that are coincidentally pointed at the Earth are extremely bright at all wavelengths, from radio to gamma rays, due to Doppler beaming. These types of AGN are known as blazars. Other types of AGNs are radio galaxies —the jets are perpendicular with respect of the line of view from Earth— and starburst galaxies —which are galaxies wtih high star-rate formation.

Other type of extra-galactic sources are gamma-ray bursts (GRBs). These are extreme energetic explosions produced in distant galaxies. The bursts can last ten milliseconds to several hours. Detection of GRBs has been done over the whole electromagnetic spectrum [28].

This thesis is focused on the study of VHE gamma rays from extended regions in our galaxy such as the Fermi Bubbles and Giant Molecular Clouds. Chapter 2 describes the detection techniques used in gamma-ray astronomy. Chapter 3 discusses the HAWC observatory and its hardware. Chapter 4 explains the HAWC data and the methods used to reconstruct gamma-ray events. Chapters 5 and 6 show the analysis and preliminary results from the search for VHE gamma rays in large extended regions in the Galaxy. The conclusions are presented in chapter 7.

Chapter 2

Detection of Gamma Rays

As mentioned in chapter 1, gamma-ray astronomy spans a large energy domain in the electromagnetic spectrum, covering 14 orders of magnitude in the energy range from 1×10^6 eV to $\geq 1 \times 10^{20}$ eV. Because of this large energy range, different detection techniques had to be developed to study gamma rays. This chapter describes some of the techniques used for the observation of gamma rays. The techniques are separated into two main groups, space-based telescopes and ground-based observatories.

2.1 Space-Based Telescopes

Observation of gamma rays started in the 1960s, when the technology was developed to send a gamma-ray telescope into orbit. The Explorer 11 satellite was launched in 1961 and it observed the first gamma-ray photons coming from all directions [29].

It was not until the launch of the Small Astronomy Satellite 2 (SAS-2) in 1972 [30] and the COS-B satellite [31] in 1982 that the field of gamma-ray astronomy was born. The SAS-2 satellite detected around ~8000 gamma rays from the sky, making the first identifications of gamma rays coming from sources like the Crab and Vela pulsars, Geminga and the Cygnus region [12]. The COS-B satelite was able to detect ~200000 gamma-ray photons. It discovered 25 sources, most of them in the Galactic Plane. By the late 1960s and 1970s, the Vela satellites, designed to look for nuclear bomb blasts, discovered the existence of Gamma-Ray Bursts.

In 1991, NASA launched the Compton Gamma Ray Observatory (CGRO), which carried four major instruments. One of these instruments was the Energetic Gamma Ray Experiment Telescope (EGRET). It was designed to be sensitive to gamma rays in the energy range of $20\,\mathrm{MeV}$ to $30\,\mathrm{GeV}$. It consisted of a gas-filled spark chamber, which main function was to track the gamma-ray photon after it converted to an
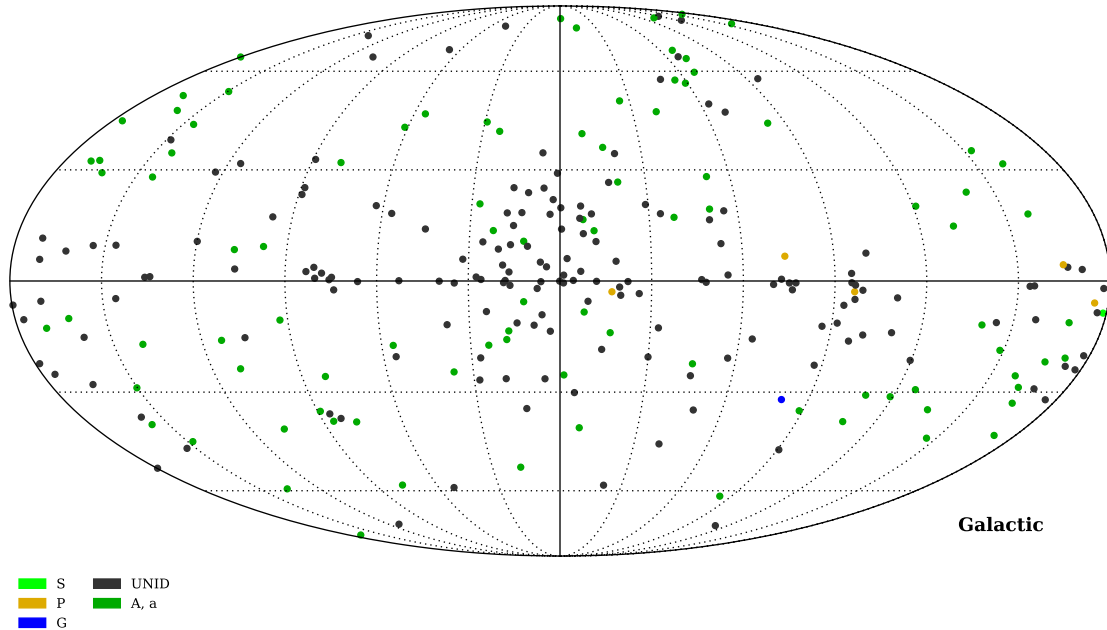
Figure 2.1: EGRET Catalogue. Labels: S-Solar Flare; P-Pulsar; G-Galaxy; A,a- Active Galactic Nuclei; UNID-Unidentified. [1]

electron-positron pair. An anti-coincidence chamber was used to veto charged particles. CGRO was de-orbited in 2000 due to a failure in its stabilizing mechanism. EGRET was able to observe 271 sources above an energy of E>100 MeV [1]. Figure 2.1 shows the sources discovered by EGRET.

The Fermi Gamma-Ray Telescope was launched on August 26th, 2008. It is the most sensitive instrument in space to detect gamma rays. It consists of two different detectors, the Large Area Telescope (LAT) and the Gamma-ray Burst Monitor (GBM).

The LAT has a $\sim 1\,\mathrm{m}^2$ aperture and it is sensitive to gamma rays between $20\,\mathrm{MeV}$ and $\gtrsim 500\,\mathrm{GeV}$. The telescope uses pair conversion to observe and reconstruct the direction of gamma rays. It has a calorimeter to measure the energy of the photon that consists of 1536 CsI(Tl) crystals, arranged in eight alternating orthogonal layers, of 96 crystals. And it is also provided with an anti-coincidence detector of 89 plastic scintillator tiles, which detects charged cosmic rays by observing the flash of light they generate when traversing the detector. It can scan the full sky in 3 hours with a field of view of 2sr. The energy resolution is $< 10\%$. The angular resolution goes from $3.5°$ at $300\,\mathrm{MeV}$ to $< 0.15°$ at $>10\,\mathrm{GeV}$. Figure 2.2 show the third Fermi-LAT catalogue with a total of 3033 sources [2].

The difference between Figures 2.1 and 2.2 is notable, reflecting the sensitivity improvement of the detection methods in less than 20 years.

Despite the fact that the technology for space-based telescopes has improved significantly -providing large field of view, great angular and energy resolution- the effective area is still restricted to $\lesssim 1\,\mathrm{m}^2$. This has limited the observation of gamma rays up to TeV energies. Instruments with larger effective area are required to observe gamma rays with higher energies.
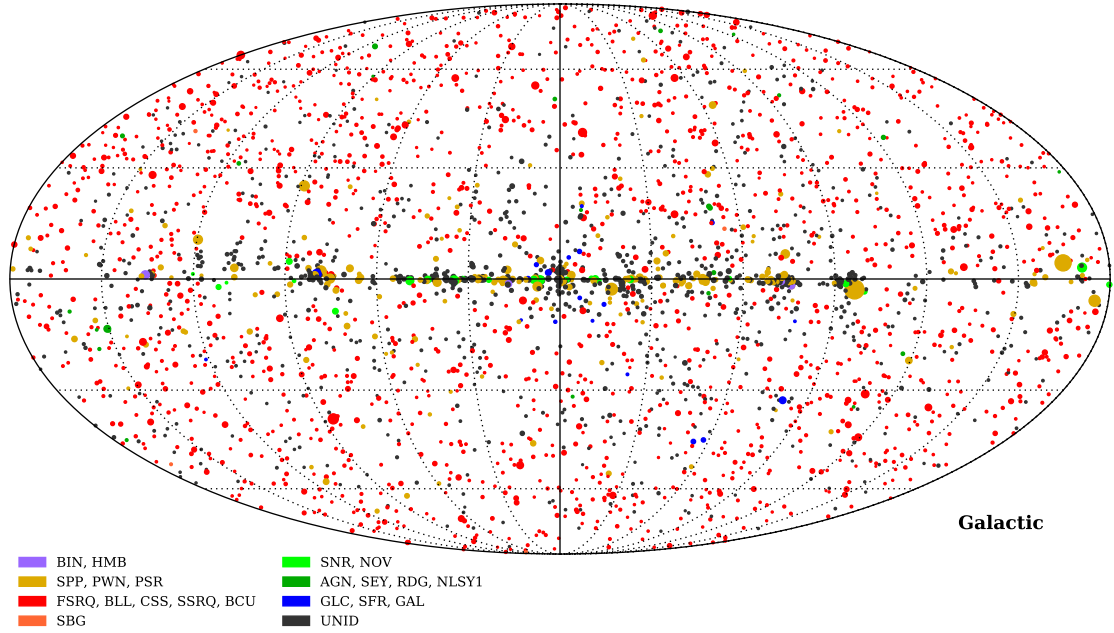
Figure 2.2: Fermi 3FGL Catalogue. Labels: BIN-Binary; HMB-High Mass Binary; PWN-Pulsar Wind Nebula; PSR-Pulsar; SPP-Supernova Remnant/PWN; FSRQ,BLL,CSS,SSRQ,BCU-Types of Blazars; SBG-Starburst Galaxy; SNR-Supernova Remnant; NOV-Nova; AGN-Active Galactic Nuclei; SEY-Seyfert Galaxy; RDG-Radio Galaxy; NLSY1-Narrow-line Seyfert 1;GLC-Globular Cluster; SFR-Star-forming Region; GAL-Galaxy; UNID-Unidentified. [2]

2.2   Ground-Based Observatories

Gamma rays do not penetrate the atmosphere of Earth. However, an indirect detection is possible by using the atmosphere as part of the detector. When high energy particles penetrate the atmosphere of Earth, they interacting with the gas molecules and produce a so-called extensive air shower. The detection of these extensive air

showers is the objective of the ground-based observatories.

2.2.1 Extensive Air Showers

The way a high energy particle deposits its energy in Earth's atmosphere is by produc-
ing secondary particles. Secondary particles are produce by the several mechanisms,
mainly bremsstrahlung and pair production. The continuous production of secondary
particles through the atmosphere is called an extensive air shower (EAS).

Pair production consists of the energy conversion of a photon into an electron-positron
pair in the presence of a nucleus. The photon energy has to be larger than the sum of
the rest-mass energies of electron and positron $E = 2(0.511\,\text{MeV}) = 1.022\,\text{MeV}$. The
radiation length of bremsstrahlung in the atmosphere is $X_0 = 37.15\,\text{g}\,\text{cm}^{-2}$, which is
7/9 of the free mean path of pair production. This is the distance that an electron
will travel before losing all but $1/e$-th of its energy [32]. The total vertical thickness
of the atmosphere above sea level is of $1030\,\text{g}\,\text{cm}^{-2}$. This means there are 28 radiation
lengths in the atmosphere [33].

EAS can be initiated by hadronic cosmic rays or by gamma rays and electrons.
Bremsstrahlung and pair production are the main processes for gamma-ray/electron
showers. In the case of hadronic EAS, the high energy cosmic ray will also interact
through collisions with particles in the atmosphere producing pions, muons, kaons,

neutrinos and other types of particles. These particles will spread the air shower more before becoming a purely electromagnetic shower.

There are main differences between a gamma-ray initiated shower and a cosmic-ray initiated shower. In general, a gamma-ray shower is more compact than a cosmic-ray shower. This is because the transverse momenta of the secondary particles in the collisions of cosmic rays with particles in the atmosphere is higher than the transverse momenta of the secondary particles in the electromagnetic processes. Gamma-ray showers also have a low content of muons, —only about a percent of that found in hadron induced showers— a feature that is used to identify the type of showers[34].

Simulated particle tracks in a cosmic-ray shower and a gamma-ray shower are shown in Figure 2.3.

The number of secondary particles increases as the shower progresses through the atmosphere. When the average energy of the secondary electrons drops below $E_c \sim 80 \, \text{MeV}$, the cross section for ionization losses starts to be greater than that for Bremsstrahlung. This occurs at a maximum depth of $X_{max} = X_0 \ln\left(\frac{E}{E_c}\right)/\ln 2$. This is when the maximum number of secondary particles are produced. For a TeV gamma ray shower, this occurs at 5-10km.

There are two techniques that are used for the detection of extensive air showers produced by gamma rays. The techniques are Imaging Air Cherenkov Telescopes and
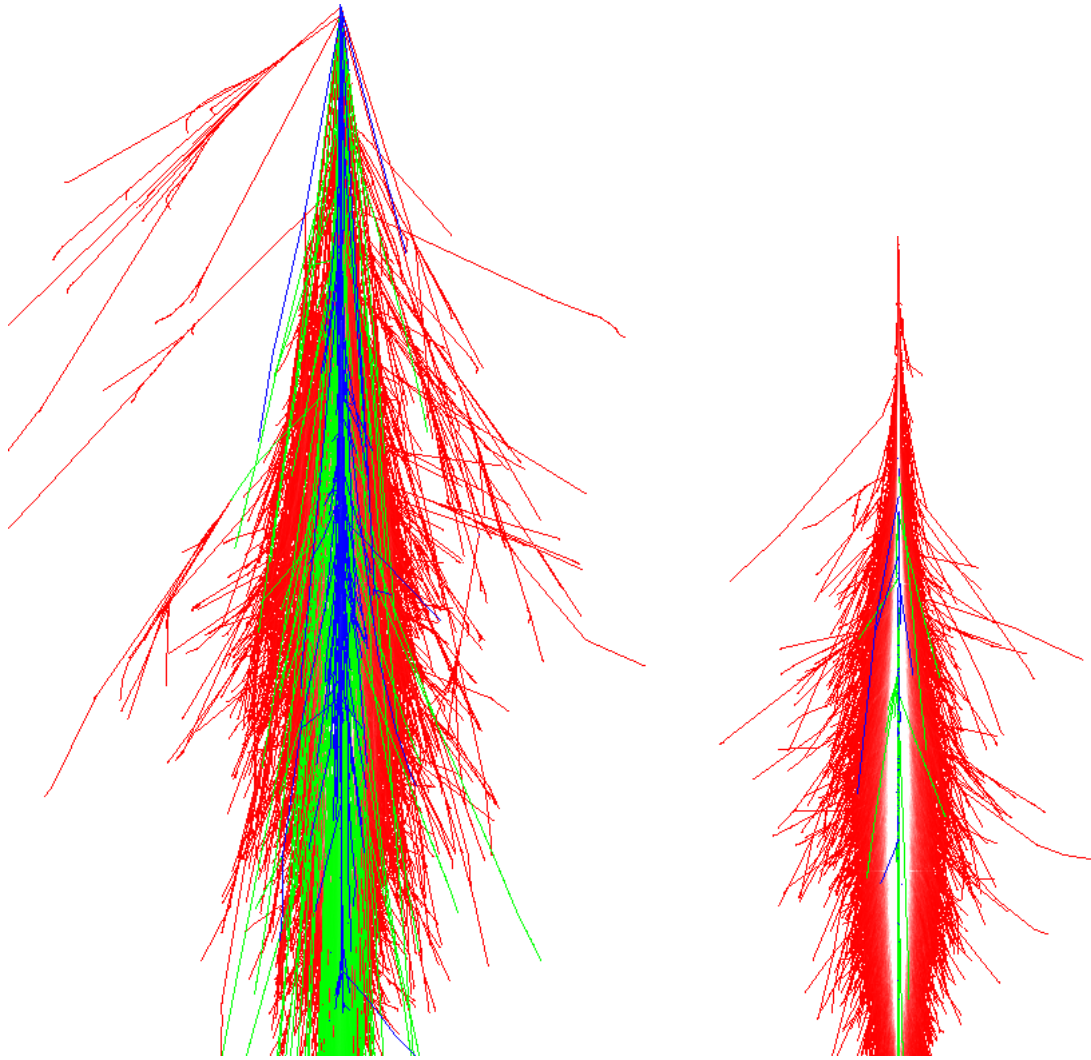
Figure 2.3: Examples of 10TeV proton and photon showers. Red tracks represent the electromagnetic components (photons, electrons and positrons). Green is the muon component. Blue is the hadronic component. CORSIKA software was used to make these plots [3]

EAS Arrays.

2.2.2 Imaging Air Cherenkov Telescopes

Cherenkov Radiation is an electromagnetic phenomenon that occurs when charged particles travel faster than the speed of light in a dielectric medium. This means that

$$\frac{c}{n} < v_{particle} < c \tag{2.1}$$

where n is the index of refraction of the dielectric medium. Figure 2.4 shows a schematic of Cherenkov Radiation. The lights is represented by the blue cone.

For example, in water, light travels at a speed of $0.75c$; while in air light travels at a speed close to its value in vacuum. Particles traveling faster than this speed will produce Cherenkov light. The particle produces an electromagnetic shock wave while traversing the medium as shown in figure 2.4. The emission cone has an opening angle given by

$$cos\,\theta = \frac{c}{n\,v_{particle}}. \tag{2.2}$$

Taking advantage of the Cherenkov radiation, Imaging Air Cherenkov Telescopes (IACTs) have been designed to detect this radiation in the atmosphere. These observatories are composed of an array of optical telescopes. The telescopes are typically $\geq 10\,\mathrm{m}$ in diameter and consist of smaller mirror segments that reflect and focus
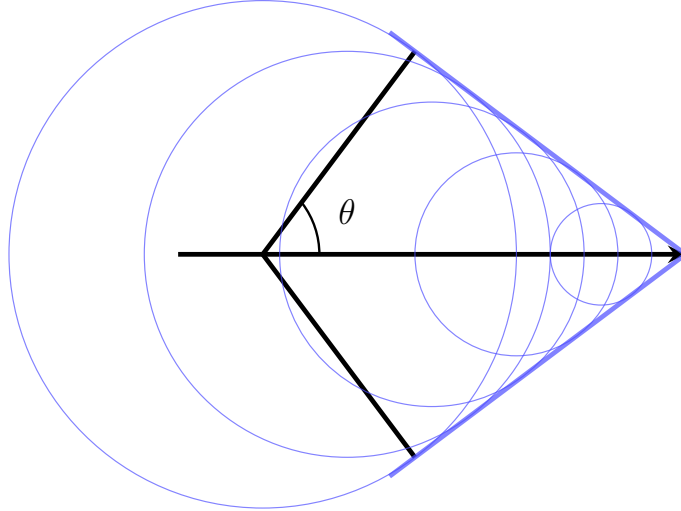
Figure 2.4: Sketch of a Cherenkov radiation cone with the characteristic opening angle θ.

the Cherenkov light produced by the EAS into high-speed photomultipliers located in the focal plane of the telescope [23]. The current active telescopes are the VERITAS array in Arizona [35], H.E.S.S. obsevatory in Namibia [36] and the MAGIC telescope in the Canary Islands [37]. A new observatory, the Cherenkov Telescope Array (CTA) is under development by a consortium of researchers from 27 countries from all continents[38].

IACTs have a good angular resolution, of the order of 0.1°. Since IACTs detect the characteristic light of the EAS as it develops in the atmosphere, they have a relatively low energy threshold and energy resolution of $< 20\%$. However, their field of view is limited ($\leq 5°$) and they can only operate in clear, moonless nights, leaving to a duty cycle of around 10%.

2.2.3 EAS Arrays

Another technique to detect gamma rays is by sampling the secondary particles of the EAS that reach the Earth's surface. This is done by using an array of detectors that covers a large area. These detectors are built at high altitude in order to be closer to the shower maximum of the extensive air showers and are able to detect showers of $\sim$100 GeV up to $\sim$100 TeV. Advantages of these arrays are:

- High duty cycle: In principle, they can operate all day, compared to only clear night observations of IACTs.

- Field of view: These detectors monitor large portions of the sky compared to IACTs

Two different techniques have been used for the detectors. One consists of the use of scintillation counters capable of measuring the time when particles interact with them. They also allow to measure the density of the charged particles. An example of this kind of detector is ARGO-YBJ located in Tibet, China [39]. The second technique uses water-filled vessels on ponds to produce Cherenkov light and sample the particles that get to the ground. Photomultipliers (PMTs) immersed in the water detect the Cherenkov light. A custom-made electronic read-out sysstem allows to measure the time of each detection and the amount of light or energy density. The
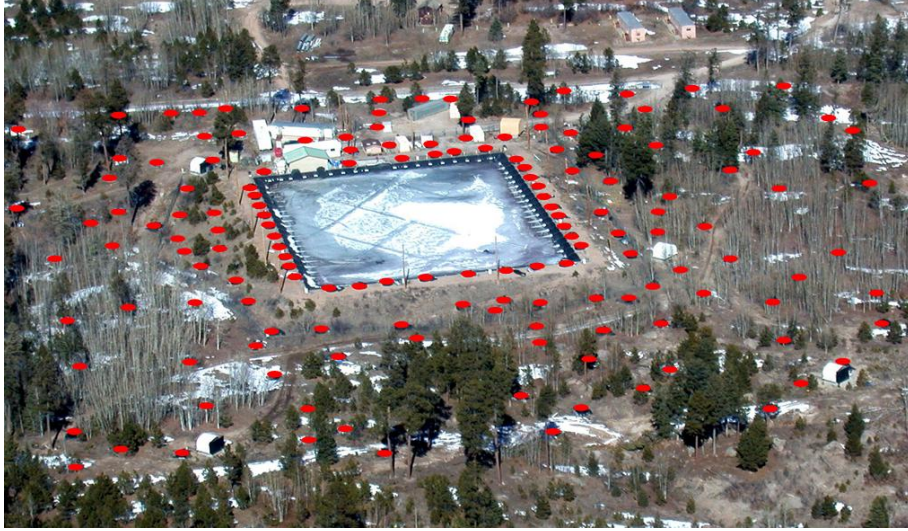
Figure 2.5: The Milagro Detector. The positions of the outrigger tanks are marked in red.

Milagro detector belongs to the first generation of this kind of technique. It was located in Los Alamos, New Mexico at an altitude of 2630 m a.s.l. [40]. Figure 2.5 is a photo of the Milagro Observatory. It consisted of a central pond filled with water containing two layers of PMTs. The top layer was used for reconstruction of EAS events, while the bottom part was used for gamma-hadron separation and energy estimation. The detector was upgraded with an array of smaller tanks surrounding the main pond in order to improve the reconstruction. These were called outriggers —in reference of a secondary float that helps a canoe. In both techniques the time and charge density information are used to determine the direction of the original gamma-ray. The HAWC observatory, which will be described in the next chapter, represents a new generation of water Cherenkov detectors. The reconstruction of gamma-ray EAS with the HAWC observatory is presented in chapter 4.

Chapter 3

The HAWC Observatory

The High Altitude Water Cherenkov (HAWC) observatory is a second generation water Cherenkov detector designed to study cosmic and gamma rays. It is sensitive to high-energy particles in the energy range of $100\,\text{GeV}$ to $100\,\text{TeV}$ [41]. The observatory is located in the state of Puebla in Mexico, between the volcano Pico de Orizaba and Sierra Negra, at an altitude of $4100\,\text{m}$ a.s.l. The geographic coordinates are $18°59'41"$ N, $97°18'30"$ W.

With an instantaneous field of view of $2\,\text{sr}$ and a duty cycle of $> 95\%$, HAWC has a daily sky coverage of $8.4\,\text{sr}$ of the sky. It covers the declination band between -26° to 64° of the celestial sky. Half of the galactic plane is seen by HAWC, with the galactic center been close to the horizon of HAWC.
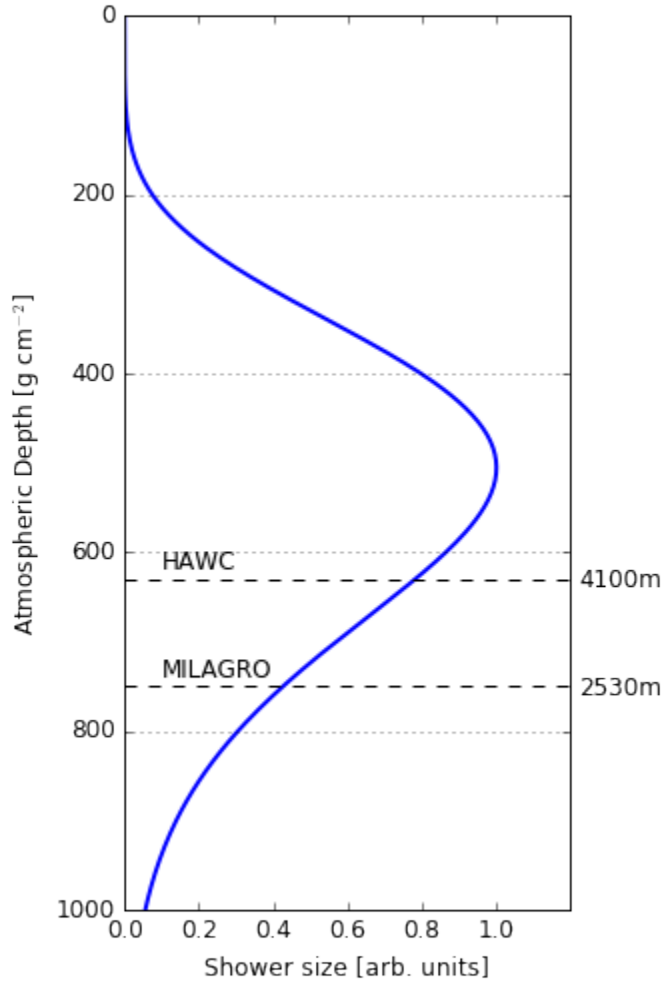
Figure 3.1: Shower size versus atmospheric depth for a typical gamma-ray shower. Model obtained from [4]. The dashed lines indicate the altitudes of HAWC and Milagro.

As mentioned in chapter 2, the HAWC array uses the water-Cherenkov technique for the observation of cosmic rays and gamma rays. The altitude of HAWC corresponds to an atmospheric depth of $638\,\mathrm{g/cm^2}$ or 17.2 times the radiation length for pair production and bremsstrahlung interactions in air [42]. This still puts HAWC below the shower maximum but closer to it than the Milagro observatory. (See figure 3.1).

HAWC was inaugurated in March of 2015, although it started recording data and science operations with a third of the detector in August 2013. A picture of the full detector is shown in figure 3.2.

Figure 3.2: The HAWC Observatory. Picture taken by the author.

3.1 Water Cherenkov Detectors

HAWC consists of 300 water Cherenkov detectors (WCDs), covering an effective area of $20,000\,\mathrm{m}^2$ with $12,000\,\mathrm{m}^2$ of active surface. Each of these WCDs consists of corrugated steel tanks of $7.3\,\mathrm{m}$ in diameter and $5\,\mathrm{m}$ in height. Inside the tank, a plastic-bladder holds up to ~ 200000 liters of processed water, which corresponds to a height of $\sim 4\,\mathrm{m}$. At the bottom of the tank there are four photomultiplier tubes (PMTs). Three of them are 8-inch Hamamatsu R5912, located at $1.8\,\mathrm{m}$ from the center and spaced 120° apart. A 10-inch Hamamatsu R7081-MOD is located at the center. The PMTs are sensitive to light in the wavelength range of $300\,\mathrm{nm}$ to $500\,\mathrm{nm}$. A schematic

is shown in figure 3.3.
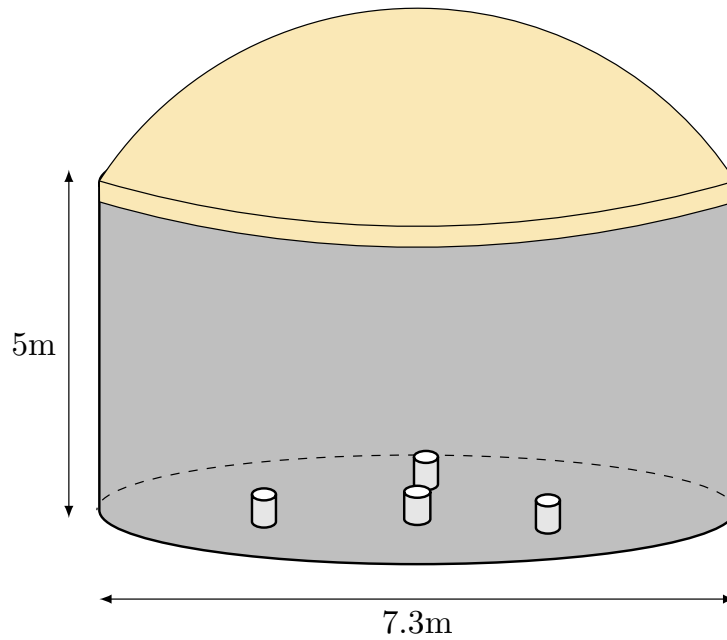
Figure 3.3: Schematic of a water Cherenkov detector.

The PMTs detect the Cherenkov light produced by the secondary particles that enter the WCD. Using the photoelectric effect, photoelectrons (PEs) are produced in the photocathode of the PMTs. By applying a high voltage to the PMTs, the PE signal can be amplified through the 10-stage dynode chain of the PMT, producing up to 10^7 electrons. The voltages on the PMTs are chosen to match the PMT gains across the array and it has values close to $\sim 1700\,V$. Using $\sim$550ft RG59 coaxial cables, the signal of the PMTs is sent to the main building at the HAWC (the counting house), located at the center of the array.

3.2   Data Acquisition System

The counting house is the place where the data acquisition system (DAQ) is located. The DAQ is composed of all the electronics that process and analyze the signal from the PMTs. The signal is processed by custom-made front end boards, which shape and organize the signal depending on two voltage thresholds at $30\,\mathrm{mV}$ and $50\,\mathrm{mV}$. When a pulse crosses these thresholds, the time is recorded by CAEN VX1109A time-to-digital converters (TDCs) with a resolution of $100\,\mathrm{ps}$. These time-stamps are then used to estimate the number of PEs, using a time-over-threshold method.

The DAQ reads out PMTs signals during a $2\,\mathrm{\mu s}$ window after a simple trigger condition is met. HAWC utilizes a multiplicity trigger that counts the number of PMTs signals in a 150ns trigger window. For the full detector, with at least 90% active PMTs, the trigger is set to 28 PMTs. The trigger rate for HAWC is $\sim23.5\,\mathrm{kHz}$. The time and charge information are used to reconstruct the main properties of the primary gamma rays and cosmic rays. This process is explained in chapter 4.

3.3 Scientific Objectives

The main scientific goals of the HAWC observatory are the understanding of particle acceleration in sources of galactic and extra-galactic origin, as well as the propagation of high-energy cosmic rays through the universe. HAWC will almost continuously survey the VHE gamma-ray sky. This complements other IACT instruments that observe lower-energy gamma rays (See [41] for more details). For instance, the observation of VHE energy gamma rays (with energies of $\sim 100\,\mathrm{TeV}$) from point sources can confirm that hadronic cosmic-ray acceleration sites exist in SNRs.

Thanks to the high duty cycle of the HAWC observatory, detection and monitoring of transients such as AGNs, gamma-ray bursts, flares from PWN and binary systems will be possible. The first catalog of point-like sources from the galactic plane is presented in [43].

Study of diffuse gamma-ray radiation from the Galaxy also probes the origin and propagation of cosmic rays. The gamma-ray flux is proportional to the cosmic-ray flux with the energies of the gamma rays being ten times smaller than the energies of their parent cosmic rays. The hypothesis that the flux of the sea of cosmic rays is constant throughout the Galaxy can be tested.

HAWC not only detects gamma rays, but also cosmic rays. A recent publication

shows the study of large and small-scale cosmic ray anisotropy in the northern sky [44]. The large-scale anisotropy is not well understood. It has long been suggested that a weak dipole feature should be a consequence of the diffusion of cosmic rays from nearby sources in the Galaxy[45]. The small-scale structure, on the other hand, could be the product of turbulence in the Galactic magnetic field[46].

Furthermore, HAWC will help solve some fundamental physics problems, such as Dark Matter or Lorentz violation. For example, the possible measurement of gamma ray emission from low luminosity, high mass galaxies can provide clues for dark matter particles with masses of $\sim$1 TeV [47, 48].

Chapter 4

Data and Reconstruction

4.1 HAWC Data

A brief description on how the data is collected was presented in chapter 3. The total data collection rate is 400MB/s and drops to 15-20MB/s after the application of trigger conditions. This means that in a day $\sim$2 TB of data are collected.

This chapter describes the data process in order to obtain the information of the primary particle: the type, its direction, and energy. The first step is to identify the event showers after the signal is digitized by the DAQ. A proper calibration of the system is needed in order to have a precise and accurate measurement of both the direction and energy. Then the position of the core of the EAS front is found by using

the measured charge. This is followed by finding the direction of the EAS. Finally, a series of cuts are implemented to distinguish between hadrons and gamma rays.

There are two types of reconstruction processes. The first is an online reconstruction performed at the HAWC site. This is done to provide preliminary and instant results, in the case of any transient observations. This reconstruction is also useful to give alerts to other telescopes in real time. The second is an offline reconstruction, which uses similar, but improved algorithms compared to the online reconstruction since most of the computer power at the site is used for the processing of the data. The official reconstruction of the data is done on the computer clusters at the University of Maryland and Universidad Nacional Autonoma de Mexico.

4.2   Edge Finding

The main component of an air shower event in the HAWC array is called a hit. A hit is the detection of Cherenkov light in a PMT. The information of the hit consists of the position of the PMT, the time when the hit occurred, and the charge of the hit. The positions of the PMTs are defined through the layout of the detector (Figure 4.1).

The DAQ saves the time stamps when the signal crosses two voltage thresholds to
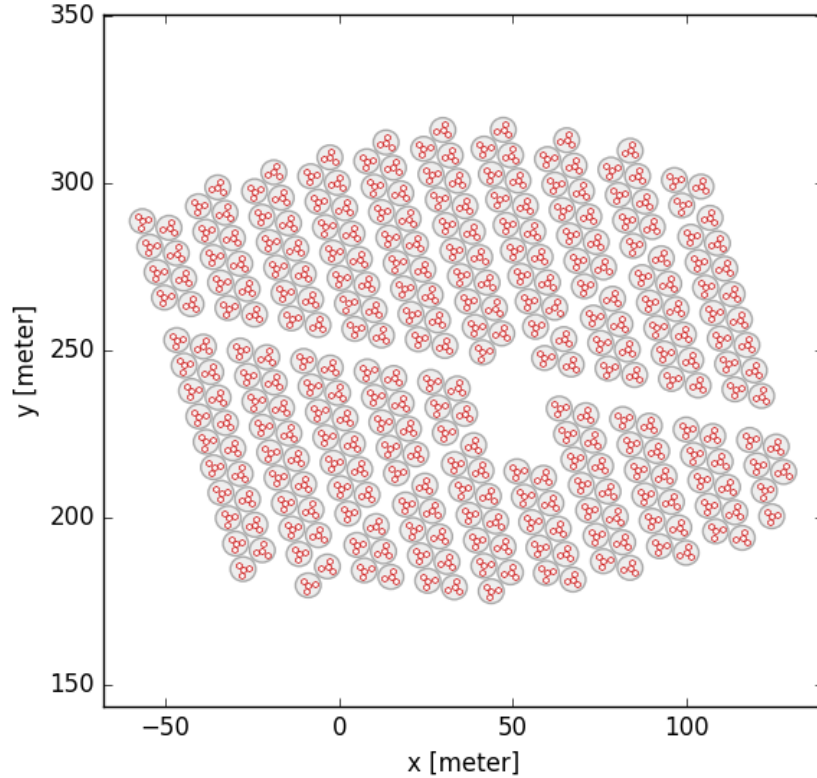
Figure 4.1: Configuration of the HAWC observatory. The position of the WCDs and the PMTs are shown

identify signal pulses from the PMTs. These times are called "edges" and are labeled t_0, t_1, and so on. The voltage thresholds are set to the equivalent of 1/4 and 4 PEs. The time between threshold crossings is called time-over-threshold or ToT. A two-edge hit is a small pulse that only crosses the low threshold. The two-edge hits have a low ToT of $t_1 - t_0$. A large pulse that crosses both thresholds is called a four-edge hit. Four-edge hits have a low ToT of $t_3 - t_0$ and a high ToT $t_2 - t_1$ (Figure 4.2). An edge-finding algorithm was designed to identify the pulses in each of the PMTs from the data stream.
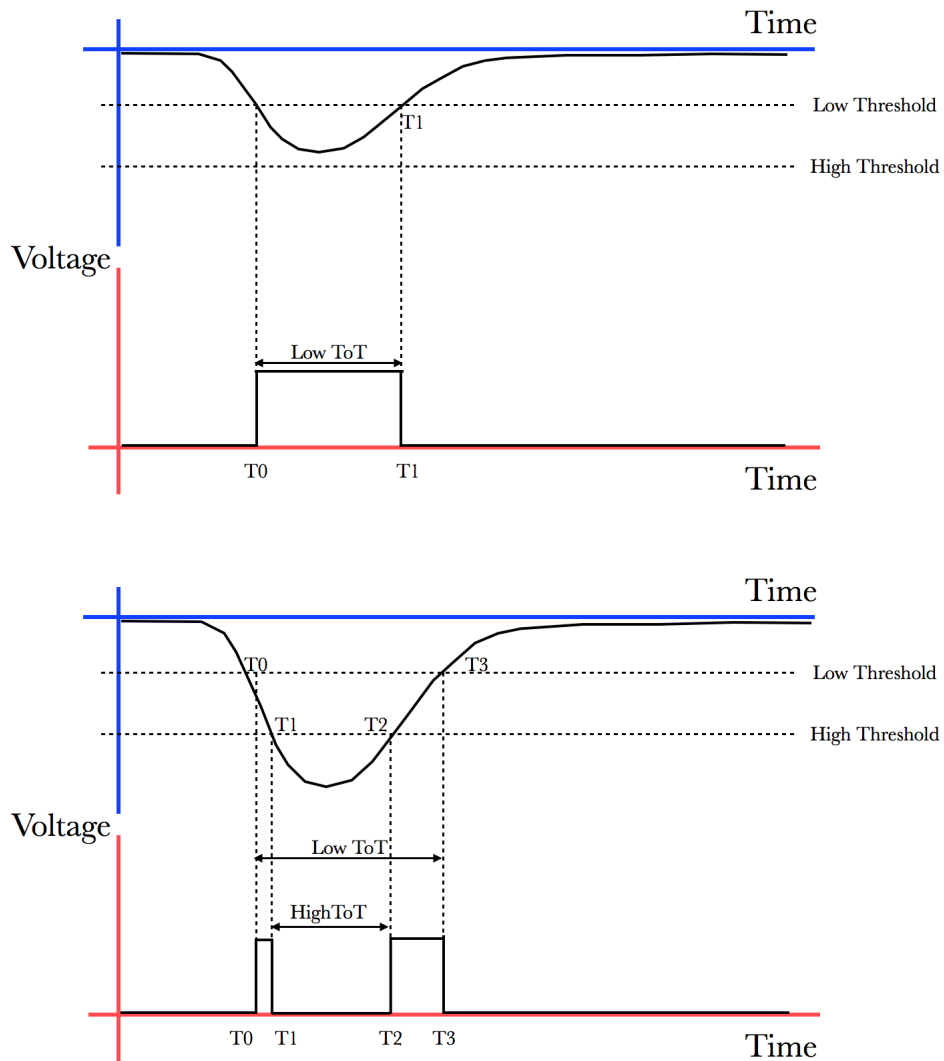
Figure 4.2: Schematic of a small and a large pulse with their corresponding time stamps.

4.2.1 Calibration of the HAWC Observatory

The time of the edges and ToTs are the main variables to obtain the initial time of the signal and the charge in each PMT.

The HAWC Observatory has a laser system that performs timing and charge calibration. The timing calibration measures two main effects: a slewing effect in each PMT and a relative time offset between each PMT. The charge is obtained by a conversion between ToT and charge.

The laser system emits pulsed light with a wavelength of 532nm. A square-wave pulse generator is used to trigger the laser. The light is split by an optical splitting cube. The split beam is sent —through a 1:19 optical splitter— to a radiometer in order to monitor the initial power of the light, I_{ref}. The other beam is sent through a series of three filter-wheels, each holding six neutral density filters that can be selected by software. The filter-wheels vary the intensity of the laser light over six orders of magnitude. The intensity of the light after the filter-wheels is given by:

$$\frac{I}{I_{ref}} = 10^{-\alpha} \tag{4.1}$$

where α is the total optical depth provided by the three filter-wheels.

$$\alpha = \sum_{i=1}^{N=3} OD_i \tag{4.2}$$

The optical depths are shown in table 4.1

A combination of 180 non-opaque (not using position 1 in FW3) filter-wheel settings is possible. However, some of this settings are repeated. At the time of writing, the

Table 4.1
Filter-wheels (FW) optical depth values

FW position	OD1	OD2	OD3
1	5.0	0.0	99.0
2	0.0	0.2	0.0
3	1.0	0.4	0.3
4	2.0	0.6	1.0
5	3.0	0.8	1.3
6	4.0	1.0	2.0

calibration system uses 68 combinations that provide transmittance factors of 1 to $10^{-6.5}$.

After the filter-wheels, the light beam is split once more with another optical splitting cube. One light beam goes to another radiometer to monitor the light after the filter-wheels (referred to as I in equation 4.1). The other beam passes through a 1:37 optical splitter. Eight outputs from this splitter are connected to eight 1:16 optical switches. The switches send light to 1:2 or 1:4 splitters which then are connected to long 550 feet optical fibers plus 25 feet optical fibers that go from a junction box at the bottom of each WCD to the top of the WCD. These fibers connect to the 300 WCDs. At the end of the short optical fiber there is a diffuser that spreads the laser light inside the WCD in order to trigger the 4 PMTs.

The calibration system sends a notification to the DAQ everytime the laser is fired. This way the laser light is not misidentified as part of an air shower signal. Also, the

time when the laser fires is saved, which marks the beginning of a 2 μs time window used to analyze the charge and time calibration data.

4.2.1.1 Timing Calibration: Slewing Time

The time when the PMT pulse crosses the first threshold, is assigned as the time of the signal in that PMT. This time depends on the pulse size, since a bigger pulse yields an earlier crossing time of the low threshold. This response time is referred as slewing time, which is a function of low/high ToT.
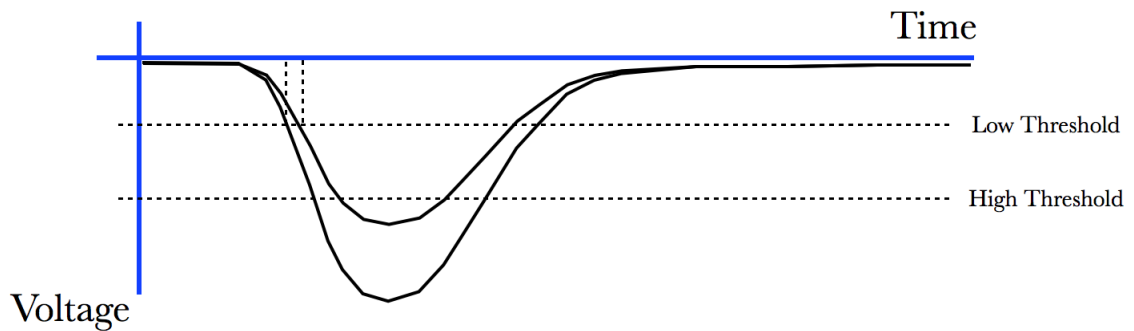
Figure 4.3: Sketch of the slewing effect. A bigger pulse crosses the threshold earlier than a smaller pulse.

The calibration system is used to obtain the slewing time as a function of ToT. The time interval between firing the laser and the PMT pulse crossing the voltage thresholds is called the raw slewing time. It includes the response time of the PMT, electronics and the time for the laser light to go through the optical path (splitters,
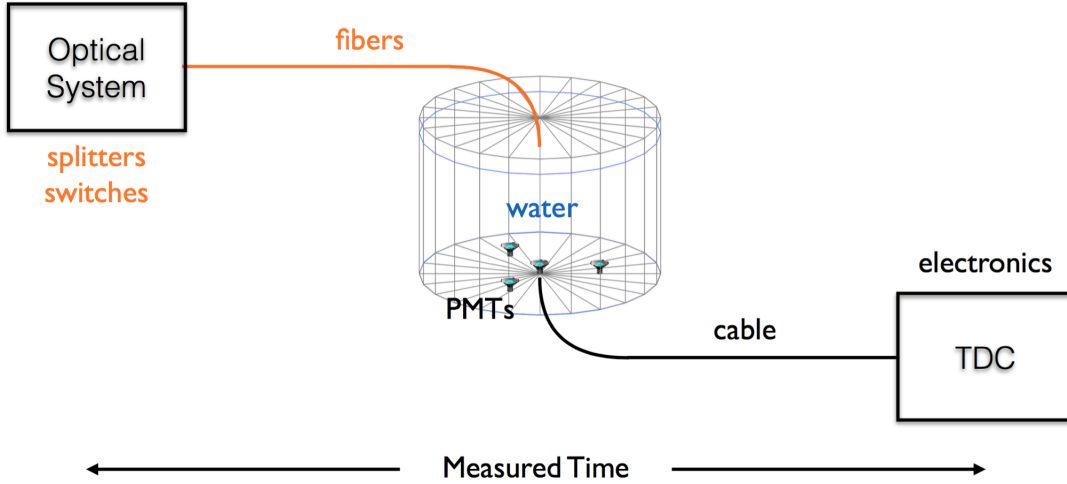
Figure 4.4: Sketch of the calibration system. The calibration system measures the total time between the time that the laser is fired and the detection in the DAQ.
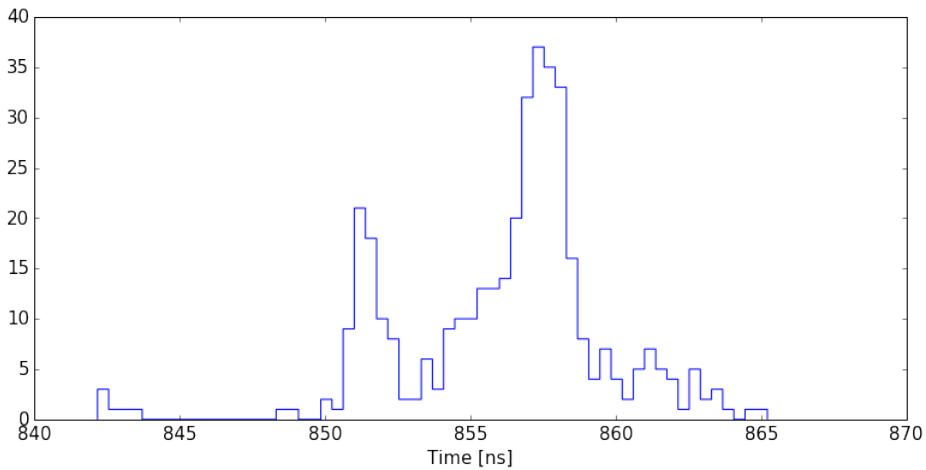
Figure 4.5: Measured time of the optical path for the 300 WCDs. The measurements were done at the HAWC site.

long fibers and water; see figure 4.4).

The optical path time was measured at the site, and shown in Figure 4.5. Subtracting this timing information from the raw slewing time, the response time of the PMTs and electronics is obtained.
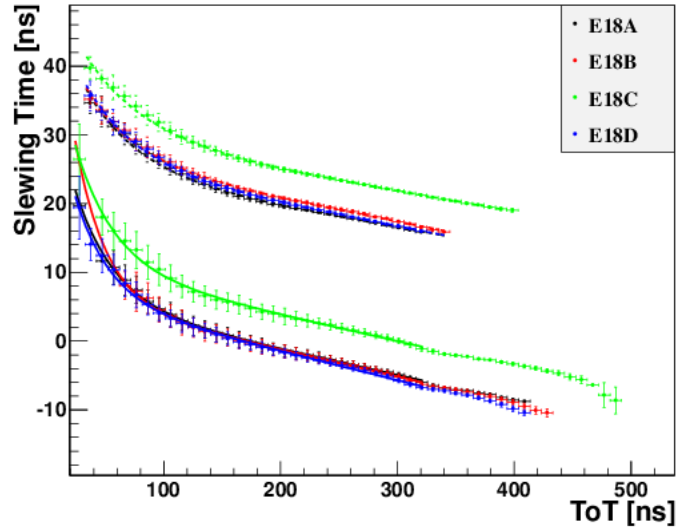
Figure 4.6: Slewing curve for one of the WCDs. PMTs are labeled A through D. PMT C is the 10" PMT. The group of lines in the upper part of the graph correspond to the curves for the high threshold while the group of curves in the bottom are for low threshold.[5]

An example of a slewing calibration run for one of the tanks is shown in figure 4.6.

4.2.1.2 Timing Calibration: Relative Time Offset

The relative time between PMTs is one of the crucial measurements required to obtain the direction of the primary particle. The timing measurements of the optical system can have variations of the order of ~ 1 ns. The resolution of the measured time for the HAWC observatory can be improved to ~ 0.1ns. To reach this objective, we apply a time residual method. The time residual is a systematic offset defined as the difference between the PMT readout time and the fitted arrival time of the air shower in the PMT. Figure 4.7 shows an schematic of the time residual procedure.
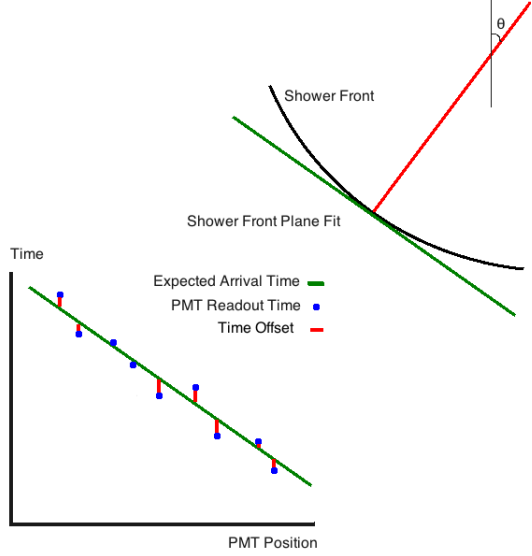
Figure 4.7: The black line represents the true shower front of an extensive air shower. The green line represents the plane shower front after the curvature correction. This is used for the expected arrival time, which is then compared to the readout times of the PMTs. [5]

As will be explained in section 4.3.2, a curvature correction is applied to the shape of the shower front in order to have a plane whose normal points to the direction of the initial particle. The time residual is implemented as follows. 200,000 air shower events from within 30° from the zenith angle and with at least 200 PMTs triggered by the air shower are used. The events are reconstructed with the slewing calibration. The time residuals are calculated for each PMT and a histogram is obtained. A gaussian fit is used to find the mean time residual in each PMT (Figure 4.8). This mean time residual is added to the relative time and used in another iteration of this procedure. This method is repeated three times until the time offset in each PMT is closer to zero (Figure 4.9).
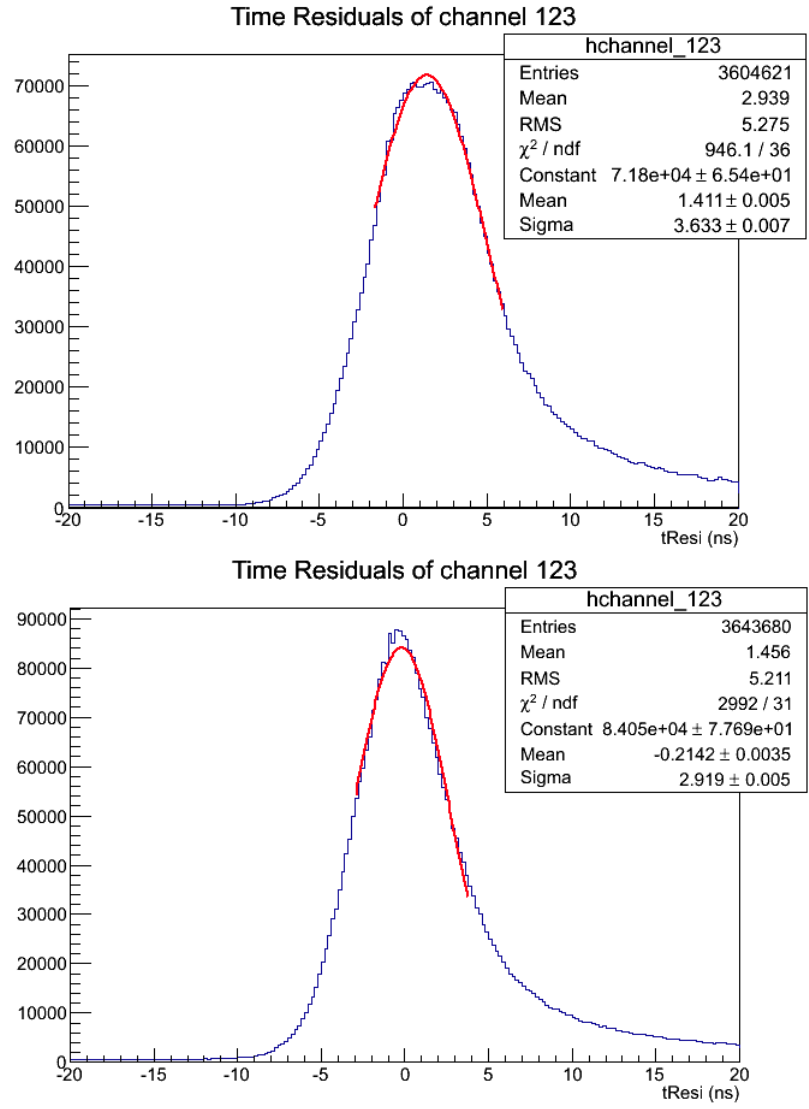
Figure 4.8: Time residual histograms for one of the PMT channels before and after the time residual method. The histogram after the correction shows a smaller width and the mean is closer to zero. [5]
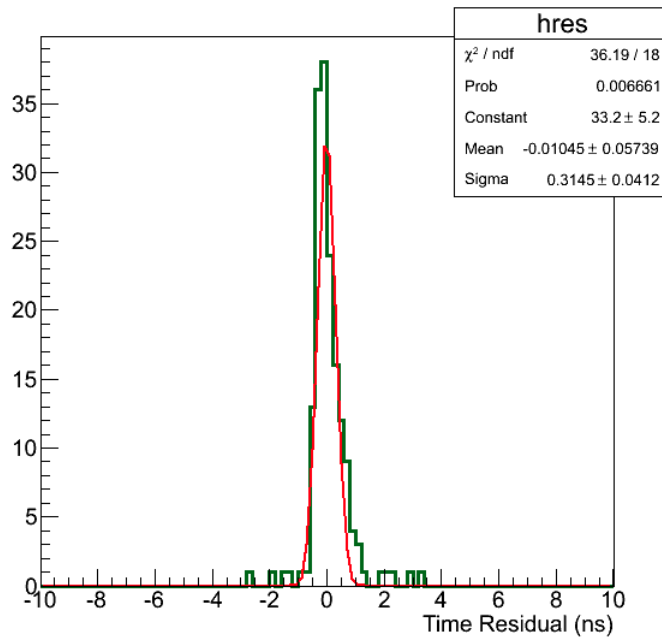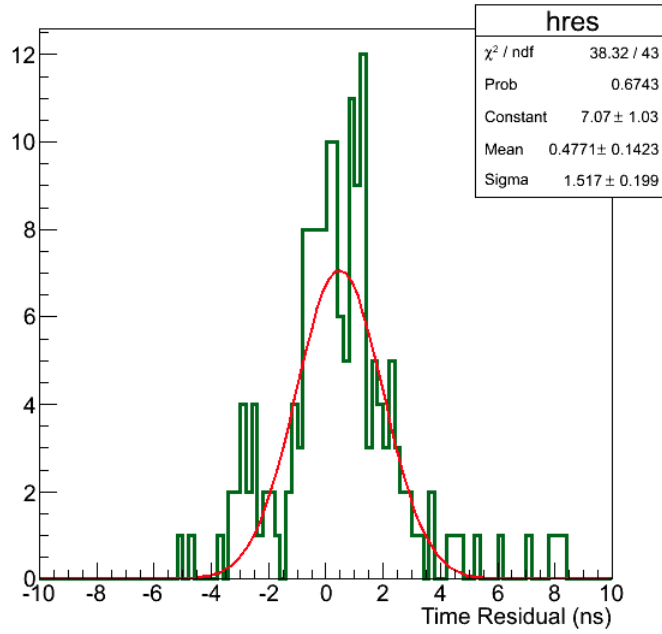
Figure 4.9: The mean time residuals in each PMT before and after correction for the relative time offset. [5]

4.2.1.3 Charge Calibration

The amount of charge detected by a PMT is obtained indirectly by comparing an expected distribution of photon-electrons (PEs) with the ToT distribution. A direct measurement of the charge would be possible, however, the transmittance in each optical path to the WCDs is different from each other, making the procedure complicated.

Using the different light intensities due to the different filter-wheel configurations, the calibration system measures the probability of detecting at least one PE with each intensity. With this probability, the expected number of PEs $\langle N_{PE} \rangle$ can be calculated for each intensity. The number of PEs is assumed to follow a poisson distribution for each PMT with mean $\langle N_{PE} \rangle$. To represent the charge resolution of the PMTs, the PE distribution for each intensity is smeared by a factor of $\sigma = 0.35\langle N_{PE} \rangle$ following a Gaussian distribution. The PE distributions and the ToT distributions are matched for each intensity set from the filter-wheels to produce a curve of PEs as a function of ToT.

The calibration measurements are used in the reconstruction process that is described in the following section.

4.3 Reconstruction

4.3.1 Core Reconstruction

The measured charge at each of the PMTs is used to detect the core position of an air shower. The core is found by using two algorithms. The first algorithm consists of a simple center-of-mass (COM) procedure. This algorithm estimates the core position inside the detector and the result is used as a first guess for a more accurate algorithm. The first guess of the core position is obtained by the following equations.

$$x_{COM} = \frac{\sum x_i q_i}{\sum q_i} \qquad (4.3)$$

$$y_{COM} = \frac{\sum y_i q_i}{\sum q_i} \qquad (4.4)$$

where x_i, y_i are the position of the PMTs and q_i is the measured charge in each PMT that participate in the measurement of an air shower event.

The COM core position is then used as the seed for a more time-expensive algorithm in order to improve the location of the core position. The algorithm is a χ^2 minimization procedure used to find the optimal parameters that describe the core position. The χ^2 compares the measured charge q_i to an expected charge Q_i modeled by a charge distribution (or lateral distribution in the jargon of EAS).

$$\chi^2 = \sum^{N_{PMTs}} \frac{(q_i - Q_i)^2}{\delta q_i^2} \qquad (4.5)$$

where δq_i is the error of the measured charge.

The first lateral distribution function applied in HAWC was a gaussian function,

$$Q(x_i, y_i; N, x_o, y_o, \sigma) = \frac{N}{2\pi\sigma^2} \exp\left(-\frac{1}{2}((\frac{x_i - x_o}{\sigma})^2 + (\frac{y_i - y_o}{\sigma})^2)\right), \qquad (4.6)$$

where N is the amplitude, σ is the width of the shower core, and x_o, y_o are the coordinates of the core position.

Figure 4.10, shows the distributions of core positions during the time when HAWC had around 111 WCDs (HAWC-111). As can be seen, a ring structure surrounds the central part of the detector. In these cases, the minimization of the χ^2 preferred to have the tails of the gaussian inside the array.

The gaussian function is a simple approximation for the lateral distribution of an air shower and requires minimal computational resources when used as a model in the minimization process. A better approximation is obtained by applying the physics of EAS. For the first survey of the Galactic Plane with HAWC[43], the expected charge was obtained from the Nishimura-Kamata-Greisen (NKG) function [49, 50]. The NKG function is used to describe the lateral distribution of electromagnetic showers.
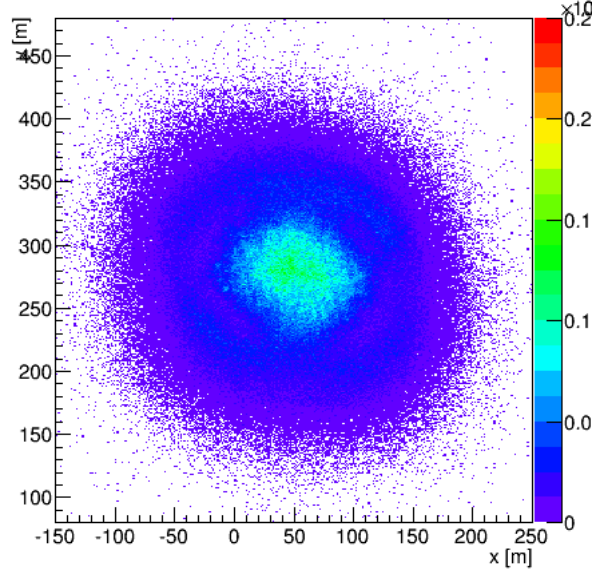
Figure 4.10: Core distribution using a gaussian lateral distribution function during HAWC-111. A ring structure is observed around the detector.

The function is defined as:

$$Q(x_i, y_i; N, x_o, y_o, s) = \frac{N}{2\pi R_{Mol}^2} \frac{\Gamma(4.5 - s)}{\Gamma(s)\Gamma(4.5 - 2s)} \left(\frac{r}{R_{Mol}}\right)^{s-2} \left(1 + \frac{r}{R_{Mol}}\right)^{s-4.5}, \quad (4.7)$$

where N is the total number of electrons in the shower event; the value s is referred to as the shower age, which parametrizes the stage of the shower development. If $s = 1$, the number of particles in the shower plane reaches its maximum. The distance of the shower core to the PMT position is the value $r = \sqrt{(x - x_o)^2 + (y - y_o)^2}$. R_{Mol} is called the Molière radius. This value is defined as

$$R_{Mol} = X_0 \frac{E_s}{E_c \rho} = (37.15 \,\mathrm{g\ cm^{-2}}) \frac{21\,\mathrm{MeV}}{(84.4\,\mathrm{MeV})\,(7.4 \times 10^{-4}\,\mathrm{g\ cm^{-3}})} = 124.21\,\mathrm{m} \quad (4.8)$$

56
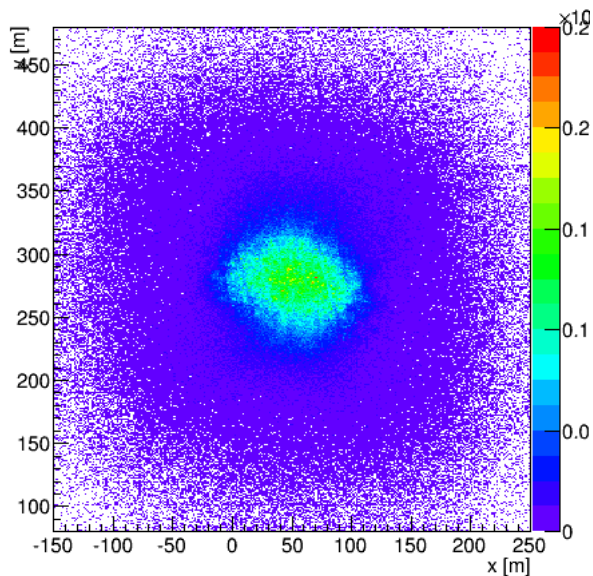
Figure 4.11: Core distribution using an NKG lateral distribution function during HAWC-111. The ring structure disappears with this lateral distribution.

where X_0 is the radiation length in air, E_s is the scattering energy, E_c is the critical energy at which an electron loses equal amounts of energy per unit radiation length by ionization and bremsstrahlung —At energies bigger than E_c, bremsstrahlung dominates the energy losses—, ρ is the air density at the height of observation. This gives a value of 124.21 m at the HAWC site.

The χ^2 minimization with an NKG distribution became too computationally expensive once most of the detector was online. In order to speed up the analysis, a new function was constructed, based on the combination of a gaussian function and the tail of the NKG distribution.

The function is defined as:

$$Q(x_i, y_i; N, x_o, y_o) = A \left(\frac{1}{2\pi\sigma^2} e^{\frac{-r^2}{2\sigma^2}} + \frac{N}{(0.5 + \frac{r}{R_{Mol}})^3} \right) \tag{4.9}$$

where r and R_{Mol} are defined as before; σ is chosen to be 10 m in order to fit cores near the array ; and N is the normalization of the integral of the second term in the equation relative to the Gaussian and the value is $5 \cdot 10^{-5}$. The three fitted parameters are the two coordinates of the core position and the amplitude A.

The core distributions of a sample of extensive air showers, for the complete detector with the NKG and gauss-NKG functions are shown in Figure 4.12.

Figure 4.13, shows an example of one extensive air shower event. This example is one where the core of the shower landed on the array. Figure 4.14 shows the charge distribution as a function of the distance from the core. The blue line is the best gaussian-NKG function after the χ^2 minimization. The green line is the NKG using the core position from the gaussian-NKG function.

4.3.2   Angular Reconstruction

After finding the position of the core of the air shower, the direction of the primary particle is measured.

58
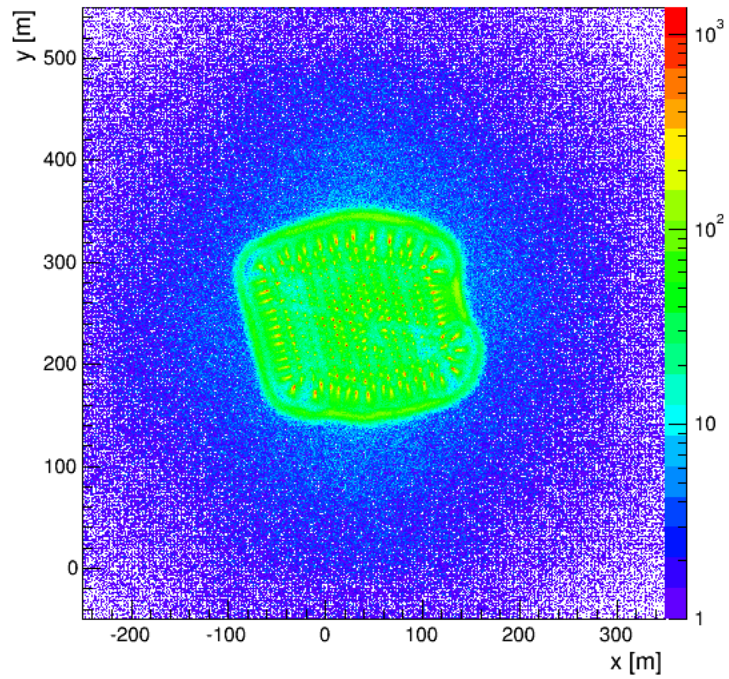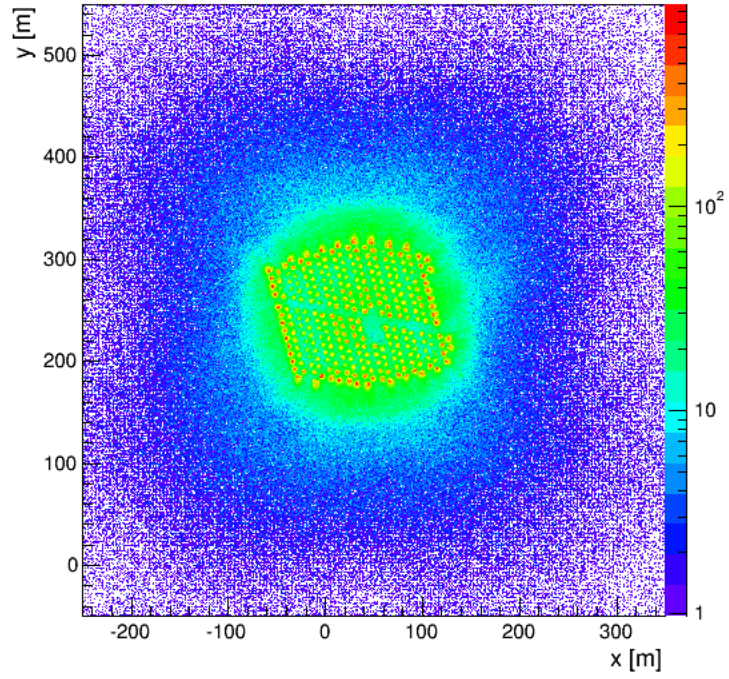
Figure 4.12: Core distributions for the complete detector using real data. The NKG function (upper plot) and the gauss-NKG (lower plot) function are used.
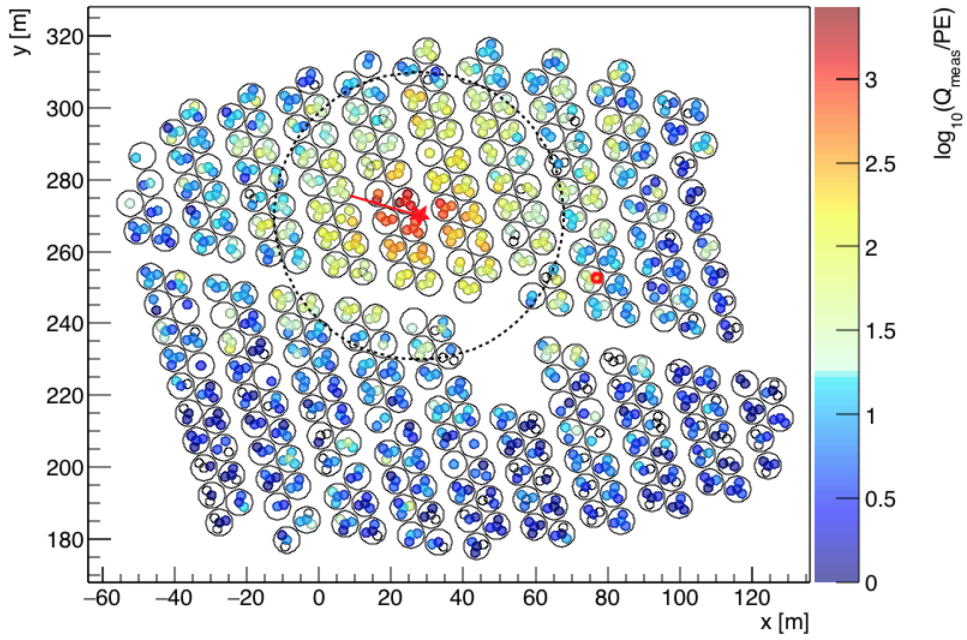
Figure 4.13: An extensive air shower event from real data coming from the region of the Crab. The core of the shower landed on the array.
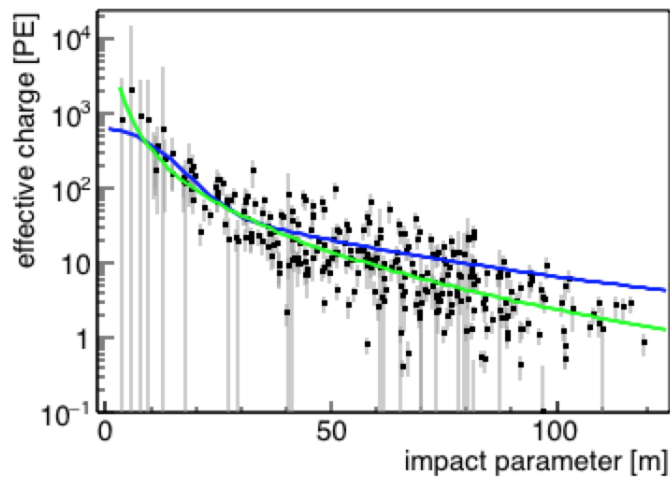
Figure 4.14: Charge distribution as a function of the distance from the core. The blue line is the best fit gaussian-NKG function after the χ^2 minimization. The green line is the NKG using the core position from the gaussian-NKG function.

60
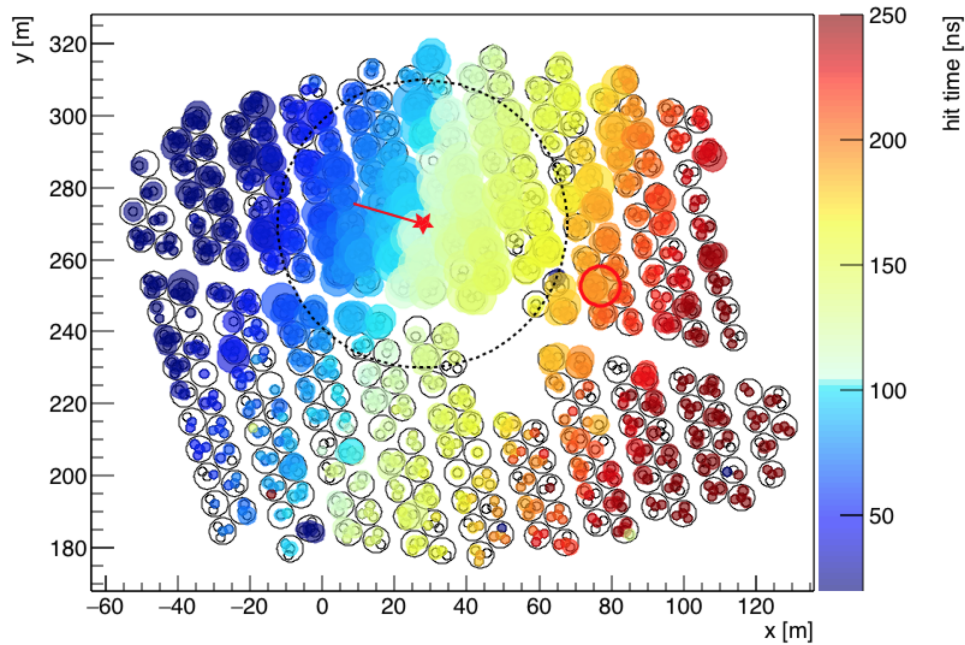
Figure 4.15: Times when each PMT is triggered by an extensive air shower event. The event is the same as in figure 4.13.

The shower front can be thought of as a thin pancake that crosses the detector array. During the crossing, the PMTs are activated at different times. The relative time between PMTs is used to obtain the shape of the shower front. Figure 4.15 shows the times when each PMT was triggered. The shower front is not completely flat, the hit times of the PMTs are shifted as described previously in order to produce a flat plane.

The measurement of the core position is important to produce this flat plane. Particles that are farther from the core are delayed with respect to a perfect plane tangent to to the core position. Using simulations, the curvature of the showers is found and a correction is applied.

Also, the particle density of the shower front decreases as a function of distance from the core, following the NKG distribution presented in section 4.3.1. Since there are less secondary particles farther from the core, the detection of the first PE in the PMTs away from the core can be delayed. This effect is referred as sampling and it is also corrected by using simulations.

After applying the corrections from the shower curvature and sampling, a weighted χ^2 is performed and the direction of the primary particle in the local coordinate sky is obtained. A distribution of the reconstructed zenith and azimuth angles is shown in figure 4.16.

4.4 Analysis Cuts: Describing the Air Shower Events

The shower size or footprint of an air shower event correlates with several parameters that describe the primary particle, such as the energy and the type of the particle.

HAWC data is divided into shower size bins f. These bins are defined by the ratio of the PMTs that participated in the reconstruction to the total number of PMTs that were available during the reconstruction.
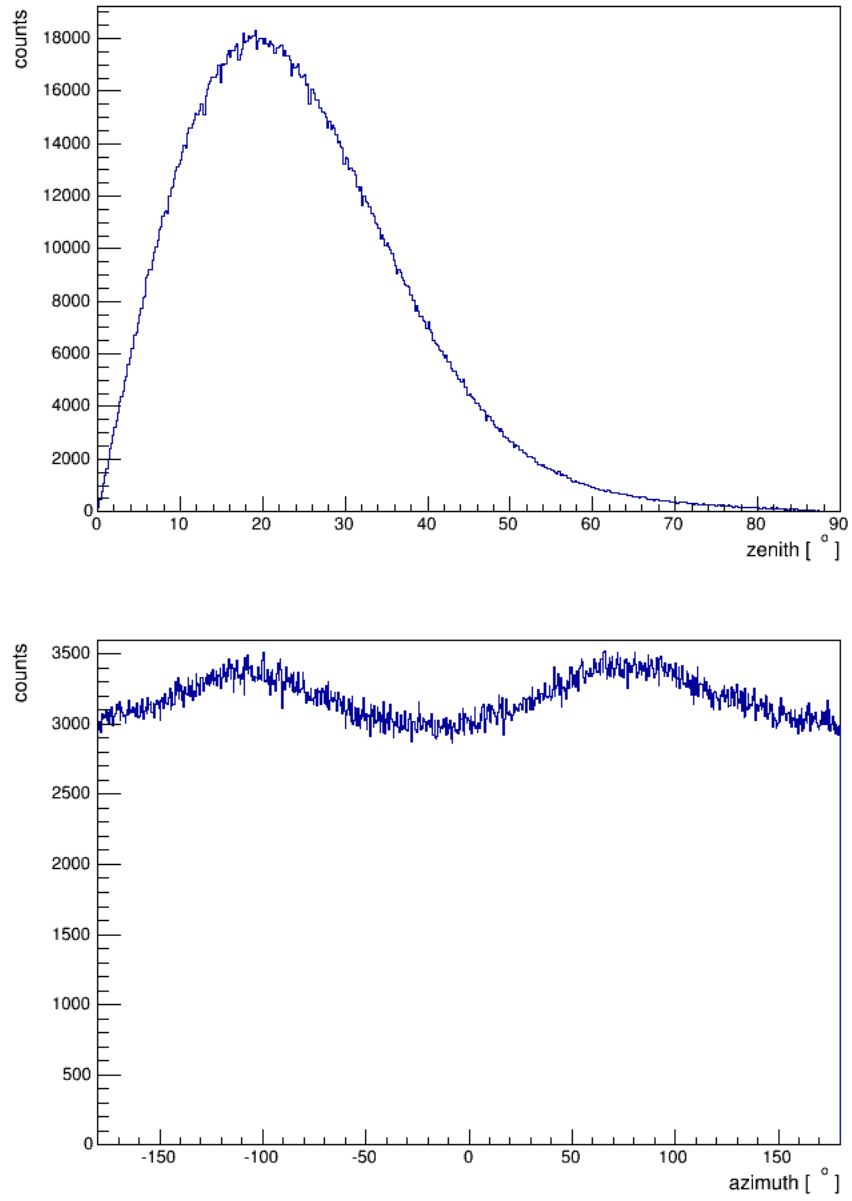
Figure 4.16: Distributions of the reconstructed zenith and azimuth angles from real data.

Table 4.2
Fractional f bins

f	Low	High
1	0.067	0.105
2	0.105	0.162
3	0.162	0.247
4	0.247	0.356
5	0.356	0.485
6	0.485	0.618
7	0.618	0.740
8	0.740	0.840
9	0.840	1.00

4.4.1 Simple Energy Estimator

The variable f works as a simple energy estimator. Figure 5.8 in chapter 5, shows
the energy histograms as a function of f. However, this parameter is dependent on
the spectral assumption for the observed source and on the direction of the primary
particle in the local sky. At the time of writing this thesis, different energy estimators
are being developed.

4.4.2 Gamma-Hadron Separator

As mentioned in chapter 2, hadronic cosmic rays and gamma rays produce extensive
air showers with different characteristics. For instance, gamma rays produce purely

electromagnetic showers, with extremely low numbers of muons or pions. Hadronic cosmic rays, on the other hand, produce a combination of electromagnetic showers, with muons, pions and other hadrons.

Hadronic cosmic rays are more abundant than gamma rays and account for the main background for the observation of VHE photons. Two variables are used to identify the type of primary particle that produces an extensive air shower.

The first variable is referred to as compactness, which measures how compact the footprint of a shower is in the detector array. The compactness $\mathcal{C}$ is defined as:

$$\mathcal{C} = \frac{N_{hit}}{CxPE_{40}} \tag{4.10}$$

where N_{hit} is the number of PMTs that participated in the reconstruction of the shower event, and $CxPE_{40}$ is the largest measured charge in a PMT outside a circle of 40m centered at the core of the shower. In general a gamma-ray shower event will have a higher value of $\mathcal{C}$. Figure 4.17 shows distribution of the parameter $\mathcal{C}$ for the different f bins. The difference between gammas (blue) and hadrons (red) is noticeable. Data is also plotted for comparison (black); since data is composed mostly from hadrons, the distributions of hadron simulation and data are similar.

The second variable measures how "unsmooth" the lateral distribution function of
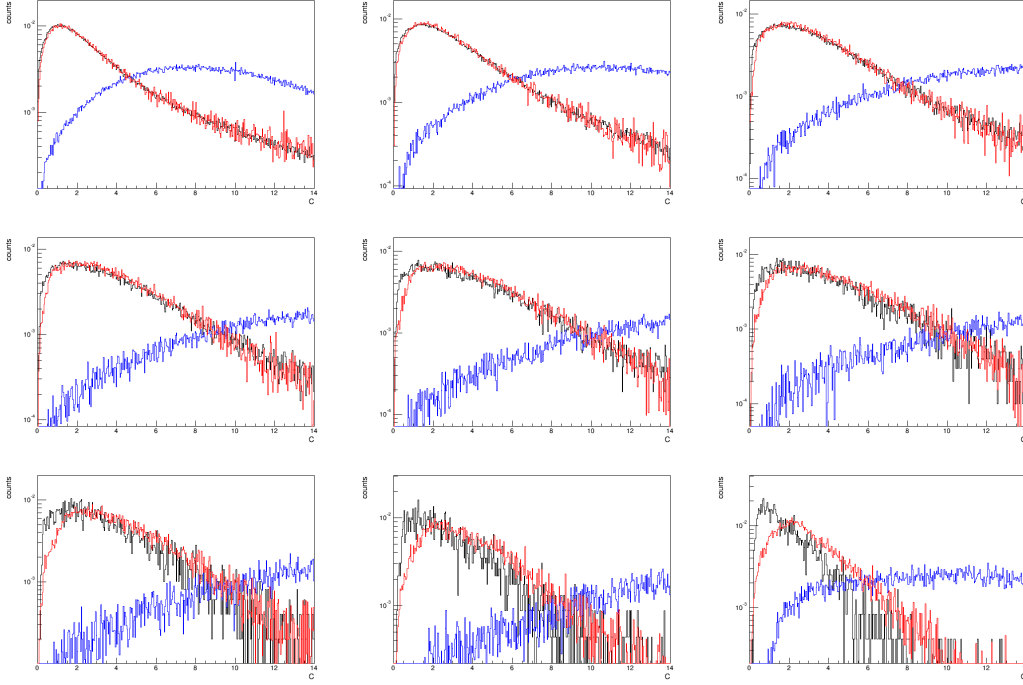
Figure 4.17: Compactness distributions for each f bin. Black: data; Red: hadrons; Blue: gammas. Upper-left plot starts with f_1 followed by bin f_2 and f_3 in the same row. Lower-right plot corresponds to bin f_9.

the air shower event is. This variable $\mathcal{P}$ is calculated as:

$$\mathcal{P} = \frac{1}{N} \sum_{i=0}^{N} \frac{(log(q_i) - \langle log(q_i) \rangle)^2}{\sigma_{log(q_i)}^2} \qquad (4.11)$$

where $log(q_i)$ is the logarithm of the measured charge in PMT i; $\langle log(q_i) \rangle$ is the average of the logarithm of the charge in all the PMTs that are inside an annulus containing the hit i, with a width of 5 meters, centered at the core of the shower; $\sigma_{log(q_i)}$ is the uncertainty in the charge derived from gamma ray events from the Crab. In general events with small values of $\mathcal{P}$ will be considered gamma rays. Figure 4.18 shows distribution of the parameter $\mathcal{P}$ for different f bins. The difference between

66
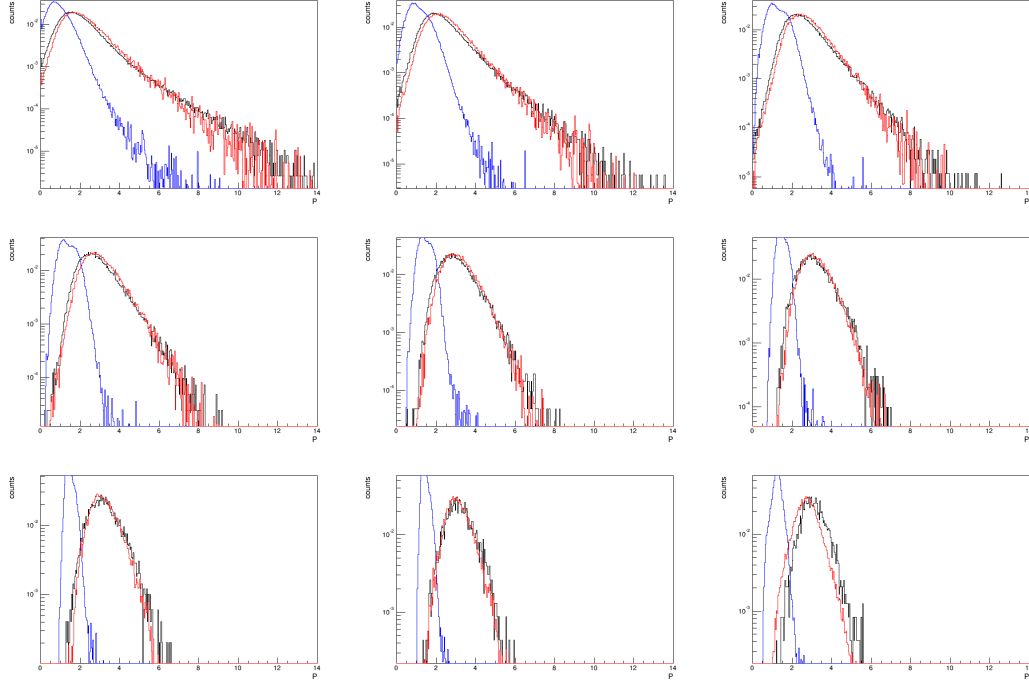
Figure 4.18: Smoothness distributions for each f bin. Black: data; Red: hadrons; Blue: gammas. Upper-left plot starts with f_1 followed by bin f_2 and f_3 in the same row. Lower-right plot corresponds to bin f_9.

gammas (blue) and hadrons (red) is noticeable. Data is also plotted for comparison (black); since data is composed mostly from hadrons, the distributions of hadron simulation and data are similar.

4.4.3 Angular Resolution

The angular resolution results in an uncertainty on the direction of the primary particle and it is called the point spread function (PSF). It depends on the size of the shower footprint in the array, on the zenith position of the primary particle and

improves with larger values of f_{Hit}. It is important in the study of point sources.

For the HAWC array, the PSF is approximated as a double-width Gaussian

$$PSF\delta = \alpha G_1(\delta) + (1 - \alpha)G_2(\delta) \tag{4.12}$$

where δ is the angle difference between the true direction and reconstructed direction of the primary particle; G_i is a normalized gaussian function and α represents the contribution from each Gaussian. Figure 4.19 shows two examples for the PSF in different f bins between the declinations 17.5^o and 22.5^o.
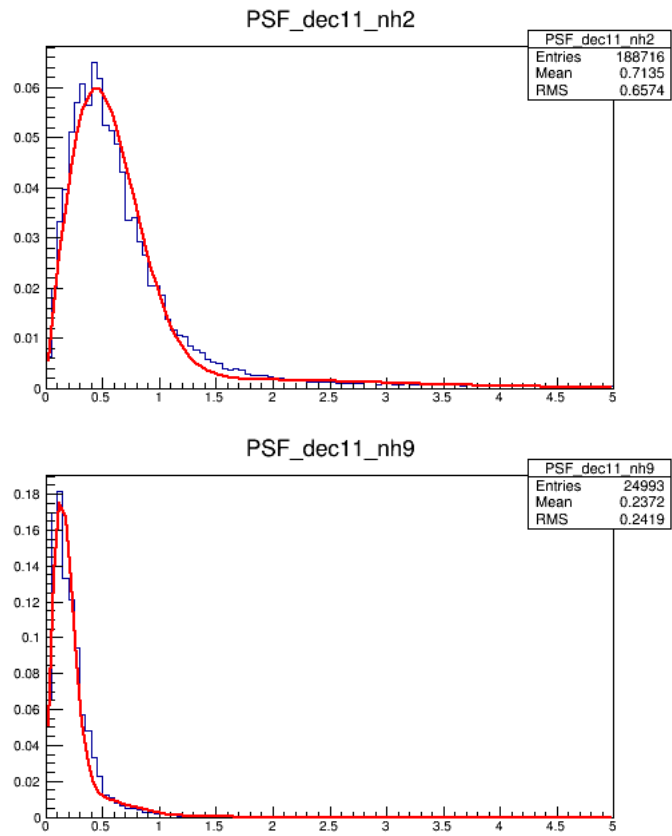
Figure 4.19: PSF for bins f_2 and f_9 in the declination band of 17.5^o - 22.5^o. The PSF improves with larger f bin. Usually, the 68% containment value is reported.

Chapter 5

The Fermi Bubbles

The search for a counterpart of the microwave haze [26] in gamma-ray data, using the *Fermi* telescope, revealed the existence of two large structures extending up to 55° above and below the Galactic Plane [26, 27]. Due to their bubble-like shape they recieved the name of *Fermi* Bubbles.
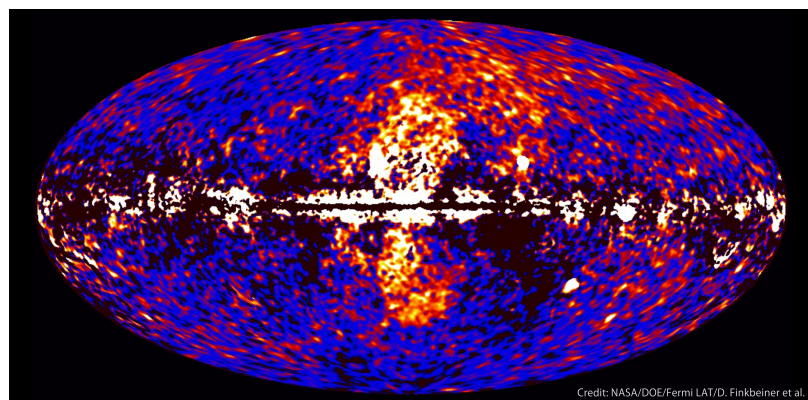
Figure 5.1: Fermi Bubbles observed between 1 GeV to 10 GeV. Credit: NASA/DOE/Fermi LAT/D. Finkbeiner et al.

The gamma-ray emission from the *Fermi* Bubbles presents a slowly falling spectrum —$dN/dE \sim E^{-2}$— in the energy range of $\sim 1\,\text{GeV}$ to $\sim 100\,\text{GeV}$; the surface brightness is roughly uniform in both bubbles —with an exception of a structure inside the south bubble called the cocoon; the total luminosity of the bubbles for $|b| > 10°$ and between $100\,\text{MeV}$ and $500\,\text{GeV}$ was found to be $4.4^{+2.4}_{-0.9} \times 10^{37}\,\text{erg}\,\text{s}^{-1}$ [6] .

5.1   The Origin of the *Fermi* Bubbles and Gamma-Ray Emission Mechanisms

The origin of the *Fermi* Bubbles is still uncertain. Different models have been proposed to explain their formation. Most of the models revolve around the idea of outflows from the galactic center which then interact with the interstellar medium (ISM). There exists several models in the literature. This thesis describes some of them.

The first model is the Active Galactic Nuclei (AGN) model. In [27], it is mentioned that the *Fermi* Bubbles were probably created by a large energy injection from the galactic center in the form of jets. Simulations showed that the AGN model can reproduce the morphology of the *Fermi* Bubbles [51, 52]. It is assumed that the activity of the jets started 1-3 Myr ago and were active for $\sim$0.1-0.5 Myr.

Another model suggests that a cosmic ray population was carried out to the bubble region by winds produced from a long time-scale star formation in the galactic center. It is argued that the observed gamma-ray spectrum can be explained if the cosmic rays are trapped in the bubble region for a time scale of 10^{10} years[53].

A periodic star capture process by the supermassive blackhole in the Galactic Center is proposed in [54]. The model shows that the supermassive black hole, Sagitarius A*, with a star capture rate of 3×10^{-5} yr^{-1}, can release an energy of $\sim 3 \times 10^{52}$ ergs per capture. This produces a hot plasma of energy ~ 10 keV and a wind velocity of $\sim 10^8$ cm s^{-1} that is injected into the bubble region. The periodic injection of the hot plasma produces shocks that can accelerate cosmic ray electrons. Some of these electrons produce gamma rays through inverse Compton scattering.

Another formation mechanism is also related to the activity of Sagitarius A*. In this case, it is assumed that the accretion rate of the black-hole was $10^3 - 10^4$ times higher during the past $\sim 10^7$ years. The hot accretion flow produces a strong wind driven by magnetic forces. Cosmic rays are accelerated inside these winds by different mechanisms. After interacting with the interstellar medium, cosmic rays will produce gamma rays [55].

The production of gamma rays is also under dispute. Hadronic and leptonic models are the main mechanisms to explain the gamma-ray production. Photons from

hadronic origin are due to the decay of neutral pions that are produced in the interaction of protons with nuclei in the Interstellar Medium. These protons are injected in the bubble regions by the outflow processes mentioned before or they can be accelerated inside the bubble as proposed by [56, 57]. Some of these models predict the possibility of high-energy gamma rays[53, 56]. In the leptonic model, high-energy photons are produced by inverse Compton scattering from the interaction of energetic electrons with photons from the interstellar radiation fields or cosmic microwave background. The division between hadronic and leptonic models should not be strict, but rather, a combination of both models may be possible[6, 54]. Observations at other wavelengths, specifically at lower energies, have helped to constrain some models. For instance, the microwave haze, produced by synchrotron radiation, can help to constrain the electron population, which can also radiate in gamma rays [26, 27, 52, 53, 55].

The same principle can apply at high energies, where observations can constrain the population of the highest-energy cosmic rays. The present chapter shows an analysis for searching for high-energy gamma rays (above $\sim 1\,\text{TeV}$) from the Northern *Fermi* Bubble region using data from the HAWC Observatory

5.2   The Data Set

The HAWC observatory began science operations in August 2013, when it was still under construction. The following analysis uses data from between 2014 November 27th to 2016 February 11th. Due to the fact that the analysis requires 24-hour periods of time when the detector is stable, only full days of uninterrupted operation are considered, resulting in a lifetime of the analysis of 290 days. This is because the method of direct integration is used to estimate the background [58], which requires stable periods of operation (See section 5.3.1).

Standard selection cuts are applied to the data that pass the trigger condition. The signals in each PMT should have > 1 photoelectron (PE) and should be between $150 \, \mathrm{ns}$ before and $400 \, \mathrm{ns}$ after the trigger. Then, the data are divided into seven bins which represent the shower footprint brightness and are defined as the fraction of functioning PMT channels triggered in an air shower event. The bins will be denoted as f. The energy of the observed gamma rays is related to the shower footprint size that is measured in the HAWC array. In addition, it is required that more than 90% of the PMT channels are functioning during the observation. The analysis cuts applied are shown in Table 4.2. Only analysis bins 3-9 are used for this analysis due to systematic effects in the lower two bins. Hence, for the purpose of the analysis, the bins will be renamed, and the analysis presented in this chapter will use bins one

through 7.

Finally, cuts are applied to distinguish between gamma rays and cosmic rays, the latter being the main background of measurements with the HAWC observatory. The first gamma-hadron cut is applied to the ratio of the number of triggered PMTs to the number of PEs in the PMT with the highest signal outside of a radius of $40\,\mathrm{m}$ from the estimated core. A higher value of this ratio corresponds to a higher gamma-ray probability of an event. Equation 4.10 is used to obtain this value (See Figure 4.17). The second gamma-hadron cut is applied to an observable that measures the deviation of the charge measured in the PMTs from an average expectation. A lower value of this observable corresponds to a higher gamma-ray probability of an event (See Figure 4.18). Equation 4.11 is used to calculate this second gamma-hadron value. All the cuts are optimized by studying the Crab Nebula in the HAWC data [43]. The value of the gamma-hadron cuts are

```
                              ┌─────────────────┐
 ───────────────────────────  │ Gamma-Hadron Cuts │  ───────────────────────────
                              └─────────────────┘

1 "(rec.nHitSP20/rec.CxPE40>=11.00) && (rec.PINC<2.30)"
2 "(rec.nHitSP20/rec.CxPE40>=15.00) && (rec.PINC<1.90)"
3 "(rec.nHitSP20/rec.CxPE40>=18.00) && (rec.PINC<1.90)"
4 "(rec.nHitSP20/rec.CxPE40>=17.00) && (rec.PINC<1.70)"
5 "(rec.nHitSP20/rec.CxPE40>=15.00) && (rec.PINC<1.80)"
6 "(rec.nHitSP20/rec.CxPE40>=15.00) && (rec.PINC<1.80)"
7 "(rec.nHitSP20/rec.CxPE40>= 3.00) && (rec.PINC<1.60)"
#rec.nHitSP20: number of hits
#rec.CxPE40: maximum charge outside 40m radius from the
#            core of the shower
#rec.PINC: charge smoothness
```

5.3 Analysis

5.3.1 Background Estimation

The position of the events are binned in equatorial coordinates using the HEALPix scheme [59]. For the analysis we set the pixel size to be 0.11°.

The background is estimated using the "direct integration" technique described in [58]. As implied in the previous section, the background is integrated over 24 hours and therefore only data were used when the detector performance was stable for 24 hours.

The direct integration technique uses the actual event distribution of local arrival direction and the integrated rate for the specific period of time. The local arrival distribution is normalized, so it becomes a local detector efficiency $E(ha, \delta)$ for the integration time period, where ha is the hour angle and δ is the declination. This is convolved with the time-integrated rate $R(t)$ to obtain the number of background events, where t is the time of the observation. This is summarized in the following equation:

$$\langle N \rangle (\alpha, \delta) = \int \int E(ha, \delta) R(t) \epsilon(ha, t, \alpha) \, dt \, d\Omega, \qquad (5.1)$$

where α is the right ascension; the variable ϵ ensures that the events from the local position in (ha, δ) corresponds to the equatorial poisiton (α, δ). The integration is done over the time t and the angular size Ω.

As explained in [44], an analysis based on background integration period of Δt is sensitive to potential signal excesses of an RA size smaller than $\Delta t \cdot 15° \, \text{hour}^{-1}$. Using a 24 hour integration period, ensures that the analysis is sensitive to the Fermi Bubbles which extend to $\sim 50^o$ in RA.

Since the estimation of the background can be biased by strong known regions of gamma- and cosmic-ray excesses in the data, a *region of interest* (ROI) masking is used, as shown in Figure 5.2. The ROI masking covers the galactic plane $[\pm 6^o]$, circular regions of $1.3^o, 1^o$, and 1° respectively for the Crab Nebula, Mrk 421, and 501. The small-scale cosmic-ray excesses, Region A and B, are also masked. Their shapes are obtained from the results presented in [44]. Contiguous areas with significances in the cosmic-ray sky map greater than 4σ are excluded from the background calculation. The ROI for the northern *Fermi* Bubble was obtained from the *Fermi* Diffuse Model pass 7 version 6 [1]. The shape at $\sim$TeV is unknown. We perform a gamma-ray flux excess search within the boundaries of the Northern bubble as detected by Fermi

---

[1]See `http://fermi.gsfc.nasa.gov/ssc/data/access/lat/BackgroundModels.html`

below GeV energies.
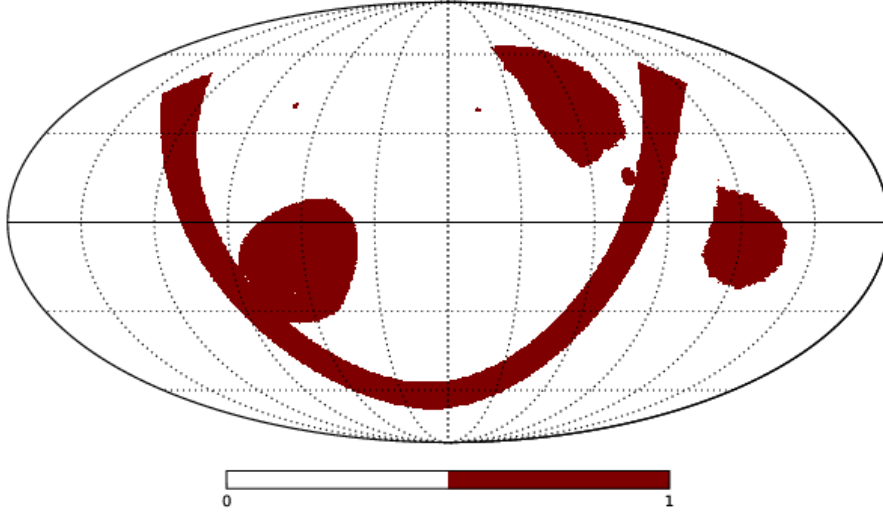
Figure 5.2: Region of interest masking used for the analysis.

5.3.2 Excess Calculation

Large integration time for the background estimation allows to resolve larger structures. Also, since the gamma/hadron separation is not perfect, sky maps at lower f values are affected by the large-scale anisotropy of cosmic rays where the statistics are large enough to be sensitive to the part-per-mille[44]. Figure 5.5 shows an all-sky excess map for all f bins after subtracting the estimated background. Artifacts of the large-scale anisotropy are seen in bins f_1 and f_2. The northern *Fermi* bubble sits on the deficit region. Completely removing the cosmic-ray feature requires maps made without applying the gamma-hadron cuts. The following is a description of our

79

procedure for this removal.

For both, gamma and hadron sky maps, the event excess is calculated by subtracting the direct integration background from the data. The excess in the cosmic-ray maps and the gamma-ray maps are composed of cosmic rays (C) and gamma rays (G), but the composition is different in the gamma-ray maps due to the gamma-hadron cuts. This can be written as

$$
\begin{aligned}
E_C &= N_C - \langle N_C \rangle = C + G \\
E_G &= N_G - \langle N_G \rangle = \varepsilon_C C + \varepsilon_G G,
\end{aligned}
\tag{5.2}
$$

where $N_{C,G}$ are the number of events in cosmic and gamma ray maps, $\langle N_{C,G} \rangle$ are the estimated number of background events in cosmic and gamma ray maps, and ε_C and ε_G are the hadron and gamma passing rates after applying the gamma-hadron cuts. The hadron passing rate efficiency ε_C are obtained from the data assuming that most of the events are cosmic rays $\varepsilon_C = N_G/N_C$.

The gamma passing rate efficiency ε_G is obtained using gamma-ray event simulations assuming a Crab-like spectrum. The detector response is simulated in each of the seven f analysis bins and for 5° declination bands between -37.5^o and 77.5^o. Each

bin contains an energy histogram that is expected for the simulated signal. We compute the total number of events in the energy histograms and the ratio for the events with cuts $h_G(e)$ over the events with no cuts $h_C(e)$. Therefore, the efficiency can be written as:

$$\varepsilon_G = \frac{\int h_G(e)de}{\int h_C(e)de},$$ (5.3)

where e is the energy .

Equation 5.2 can be solved to calculate the number of gammas G.

$$G = \frac{E_G - \varepsilon_C E_C}{\varepsilon_G - \varepsilon_C}.$$ (5.4)

The previous equation is used to calculate the number of gamma rays G in each pixel inside the Northern Bubble region as defined in Figure 5.2 and then summed to get a total excess. The shape of the Fermi Bubbles at high energies is unknown, though some authors suggest that the size of the bubbles increases with energy [55, 56, 60]. In this case, calculating the flux in the smaller region of the MeV-GeV excess is the more conservative approach.

The error calculation for G is obtained through

$$\left(\frac{\delta G}{|G|}\right)^2 = \frac{\langle N_G \rangle + (E_C \varepsilon_C)^2 (2\frac{\langle N_C \rangle}{N_C^2} + \frac{\langle N_G \rangle}{N_G^2})}{(E_G - E_C \varepsilon_C)^2}$$
$$+ \frac{\varepsilon_C^2 (\frac{\langle N_C \rangle}{N_C^2} + \frac{\langle N_G \rangle}{N_G^2})}{(\varepsilon_G - \varepsilon_C)^2} \qquad (5.5)$$

The efficiency ε_G is applied to the number of gamma-ray photons G to obtain the number of excess events measured by the detector. The excess becomes

$$E = \varepsilon_G (G + \delta G). \qquad (5.6)$$

Figure 5.5 shows skymaps for each analysis bin f before and after applying our procedure.

Figure 5.3 shows the results of the summed excess inside the bubble region after applying the procedure on the right side of each compound figure.
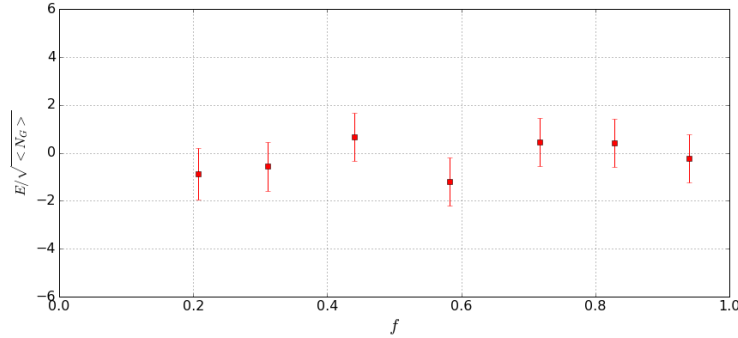
Figure 5.3: Event excess inside the Northern Fermi Bubble region after applying the procedure described in section 5.3.2.

5.3.3   Testing the Analysis Method

The analysis method is tested on simulated sky maps containing a dipole distribution as shown in Figure 5.4 assuming no sources are present. A rate map in the local
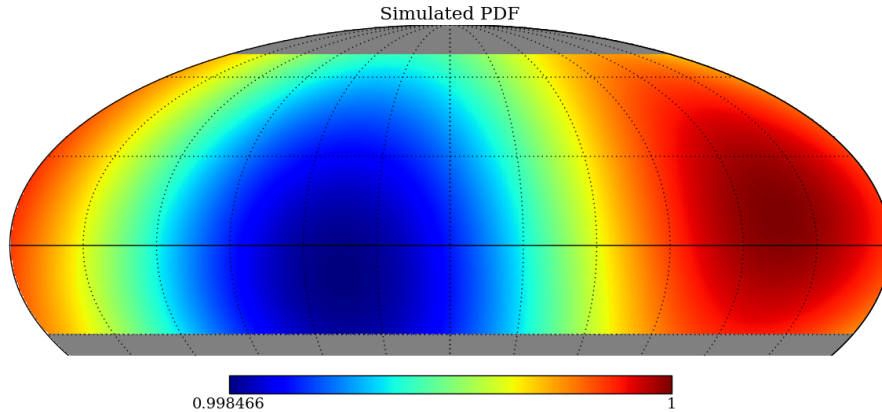
Figure 5.4: Dipole distribution used for the skymap simulation.

coordinates of HAWC containing a snapshot of 24 sec of data is generated. Since HAWC observations cover a local sky of zenith angles $0° < \theta < 45°$, the rate map is generated for this zenith angle range. Using the dipole distribution from Figure 5.4, the total sky event rate from HAWC data, and information from the detector response, a rate in each pixel is obtained. After the 24 sec period the rate map is reset and the procedure is started again. In this way a simulated data set is generated that is of the same size as the real data set analyzed in this chapter. The simulated sky maps shown in Figure 5.7. The left panel in each compound figure represents the resulting map after simply subtracting the estimated background from the data, the

(a) f_1

(b) f_2

(c) f_3

(d) f_4

(e) f_5

(f) f_6

(g) f_7
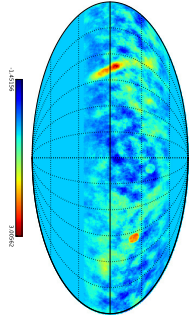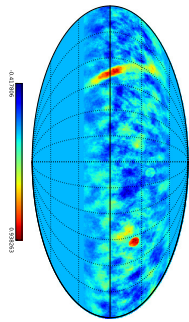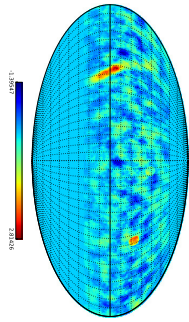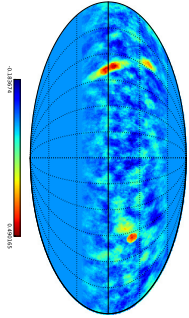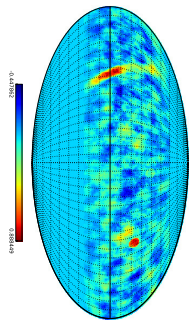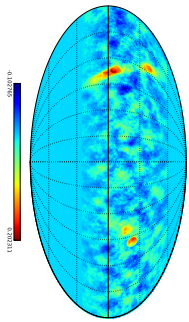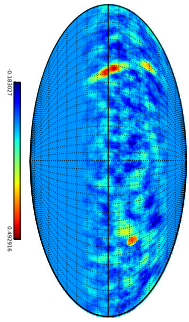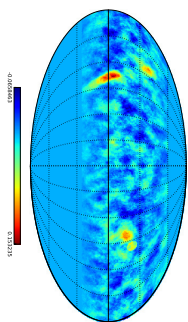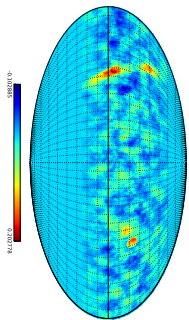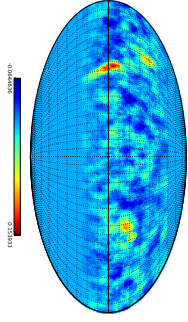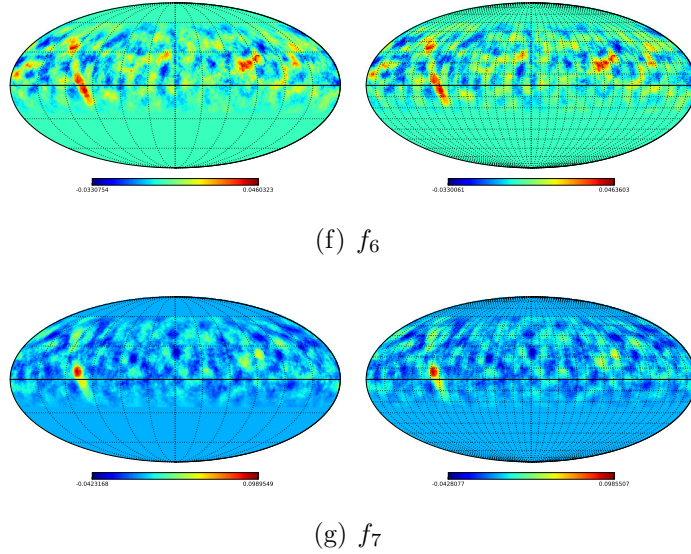
Figure 5.5: Event excess in each analysis bin, smoothed with a 5° tophat. In each figure: On the left the simple excess without removing the large-scale structure. On the right the large-scale structure is removed using the method described in section 5.3.2 (See previous page for the rest of the bins).

lower panel shows the excess map after applying the procedure described in Section 5.3.2. The simulation was repeated 22 times to suppress statistical fluctuations.

Figure 5.6 shows the resulting simulated excesses in each f bin (red points). For comparison, the excesses derived with the simple background subtraction method are also presented —blue points. The effect of the large-scale anisotropy results in systematically lower excesses clearly visible in bins f_1, f_2 and f_4 if the method from Section 5.3.2 is not applied.
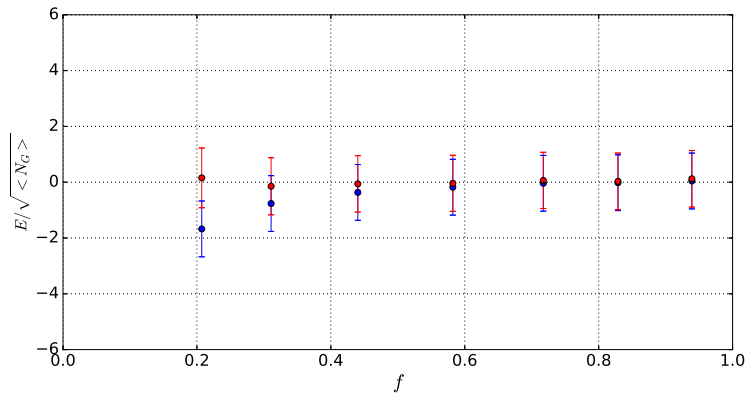
Figure 5.6: Simulated event excess inside the northern bubble region. The effect of the dipole is stronger at lower values of *f*. Blue: Simple Background Subtraction; Red: Method described in Section 5.3.2.

(a) f_1

(b) f_2

(c) f_3

(d) f_4

(e) f_5

(f) f_6

(g) f_7
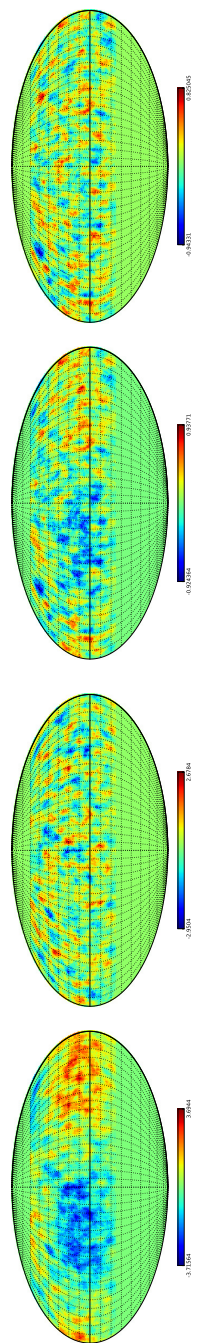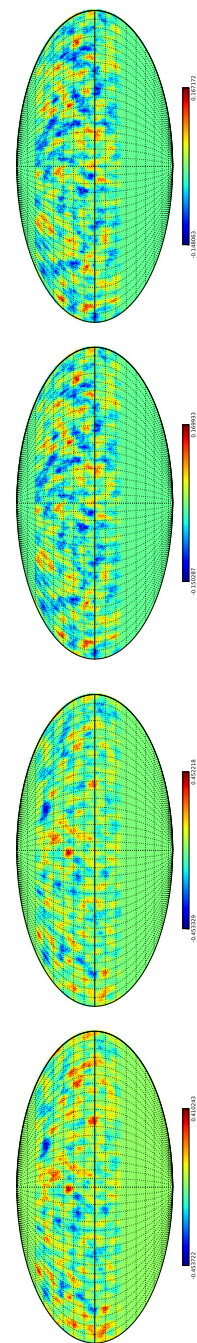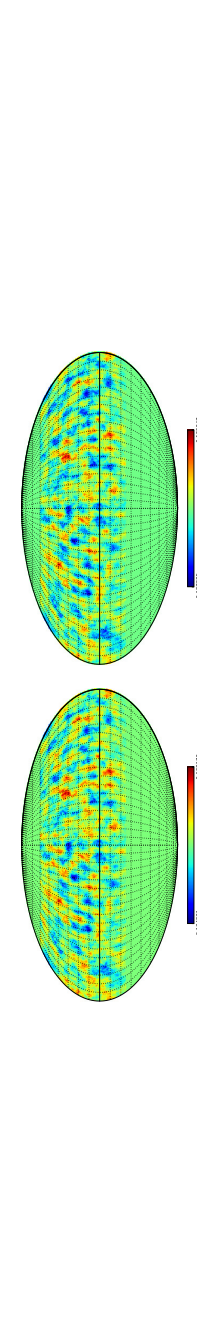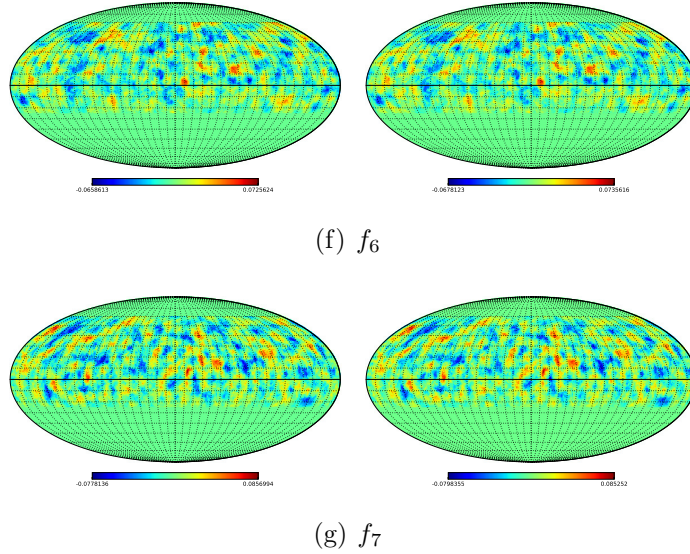
Figure 5.7: Simulated event excess for each analysis bin f, smoothed with a 5°tophat. In each figure: On the left excess after subtracting the estimated background from the fake data. On the right the large-scale structure is removed with the method described in Section 5.3.2.

5.3.4 Describing the non-detection

Figure 5.3 shows that there is no significant excess inside the bubble region, therefore upper limits and sensitivity on the differential flux are calculated.

The upper limit gives the maximum flux intensity that is plausible given the observed counts in the HAWC data. The sensitivity quantifies the power of the detection procedure and are based on finding an α-level threshold (related to background fluctuations claimed as detections) and the probability β to detect a source.
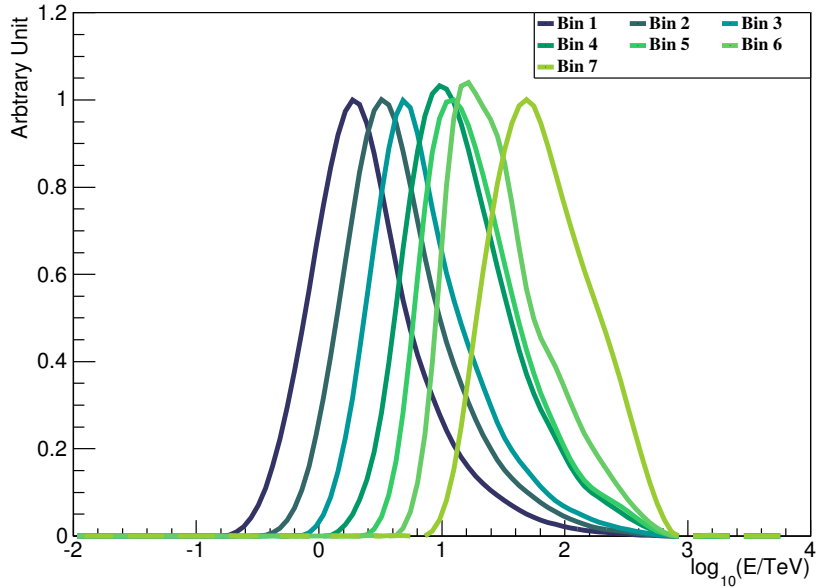
Figure 5.8: Energy histograms for the analysis bins assuming a power-law spectrum with and index $\gamma = 2.75$.

5.3.4.1 Upper Limits

The differential flux is calculated from the measured excess by comparing the signal observed in the data to an expected signal obtained for each of the f bin using simulations. Since the energy response histograms for each analysis bin overlap (see Figure 5.8), the excesses measured in the analysis bins are combined in a weighted sum.

The procedure is as follows: a differential flux is assumed in an energy bin of width $\Delta \log(E/1\,\mathrm{TeV})$. The width of differential energy bins is defined such that the results are independent of spectral assumptions. Using the HAWC detector response, an

expected signal for the Northern bubble region is obtained for each f bin. Taking into account the previous values, the weight in the energy bin k for the f bin i is calculated as:

$$w_i^k = \frac{ME_i^k}{<N_G>_i},$$

(5.7)

where w_i^k is the weight in the energy bin k for the f bin i; ME_i^k is the expected signal in the energy bin k for the f bin i, and $<N_G>_i$ is the background estimated in the f bin i. This procedure results in a matrix that allows to "project" the f analysis bin space onto the energy space.

Using the weights, the ratio of the observed signal and the expected signal is calculated:

$$R_k = \frac{\sum_{i=1}^{7} w_i^k E_i}{\sum_{i=1}^{7} w_i^k ME_i^k},$$

(5.8)

and the uncertainty in the ratio as:

$$\delta R_k = \frac{\sqrt{\sum_{i=1}^{7} (w_i^k \delta E_i)^2}}{\sum_{i=1}^{7} w_i^k ME_i^k}.$$

(5.9)

The ratio is used to obtain an estimation of the flux in the energy bin k:

$$F_k = (R \pm \delta R)_k F(E_k).$$

(5.10)

90

The upper limit (UL) calculation is then performed in the energy bins. The prescription of [61] is used to calculate an upper limit on the differential flux derived from equation 5.10. A 95% confidence level (CL) is chosen.

The procedure consists of finding the value of the upper limit that gives the result

$$1 - \text{CL} = \frac{\int_{UB}^{\infty} e^{-\frac{1}{2}(\frac{x-F}{\sigma})^2} dx}{\int_0^{\infty} e^{-\frac{1}{2}(\frac{x-F}{\sigma})^2} dx}, \tag{5.11}$$

where F is the measured flux, σ is the error in the measurement and the integral is done over the fluxes x.

5.3.4.2 HAWC Sensitivity

The sensitivity is calculated for an α-level of 0.05 with a probability of detection of $\beta = 0.5$[62]. This is in order to compare the power detection of HAWC with the upper limits measured by the data. The calculation is performed by using the measured background and a simulated *Fermi* bubble of varying flux. For the simulation we assume a power-law with an index of -2 in the differential energy bin. For each analysis bin, the total background counts and the total expected number of events from the fake *Fermi* bubble are calculated and summed inside the bubble region. Following the same procedure as in section 5.3.4.1, the analysis bins are combined to get the total number of events for each energy bin. In each energy bin, a null

hypothesis histogram and an alternative hypothesis histogram are created for the quantity

$$S_k = E_k / \sqrt{\langle N_G \rangle_k}, \qquad (5.12)$$

where E_k is obtained by poisson-fluctuating $\langle N_G \rangle_k$ and then subtracting this value to $\langle N_G \rangle_k$ for the null hypothesis, or by poisson-fluctuating $\langle N_G \rangle_k + ME_k$ and then subtracting this value to $\langle N_G \rangle_k$ for the alternative hypothesis. The Poisson fluctuations are performed 10000 times to fill the histograms. The null hypothesis histogram is used to find the α-level detection threshold and the alternative hypothesis histogram is used to find the flux normalization that is required to obtain a probability of detection of 0.5.

5.4   Results and Discussion

The first energy bin is centered at 2.2 TeV, which is the median energy of f_1 assuming a power-law spectrum of index $\gamma = 2.75$ (see Figure 5.8). The energy bin width is set to $\Delta \log(E/1 \text{ TeV}) = 0.5$ which is comparable to the width of the energy histograms. The energy range covers up to the highest energy at which HAWC is sensitive (~ 100 TeV). Figure 5.9 shows the upper limits and Table 5.1 shows the values for each energy bin. The figure also shows the flux measurement of the *Fermi* Bubbles made by the *Fermi* Collaboration [6].

Table 5.1

Characteristics of the non-Detection

Energy Range [TeV]	Upper Limits $[\mathrm{GeV\,cm^{-2}\,s^{-1}\,sr^{-1}}]$	HAWC Sensitivity $[\mathrm{GeV\,cm^{-2}\,s^{-1}\,sr^{-1}}]$
1.2 - 3.9	3.0×10^{-7}	3.3×10^{-7}
3.9 - 12.4	1.0×10^{-7}	1.1×10^{-7}
12.4 - 39.1	0.5×10^{-7}	0.5×10^{-7}
39.1 - 123.7	0.4×10^{-7}	0.3×10^{-7}

Table 5.1 shows the values of the upper limits and sensitivities for each energy bin.

The upper limits obtained from data are consistent with the detection power of

HAWC. Different leptonic and hadronic models are also present in Figure 5.9. Table

5.2 shows the description of the different models presented in Figure 5.9.

Table 5.2

Differential flux models for the *Fermi* Bubbles

Model	Description
Hadronic Model 1	$N_p \propto p^{-2.2}$
Hadronic Model 2	$N_p \propto p^{-2.1} \exp(-pc/14\,\mathrm{TeV})$
Leptonic Model 1	$N_e \propto p^{-2.17} \exp(-pc/1.25\,\mathrm{TeV})$ and IRF at 5kpc
Leptonic Model 2	$N_e \propto p^{-2.17} \exp(-pc/1.25\,\mathrm{TeV})$ and CMB
IceCube Hadronic Model	$N_p \propto p^{-2.25} \exp(-pc/30\,\mathrm{PeV})$

The two leptonic models are obtained from [6]. In these models, the emission is

described by inverse Compton scattering. Two radiation fields are used: the Inter-

stellar Radiation Field (IRF) at 5 kpc above the Galactic Plane and photons from the

Cosmic Microwave Background (CMB). The electron spectrum interacting with the

radiation fields is modeled as a power-law with an exponential cutoff. The spectral

index has a value of $2.17 \pm 0.5^{+0.33}_{-0.89}$ and the cutoff energy is $1.25 \pm 0.13^{+1.73}_{-0.68}$ TeV.

The two cyan hadronic models, also obtained from [6], assume a power-law and a power-law with cutoff for the injection spectrum of the hadrons. These protons interact with the ISM producing neutral pions that decay into gamma rays. The spectrum was obtained using the library cparamlib[2], which implements the cross sections from [63], for the production of gamma rays through hadronic interactions. The spectral index for the power-law is 2.2; the spectral index for the power-law with cutoff is $2.13 \pm 0.01^{+0.15}_{-0.52}$ with a cutoff energy of $14 \pm 7^{+6}_{-13}$ TeV. Using the fit results obtained in [6], we extrapolate the results for the hadronic models above 100 TeV. The upper limits derived from HAWC data exclude the hadronic injection without a cutoff, that best fits the GeV gamma-ray data, above 3.9 TeV.

The hadronic model represented by the red line is obtained from [7]. This model is the counterpart of a neutrino flux model that best fits the IceCube data. The IceCube data corresponds to five events that are spatially correlated with the *Fermi* Bubbles. The differential flux model was obtained by taking into account the flux from both bubbles. Above 10 TeV, the HAWC upper limits exclude the parent proton spectrum predicted from IceCube data.

Early reports such as [53, 56], hinted at the possibility of observing $\sim$TeV gamma

---

[2]`https://github.com/niklask/cparamlib`
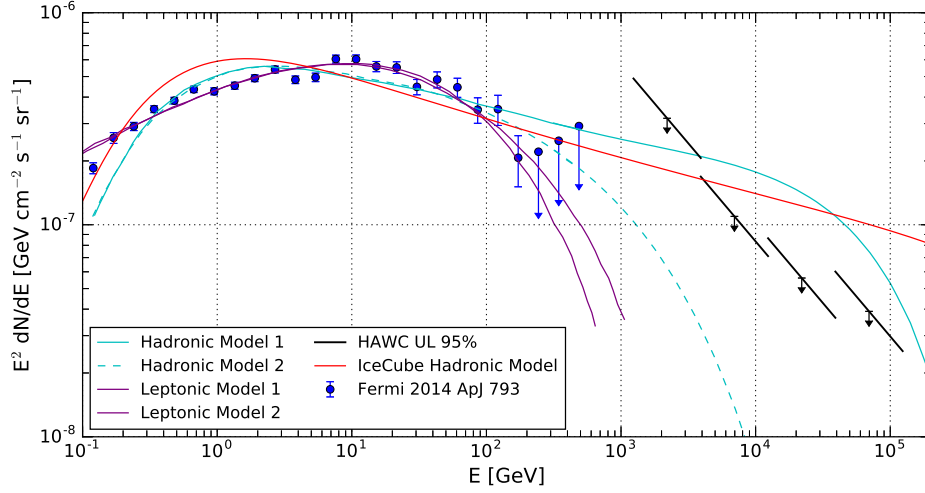
Figure 5.9: HAWC upper limits at 95% C.L. together with the *Fermi* Data and gamma-ray production models from [6] and [7].

rays. The intensity was predicted to be $\leq 10^{-6}$ GeVcm^{-2}s^{-1}sr^{-1}. The result presented here sets a stricter upper limit.

The result does not unambiguously determine the main contribution to the emission of the *Fermi* Bubbles. Nevertheless our result may imply, for a hadronic model, that there is a cutoff in the proton spectrum. A previous publication showed that the GeV gamma-ray spectrum is cutting off around $\sim$100 GeV[6]. The cutoff for the parent proton spectrum in this case could be around $\sim$1 TeV [64].

As mentioned in section 5.3.2, a few papers propose that the size of the bubbles increases with energy [55, 56, 60]. While defining the search region to be the same as the excess detected at GeV energies is a more conservative approach, it may be interesting to increase the size of the latter in a follow-up analysis.

Increasing the sensitivity at energies $< 1\,\mathrm{TeV}$ is another objective for future analyses. At energies $<\sim 1\,\mathrm{TeV}$, the large-scale anisotropy signal (or any significant, spatially-extended feature) causes signal contamination in the estimation of the background because the structure takes up a large portion of the field-of-view of HAWC, significantly altering the all-sky rate. An iterative procedure for the direct integration method will be followed as explained in [65] and has been shown to remove this artifact.

5.5   Conclusions

A search of high-energy gamma rays in the Northern *Fermi* Bubble region has been presented by using 290 days of data from the HAWC observatory. No significant excess is found above $1.2\,\mathrm{TeV}$ in the search area and the 95% C.L. flux upper limits are calculated and compared to the differential sensitivity with $\alpha = 0.05$ and $\beta = 0.5$. The upper limits are between $3\times10^{-7}\,\mathrm{GeV\,cm^{-2}\,s^{-1}\,sr^{-1}}$ and $4\times10^{-8}\,\mathrm{GeV\,cm^{-2}\,s^{-1}\,sr^{-1}}$. The upper limits, for gamma-ray energies between $3.9\,\mathrm{TeV}$ and $120\,\mathrm{TeV}$, disfavor the emission of hadronic models that try to explain the GeV gamma-ray emission detected by the *Fermi* LAT. This makes a continuation of the proton injection above $100\,\mathrm{TeV}$ highly unlikely (solid cyan line in Figure 5.9). The HAWC upper limits also disfavor a hadronic injection spectrum derived from IceCube measurements. The present result does not allow unequivocal conclusions about the hadronic or leptonic

origin of the Fermi bubbles though. A future analysis of HAWC data will include a better sensitivity, especially at lower energies and possibly larger search regions according to the predictions of some theoretical models.

Chapter 6

Large Extended Sources: from Giant Molecular Clouds to Diffuse Emission

In section 1.3.4, it was mentioned that the study of large extended sources in gamma rays is useful for tracing the origin, acceleration, propagation and distribution of cosmic rays throughout the galaxy [66]. The energy density of cosmic rays, $\sim 1\mathrm{eV/cm}^3$, is comparable to that of the galactic magnetic field, $\sim 0.2\mathrm{eV/cm}^3$, and starlight, $\sim 0.5\mathrm{eV/cm}^3$. Hence they are an important constituent in the energy budget of the ISM and a key component to understand the history and evolution of the galaxy[67].

This chapter presents preliminary results of simulations and analysis of HAWC data for the study of these large extended gamma-ray sources.

The first section is a summary of radiative transfer. It is presented in order to understand some of the measurements of the galactic surveys that are then used to estimate the amount of gas in the galaxy. The coupling of the cosmic-ray flux with the gas produces the gamma-ray flux.

6.1 Radiative Transfer[1]

If we imagine a set of rays crossing a differential surface dA, the amount of energy crossing in dt time is:

$$dE = I_\nu \, dA \, dt \, d\Omega \, d\nu \tag{6.1}$$

where I_ν is the specific intensity, ν is the frequency of the light, $d\Omega$ is the solid angle subtended by the differential area dA. In empty space, the specific intensity remains constant, however, in the presence of matter, energy can be added or subtracted by emission, absorption or scattering. The change of the specific intensity on a distance s in the presence of matter is given by:

$$\frac{dI_\nu}{ds} = j_\nu - \alpha_\nu I_\nu \tag{6.2}$$

---

[1]For a detailed description see [68]

where j_ν is the emission coefficient and α_ν is the absorption coefficient. The optical depth τ_ν is a measure of the level of transparency in a cloud. It is defined as $d\tau_\nu = \alpha_\nu ds$ and this can be used to redefine equation 6.2. The intensity radiation equation then becomes:

$$\frac{dI_\nu}{d\tau_\nu} + I_\nu = S_\nu \tag{6.3}$$

where S_ν is the source radiation intensity.

For a constant source radiation intensity, the solution is written as

$$I_\nu = I_\nu(0)e^{-\tau_\nu} + S_\nu(\tau_\nu)(1 - e^{-\tau_\nu}) \tag{6.4}$$

Since most survey measurements are in the radio region of the electromagnetic spectrum, we can use the Rayleigh-Jeans approximation. This makes the source radiation intensity become

$$S_\nu(\tau_\nu) = \frac{2KT_{Spin}\nu^2}{c^2} \tag{6.5}$$

where T_{Spin} occurs when there is thermal equilibrium between the two spin states of atomic hydrogen. The specific intensity can also be converted to a brightness temperature:

$$T_\nu \equiv \frac{c^2}{2K\nu^2}I_\nu \tag{6.6}$$

With these two equations, equation 6.4 becomes

$$T(\tau_\nu) = T(0)e^{-\tau_\nu} + T_{Spin}(1 - e^{-\tau_\nu}) \tag{6.7}$$

Generally, instruments measure $\Delta T = T(\tau_\nu) - T(0)$, i.e.

$$\Delta T = (T_{Spin} - T(0))(1 - e^{-\tau_\nu}), \tag{6.8}$$

which is used to obtain the total optical depth.

$$\tau_\nu = -\ln\left(1 - \frac{\Delta T}{T_{Spin} - T(0)}\right). \tag{6.9}$$

6.2   Giant Molecular Clouds

Giant Molecular Clouds (GMC) are dense regions in interstellar space composed mainly of cold, dark dust and molecular gas —mostly hydrogen and helium. The GMC have masses of $10^4 - 10^6$ $M_\odot$ and sizes of 50-200 pc. These are important regions for the evolution of the galaxy since it is where star formation occurs.

The observation of the GMCs is done either in the radio or infrared, since visible light is not able to penetrate these dense regions. GMCs are made mostly of molecular
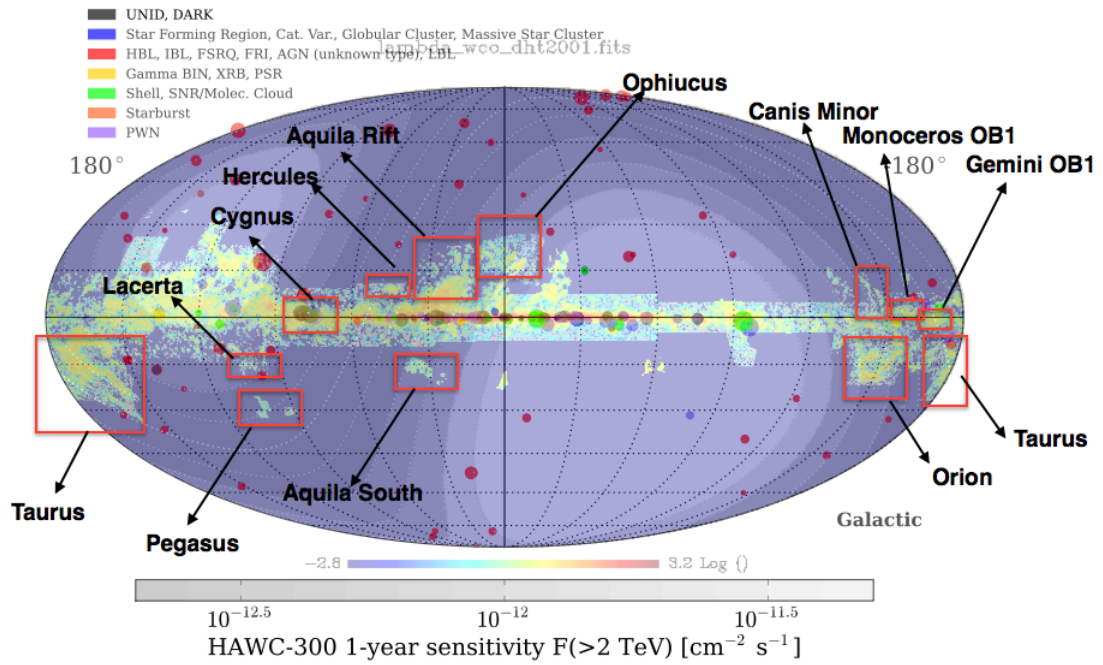
Figure 6.1: GMC obtained from the CfA 1.2m millimeter-wave Telescope survey. The survey is overlayed with the 1-year HAWC sensitivity.

hydrogen, however, since the molecule does not have a permanent electric dipole, it does not emit light. Fortunately there are other type of molecules that are used as tracers of molecular gas. One of these molecules is CO. CO presents a lower frequency rotational transition that emits radiowaves at 115GHz. Using two 1.2 m telescopes, one at the Center-for-Astrophysics (CfA) in Harvard and the other at Cerro Tololo in Chile, a CO survey of the galaxy was made [9] and it is shown in figure 6.1.

6.3　Galactic Diffuse Emission

The galactic diffuse emission is gamma-ray emission that is produced by the interaction of cosmic rays with interstellar matter and interstellar radiation fields. GMCs are part of the diffuse emission since they provide the target material for the production of gamma rays through pion decay.

Also, beside the molecular hydrogen located in the GMCs, atomic hydrogen is distributed all over the galaxy. Atomic hydrogen is observed by looking for the 21cm emission line. This emission is produced by the magnetic interaction of the proton and electron in the hydrogen atom. A photon is emitted when the relative spins change from parallel to antiparallel. One of the most frequently used surveys to model the diffuse gamma-ray emission is the Leiden/Argentine/Bonn (LAB) survey [8]. The survey uses data from radiotelescopes in the Netherlands and Argentina. The data was then corrected for stray radiation (light that is not intended to be detected) by scientists at the University of Bonn.

Equation 1.19 shows how to calculate the gamma-ray flux for hadronic interactions. The column density n_H is defined as:

$$n_H = N_{HI} + 2N_{H_2}.$$
(6.10)

Atomic Hydrogen

The column density for atomic hydrogen, N_{HI}, is obtained from

$$N_{HI} = 1.82 \times 10^{22} \int_{-\infty}^{\infty} T_{Spin} \tau(v) dv \quad [m^{-2}],$$

(6.11)

where v is the radial velocity of the cloud. Using equation 6.9, 6.11 becomes

$$N_{HI} = -1.82 \times 10^{18} \int_{-\infty}^{\infty} T_{Spin} \ln \left(1 - \frac{\Delta T}{T_{Spin} - T(0)} \right) dv \quad [cm^{-2}],$$

(6.12)

ΔT is obtained directly from the LAB survey [8]. However, if $\Delta T > T_{Spin} - 5K$ then ΔT is truncated to $T_{Spin} - 5K$.

Molecular Hydrogen

From the CfA survey [9] we have information of the brightness temperature and velocity. Then integrated brightness temperature is of the CO emission is defined as:

$$W_{CO} = \int_{-\infty}^{\infty} T \, dv.$$

(6.13)

Empirical models suggest that the integrated brightness temperature is roughly pro-portional to the mass of the cloud and hence the column density[68]. The proportionality factor is defined as:

$$X_{CO} = \frac{N_{H_2}}{W_{CO}}, \tag{6.14}$$

which is of the order of $\sim 10^{20}$ cm^{-2} K^{-1} (km s^{-1})$^{-1}$ so the final equation to obtain the column density for molecular hydrogen is

$$N_{H_2} = X_{CO} \int_{-\infty}^{\infty} T \, dv \quad [cm^{-2}]. \tag{6.15}$$

The total column density from atomic and molecular hydrogen is shown in figure 6.2
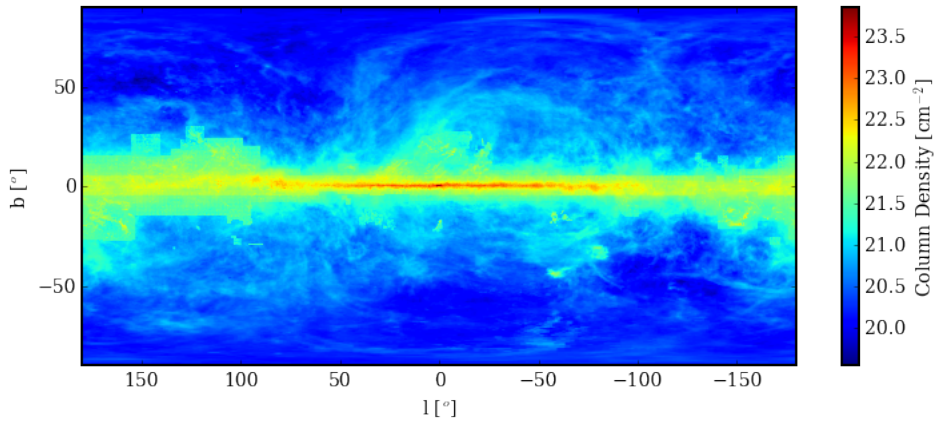
Figure 6.2: Column Density of Hydrogen after combining the atomic and molecular contributions

Equation 1.20 can then be used to calculate the emissivity of pions. The cross section

of the interaction has been calculated with different approximations. One of these

approximations is presented in [69]. The emissivity of gamma rays per solid angle is

shown in figure 6.3.
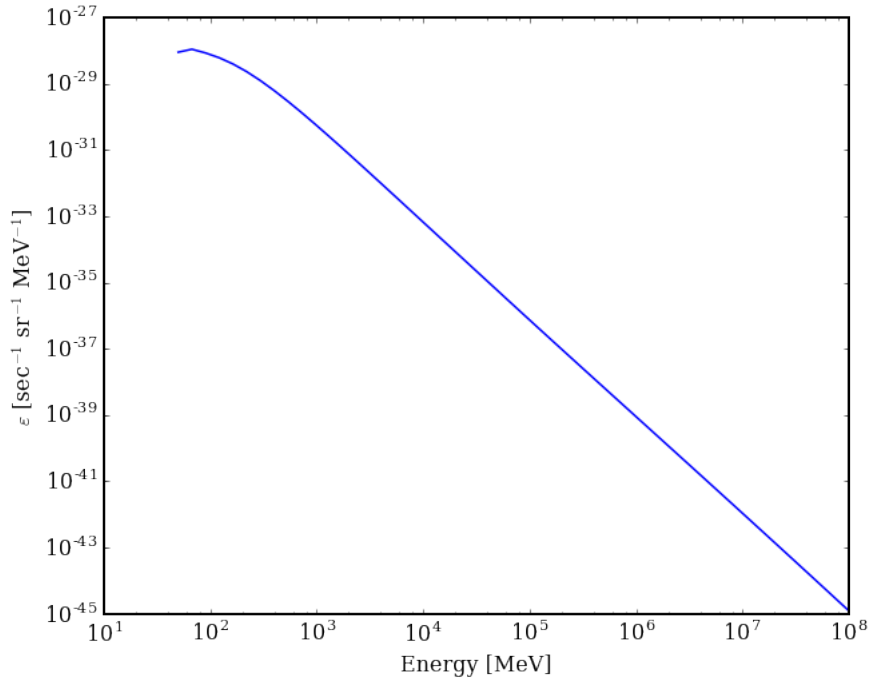
Figure 6.3: Emissivity of gamma rays versus energy.

Finally, the flux of gamma rays can be calculated by multiplying the gamma-ray

emissivity 1.19 by the column density of hydrogen (both atomic and molecular) 6.10.

The contribution from pion decay is obtained by combining the contributions from

the atomic and molecular hydrogen. This is a first principles estimation, since the

estimated flux of gamma rays from pion decay comes from other observations of the

galaxy in different wavelengths.

The other contributions to the Galactic Diffuse Emission at VHEs are inverse Compton scattering and bremsstrahlung. In the case of bremsstrahlung, the emission of gamma-rays also follows the gas distribution due to the interaction of electrons with matter. For inverse Compton scattering, the distribution is smoother since electrons interact with the radiation fields. Several simulation packages have been developed to estimate the gamma-ray flux for different physical processes. One of these is know as GALPROP[10]. GALPROP solves a diffusion equation for cosmic rays and simulates the interaction of these with the interstellar matter and interstellar radiation. It then provides a estimated flux for inverse Compton, bremsstrahlung, and pion decay.

Figure 6.4 show the estimated flux of gamma rays from the Galactic Diffuse Emission for the combination of the pion decay model from the gas maps, and the inverse Compton and Bremstrahlung from GALPROP, and the full GALPROPT model. A comparison of the two pion decay models is shown in figure 6.5.

6.3.1 Preliminary Analysis: Studies of Diffuse Emission

In order to estimate how much Galactic Diffuse Emission HAWC can detect, a rough estimate was calculated using early simulations of the HAWC detector.

The simulation first creates signal events that HAWC will detect using its response functions. A background signal was also simulated and the signal-to-noise ratio or
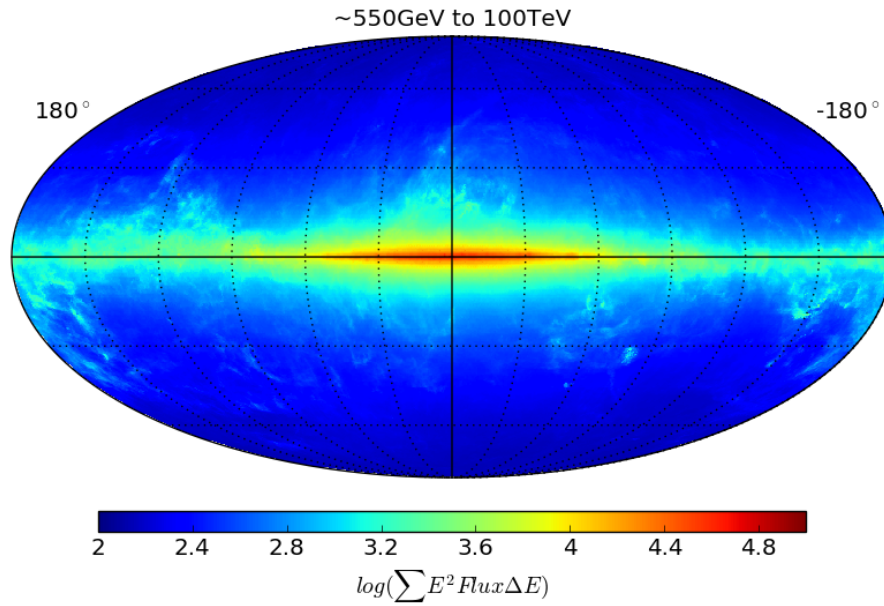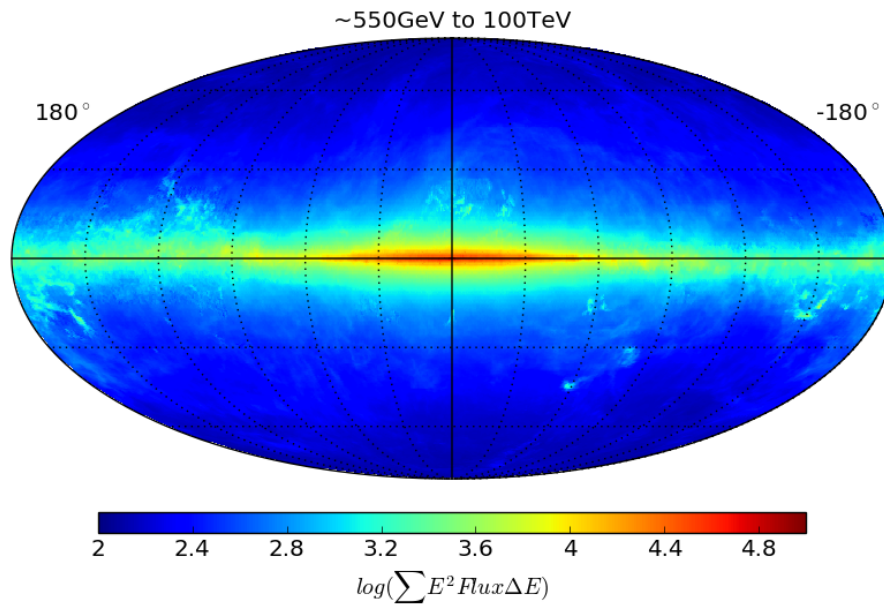
Figure 6.4: Diffuse Galactic Emission flux. The first figure uses the pion decay contribution from the LAB[8] and CfA[9] surveys and inverse Compton scattering and bremsstrahlung from GALPROP[10]. The second figure uses the whole GALPROP model.
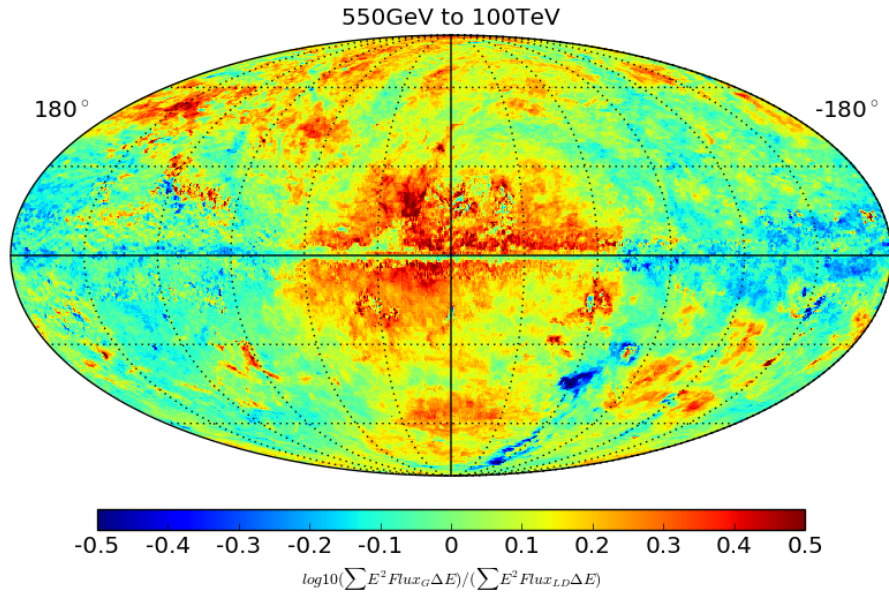
Figure 6.5: Comparison of the gamma-ray flux from pion decay for the LAB[8] and CfA[9] gas-map model, and GALPROP Model.

significance was calculated. The simulation was done for a period of 3 years.

The results of both models is shown in figures 6.6 and 6.7. The figures are in galactic coordinates.

The simulation shows that a detection of the Galactic Diffuse Emission is possible after 3 years of observations.

GalProp

Galactic

0   N_{events} 519

LAB-Dame

Galactic

0   N_{events} 519
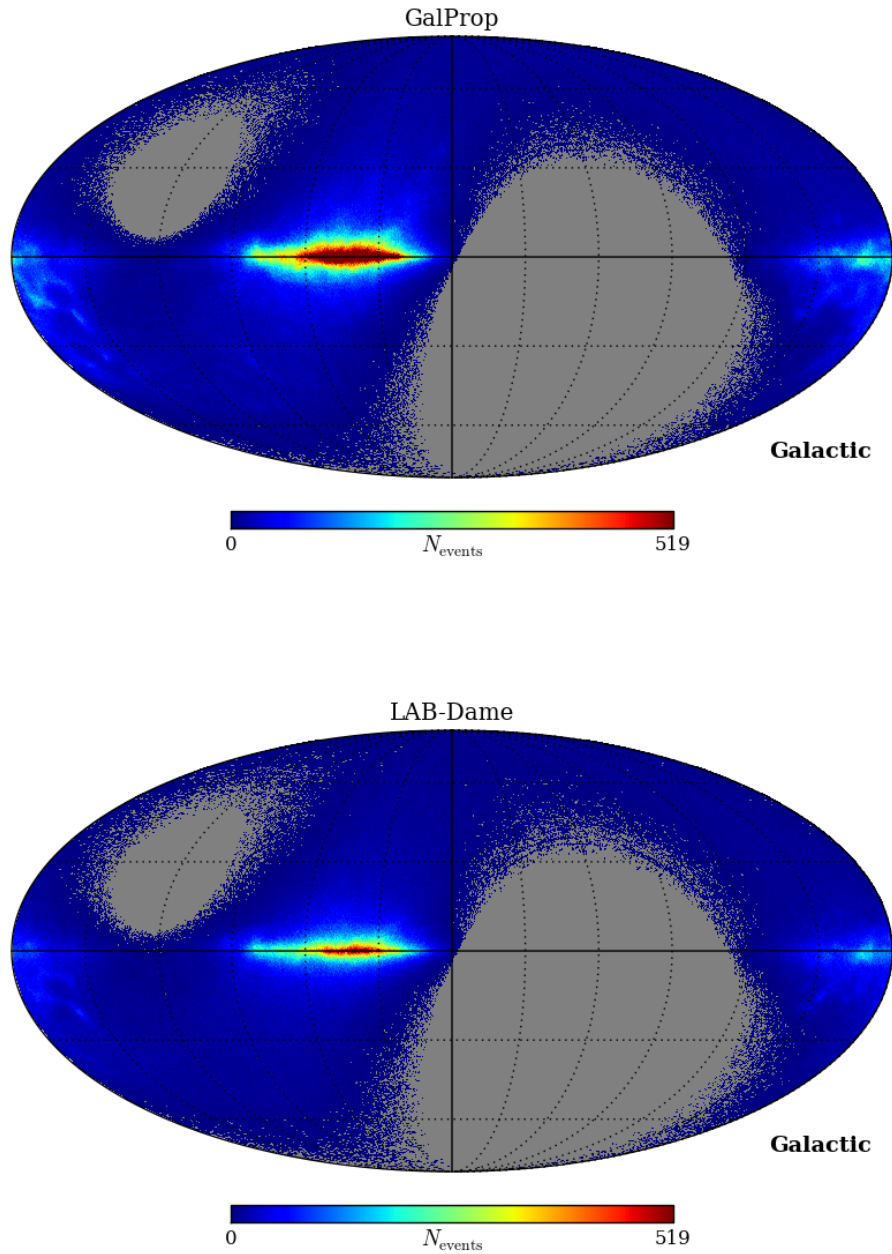
Figure 6.6: Expected number of gamma-ray events by HAWC in three years using the GALPROP model and the first principles model. The color scale is the same for both maps. Higher prediction of events is expected from GALPROP as shown in figure 6.4. The simulation also includes Regions A and B from the small-scale Anisotropy.
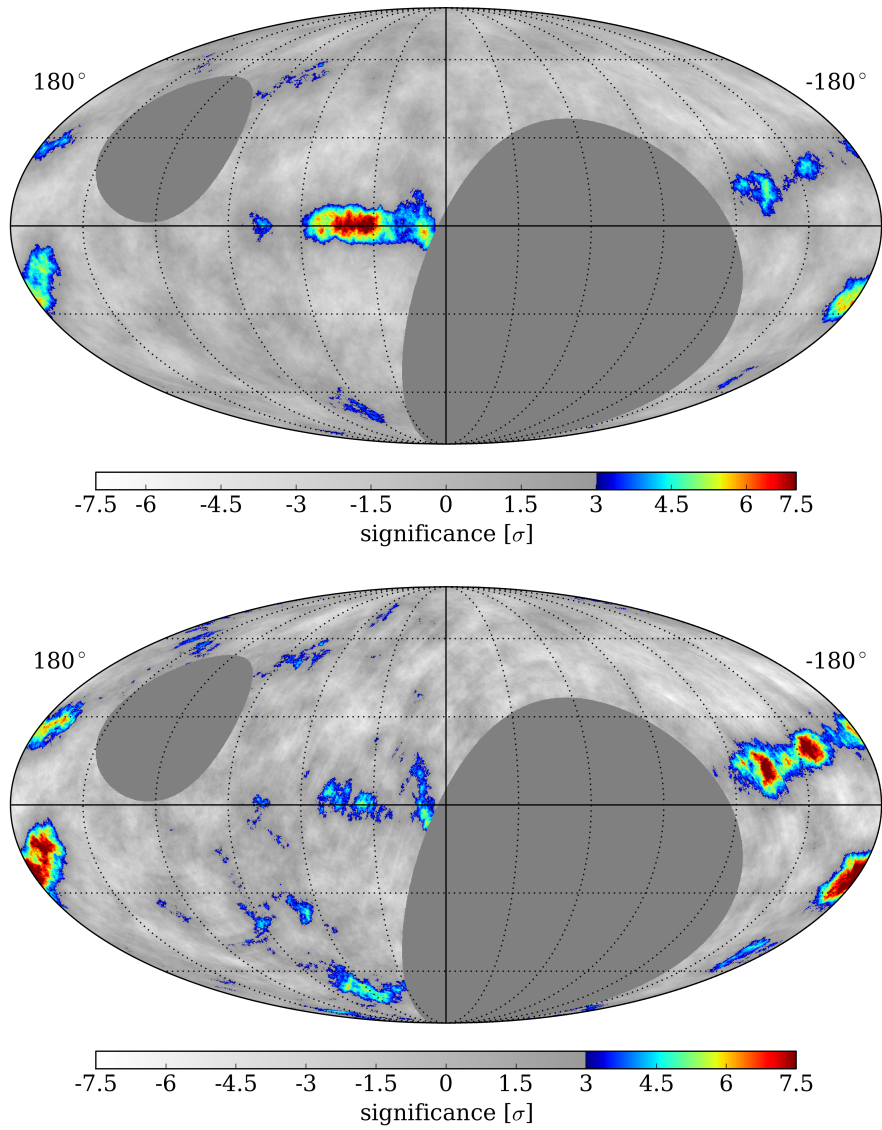
Figure 6.7: Significance maps of 3 years of simulation for both Galactic Diffuse Emission Models. Top: GALPROP Model. Bottom: LAB and CfA Model.

6.3.2   Preliminary Analysis: Molecular Clouds

The gamma-ray visibility of GMCs, assuming that gamma rays are produced by the interaction of cosmic rays with the gas, is determined by

$$F_\gamma(\leq E_\gamma) \simeq 10^{-7} \left(\frac{M_5}{d_{kpc}^2} \right) q_{-25}(\leq E_\gamma)\,\mathrm{cm}^{-2}\,\mathrm{s}^{-1}, \qquad (6.16)$$

where $q_{-25}(\leq E_\gamma) = q_\gamma(\leq E_\gamma)/10^{-25}\mathrm{H\text{-}atom}^{-1}\,\mathrm{s}^{-1}$ is the gamma-ray emissivity; $M_5 = M/10^5 M_\odot$ is the mass of the GMC; and $d_{kpc} = d/1\,\mathrm{kpc}$[23]. In a passive GMC —a cloud submerged in the already diffused cosmic rays— the gamma-ray flux of GMC above $1\,\mathrm{TeV}$ is approximated by

$$F_\gamma(\leq E_\gamma) \simeq 1.45 \times 10^{-13} \left(\frac{E}{1\,\mathrm{TeV}} \right)^{-1.6}\,\mathrm{cm}^{-2}\,\mathrm{s}^{-1}, \qquad (6.17)$$

assuming that the cosmic ray flux is the same as the flux measured at Earth, given by

$$F_{CR}(E) = 2.2 \left(\frac{E}{1\,\mathrm{GeV}} \right)^{-2.75}\,\mathrm{cm}^{-2}\,\mathrm{s}^{-1}\,\mathrm{sr}^{-1}\,\mathrm{GeV}^{-1}. \qquad (6.18)$$

In the case that there is any particle accelerator inside the cloud, an increase in the flux measurement can be detected.

Using equation 6.17 and the CO maps from figure 6.1, we can look for clouds that

are outside the galactic plane and which have a high probability of not having any particle accelerators. The flux estimates from three different clouds are presented in this chapter. These estimates are compared to upper limits calculations obtained from the same procedure as described in section 5.3.4.2, but for circular regions of radius 3° and 5°. The upper limits (or detector sensitivity) are plotted as function of declination.

The skymaps presented in this chapter were made with a two-hour background integration period. The corresponding time for this analysis is 507 days of data.

6.3.2.1   Aquila Rift

Aquila Rift is located (in galactic coordinates) between $10^o < l < 35^o$ and $0^o < b < 16^o$. It is located at a distance of $225 \pm 55 \, \mathrm{pc}$[70] and a mass of $1.5 \times 10^5 \, M_\odot$[71]. Figure 6.8 shows the estimated flux using equation 6.17 and the upper limits for 2 and 5 years of observations. The partial skymap contains a contour of the molecular map from Figure 6.1 with a value of $\log_1 0(N_{H_2}[\mathrm{cm}^{-2}]) = 21.15$. The color scheme is the significance, related to the signal-to-noise ratio.
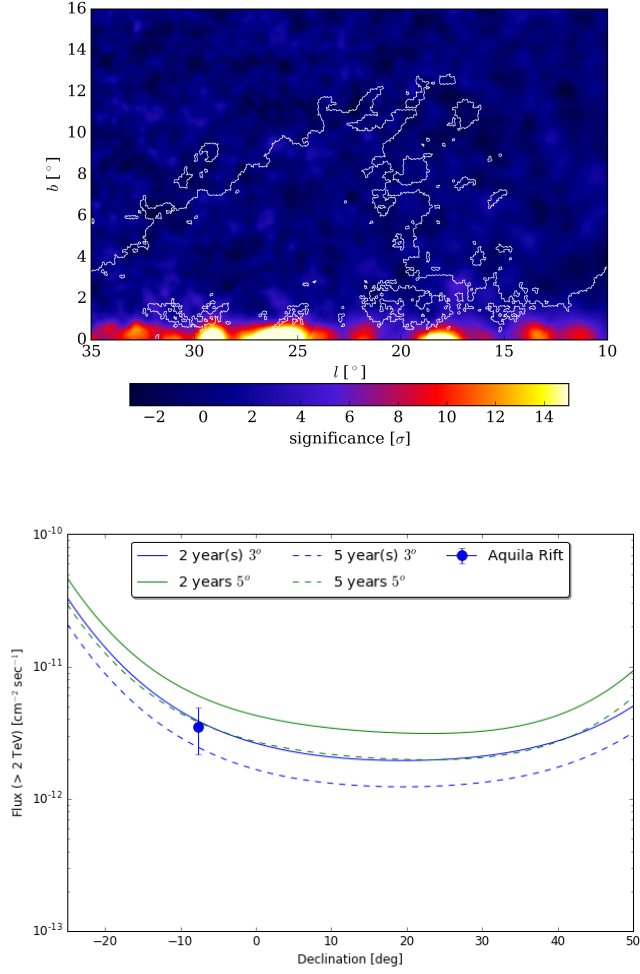
Figure 6.8: Aquila Lift. Flux estimate and flux upper limits for HAWC observations for 2 and 5 years.

6.3.2.2 Hercules

Hercules is located (in galactic coordinates) between $40^o < l < 48^o$ and $5^o < b < 13^o$, well above the galactic plane. It is located at a distance of $200 \pm 30\,\mathrm{pc}$[70]. However, no mass measurement was found in the literature so the mass of the cloud is assumed
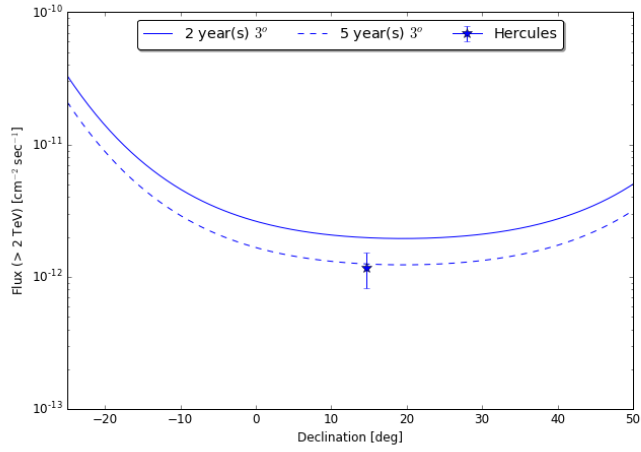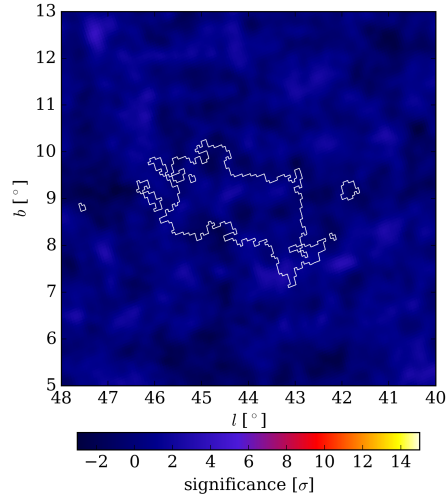
Figure 6.9: Hercules. Flux estimate and flux upper limits for HAWC observations for 2 and 5 years.

to be $0.5 \times 10^5 \, M_\odot$. Figure 6.9 shows the estimated flux using equation 6.17 and the upper limits for 2 and 5 years of observations.

6.3.2.3 Taurus

Taurus is located (in galactic coordinates) between $150^o < l < 175^o$ and $-2.5^o < b < 27.5^o$. It is located at a distance of $140 \pm 30\,\mathrm{pc}$[70] and a mass of $0.2 \times 10^5\,M_\odot$[71]. Figure 6.10 shows the estimated flux using equation 6.17 and the upper limits for 2 and 5 years of observations.

As it can be seen from the skymaps, no significant excess has been observed in these regions. A non-detection by HAWC, by at least 5 years in the most optimistic cases, would mean that the cosmic-ray flux at far distances is lower than the measured cosmic-ray flux at Earth.
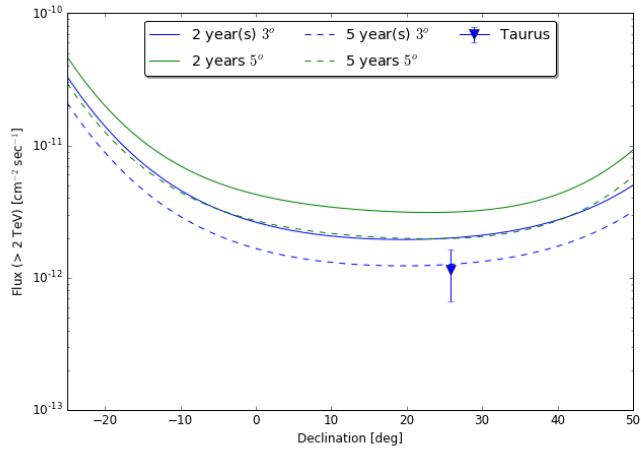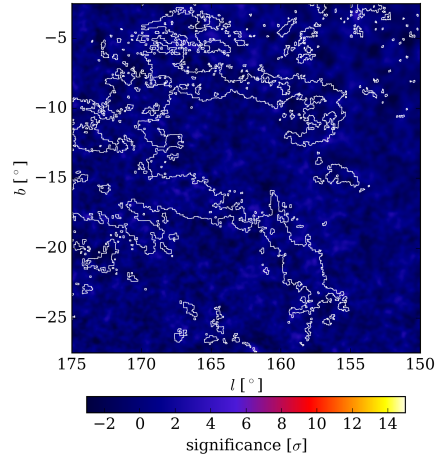
Figure 6.10: Taurus. Flux estimate and flux upper limits for HAWC observations for 2 and 5 years.

Chapter 7

Conclusions

7.1 Search for VHE Gamma-Ray Signal in the Northern Fermi Bubble Region – Summary

Chapter 5 presented a search for a VHE gamma-ray signal in the Northern Fermi Bubble region above $\sim 1\,\mathrm{TeV}$. With a large field of view and a high duty cycle, HAWC data constrains the possible hadronic models that can explain the flux of the Fermi Bubbles. The dataset was obtained during the time interval from November 27th 2014 to February 11th 2016. Only 290 days were used in order to ensure 24-hour periods of stable data taking for the estimation of the background. The search did not find a significant excess, so the upper limits with 95% C.L. were calculated.

At $\sim$40 TeV, the constraint on the flux is $\sim 4 \times 10^{-8}$ GeV cm^{-2} s^{-1} sr^{-1}. Several hadronic models, such as the one presented in [6] or [7], were ruled out by the HAWC upper limits. However, the sensitivity is still too low to be able to say anything about leptonic models. Currently, an improvement of the analysis at energies below 1 TeV is under study. Improving the background estimation and the gamma-hadron separation can reduce the systematic effect from the large-scale anisotropy of cosmic rays.

7.2   Large Extended Sources Summary

The search for VHE gamma rays from large extended sources is one of the most useful tools gamma-ray astronomy can offer to the science of cosmic rays. Due to the interaction of cosmic rays with the interstellar matter and interstellar radiation fields, the study of their origin, acceleration and propagation can be done by using gamma-ray data.

Chapter 6 showed preliminary results of sensitivity studies of the Galactic Diffuse Emission. Two different diffuse models were presented with the significance sky map distribution for 3 years of observation with the HAWC observatory. A possible detection of the diffuse emission in some parts of the galactic plane is plausible.

Also, sensitivities for the detection of extended sources, specifically GMCs, were presented. A non-detection by HAWC would mean cosmic-ray flux is lower than measured at Earth.

7.3   The outlook for HAWC

HAWC has been operating since 2014 with a partial set of the array and was able to surpass the detection sensitivity of its predecessor, MILAGRO. Even more, new smaller detectors are being built around the main HAWC array (so-called outriggers) in order to study higher energy gamma rays. More highly-energetic gamma ray showers tend to cover the whole array and their cores often land outside the main array. The new detectors will help to locate the cores of these highly energetic showers and improve the angular resolution at energies > 10TeV.

References

[1] R. C. Hartman and et al, *The Third EGRET Catalog of High-Energy Gamma-Ray Sources*, *APJS* **123** (1999) 79–202.

[2] M. Ackermann et al., *Fermi large area telescope third source catalog*, *APJS* **218** (Jan, 2015) [`arXiv:1501.0200`].

[3] D. Heck, J. Knapp, J. N. Capdevielle, G. Schatz, and T. Thouw, *CORSIKA: A Monte Carlo Code to Simulate Extensive Air Showers*, 1998.

[4] M. Rao and S. B. V., *Extensive Air Showers*. World Scientific, 1998.

[5] H. A. A. Solares, H. Zhou, et al., *Timing Calibration of the HAWC Observatory*, in *Proceedings 33rd ICRC*, 2013.

[6] M. Ackermann, A. Albert, et al., *The Spectrum and Morphology of the Fermi Bubbles*, *ApJ* **793** (2014), no. 1 64.

[7] C. Lunardini, S. Razzaque, and L. Yang, *Multimessenger study of the Fermi*

bubbles: Very high energy gamma rays and neutrinos, Phys. Rev. D **92** (Jul, 2015) 021301.

[8] P. M. W. Kalberla, W. B. Burton, D. Hartmann, E. M. Arnal, E. Bajaja, R. Morras, and W. G. L. Pöppel, *The Leiden/Argentine/Bonn (LAB) Survey of Galactic HI. Final data release of the combined LDS and IAR surveys with improved stray-radiation corrections*, AAP **440** (Sept., 2005) 775–782, [astro-ph/0504140].

[9] T. M. Dame, D. Hartmann, and P. Thaddeus, *The Milky Way in Molecular Clouds: A New Complete CO Survey*, ApJ **547** (Feb., 2001) 792–813, [astro-ph/0009217].

[10] A. E. Vladimirov, S. W. Digel, G. Jóhannesson, P. F. Michelson, I. V. Moskalenko, P. L. Nolan, E. Orlando, T. A. Porter, and A. W. Strong, *GALPROP WebRun: An internet-based service for calculating galactic cosmic ray propagation and associated photon emissions*, Computer Physics Communications **182** (May, 2011) 1156–1161, [arXiv:1008.3642].

[11] A. U. Abeysekara, A. Albert, R. Alfaro, et al., *Search for Very High Energy Gamma Rays from the Northern Fermi Bubble Region with HAWC*, ArXiv e-prints (Mar., 2017) [arXiv:1703.0134].

[12] F. Aharonian, *Very High Energy Cosmic Gamma Radiation*. World Scientific, 2004.

[13] A. R. Bell, *Cosmic-Ray Acceleration*, *Astroparticle Physics* **43** (2013) 56–70.

[14] G. R. Blumenthal and R. J. Gould, *Bremsstrahlung, Synchrotron Radiation, and Compton Scattering of High-Energy Electrons Traversing Dilute Gases*, *Reviews of Modern Physics* **42** (apr, 1970) 237–270.

[15] A. Hewish, S. J. Bell, J. D. H. Pilkington, P. F. Scott, and R. A. Collins, *Observation of a Rapidly Pulsating Radio Source*, *NAT* **217** (Feb., 1968) 709–713.

[16] G. Dubus, *Gamma-ray binaries and related systems*, *The Astronomy and Astrophysics Review* **21** (2013), no. 1 1–71.

[17] F. Aharonian et al., *Discovery of the binary pulsar PSR B1259-63 in very-high-energy gamma rays around periastron with HESS*, *AAP* **442** (Oct., 2005) 1–10, [astro-ph/0506280].

[18] F. Aharonian et al., *Discovery of Very High Energy Gamma Rays Associated with an X-ray Binary*, *Science* (2005).

[19] J. Albert et al., *Variable Very-High-Energy Gamma-Ray Emission from the Microquasar LS I +61 303*, *Science* **312** (June, 2006) 1771–1773, [astro-ph/0605549].

[20] J. A. Hinton et al., *HESS J0632+057: A New Gamma-Ray Binary?*, *ApJ* **690** (Jan., 2009) L101–L104, [arXiv:0809.0584].

[21] R. H. D. Corbet et al., *1FGL J1018.6-5856: a New Gamma-ray Binary, The Astronomer's Telegram* **3221** (Mar., 2011).

[22] M. Ackermann, M. Ajello, W. B. Atwood, et al., *Fermi-LAT Observations of the Diffuse -Ray Emission: Implications for Cosmic Rays and the Interstellar Medium, The Astrophysical Journal* **750** (2012), no. 1 3.

[23] F. Aharonian and et al., *High energy astrophysics with ground-based gamma ray detectors, Rep. Prog. Phys.* **71** (2008).

[24] S. Casanova et al., *Molecular Clouds as Cosmic-Ray Barometers, Publications of the Astronomical Society of Japan* **62** (2010), no. 3 769–777, [http://pasj.oxfordjournals.org/content/62/3/769.full.pdf+html].

[25] R.-z. Yang, E. de Oña Wilhelmi, and F. Aharonian, *Probing cosmic rays in nearby giant molecular clouds with the Fermi Large Area Telescope, AAP* **566** (June, 2014) A142, [arXiv:1303.7323].

[26] G. Dobler, D. P. Finkbeiner, I. Cholis, T. R. Slatyer, and N. Weiner, *The Fermi Haze: A Gamma-Ray Counterpart to the Microwave Haze, ApJ* **717** (2010) 825–842.

[27] M. Su, T. R. Slatyer, and D. P. Finkbeiner, *Giant Gamma-Ray Bubbles From Fermi -Lat: Active Galactic Nucleus Activity or Bipolar Galactic Wind?, ApJ* **724** (2010), no. 2 1044–1082, [arXiv:1005.5480].

[28] T. Piran, *The physics of gamma-ray bursts, Rev. Mod. Phys.* **76** (Jan, 2005) 1143–1210.

[29] W. L. Kraushaar and G. W. Clark, *Search for Primary Cosmic Gamma Rays with the Satellite Explorer XI, Phys. Rev. Lett.* **8** (1962) 106–109.

[30] W. H. Warren, Jr., *Catalog of SAS-2 gamma-ray observations (Fichtel, et al. 1990).* NASA, July, 1990.

[31] B. N. Swanenburg, *Gamma ray astronomy with COS-B, Annals of the New York Academy of Sciences* **375** (1981) 381–390.

[32] P. K. Grieder, *Extensive Air Showers.* Springer, 2010.

[33] T. Weekes, *Very High Energy Gamma-Ray Astronomy.* CRC Press, 2003.

[34] P. G. Edwards, R. J. Protheroe, and E. Rawinski, *The muon component of gamma-ray-initiated air showers, Journal of Physics G: Nuclear Physics* **11** (1985), no. 6 L101.

[35] F. Krennrich et al., *VERITAS: the Very Energetic Radiation Imaging Telescope Array System, NAR* **48** (Apr., 2004) 345–349.

[36] A. Abramowski and et al., *Acceleration of petaelectronvolt protons in the Galactic Centre, Nature* **531** (Mar., 2016) 476–479, [arXiv:1603.0773].

[37] J. Cortina, *Status and First Results of the Magic Telescope, APSS* **297** (June, 2005) 245–255, [astro-ph/0407475].

[38] B. Acharya et al., *Introducing the CTA concept, Astroparticle Physics* **43** (2013) 3 – 18. Seeing the High-Energy Universe with the Cherenkov Telescope Array - The Science Explored with the CTA.

[39] B. Bartoli et al., *TeV Gamma-Ray Survey of the Northern Sky Using the ARGO-YBJ Detector, ApJ* **779** (Dec., 2013) 27, [arXiv:1311.3376].

[40] B. Dingus and et al, *Milagro: A TeV gamma-ray monitor of the Northern Hemisphere Sky*, in *American Institute of Physics Conference Series* (M. L. McConnell and J. M. Ryan, eds.), vol. 510 of *American Institute of Physics Conference Series*, pp. 642–645, Apr., 2000.

[41] A. U. Abeysekara and et al, *Sensitivity of the High Altitude Water Cherenkov detector to Sources of Multi-TeV gamma rays, Astroparticle Physics* **50** (2013) 26–32.

[42] A. U. Abeysekara et al., *The HAWC Gamma-Ray Observatory: Design, Calibration and Operation*, in *Proceedings 33rd ICRC*, 2013.

[43] A. U. Abeysekara et al., *Search for TeV Gamma-Ray Emission from Point-like Sources in the Inner Galactic Plane with a Partial Configuration of the HAWC Observatory, The Astrophysical Journal* **817** (2016), no. 1 3.

[44] A. Abeysekara, R. Alfaro, C. Alvarez, et al., *Observation of small-scale anisotropy in the arrival direction distribution of TeV Cosmic Rays with HAWC, ApJ* **796** (2014) 108, [arXiv:1408.4805].

[45] L. G. Sveshnikova, O. N. Strelnikova, and V. S. Ptuskin, *Spectrum and anisotropy of cosmic rays at TeV-PeV-energies and contribution of nearby sources*, *Astroparticle Physics* **50** (Dec., 2013) 33–46, [`arXiv:1301.2028`].

[46] M. Ahlers, *Anomalous Anisotropies of Cosmic Rays from Turbulent Magnetic Fields*, *Physical Review Letters* **112** (Jan., 2014) 021101, [`arXiv:1310.5712`].

[47] P. Scott et al., *Direct constraints on minimal supersymmetry from Fermi-LAT observations of the dwarf galaxy Segue 1*, *Journal of Cosmology and Astroparticle Physics* **2010** (jan, 2010) 031–031.

[48] **The VERITAS collaboration** Collaboration, E. Aliu et al., *VERITAS deep observations of the dwarf spheroidal galaxy Segue 1*, *Phys. Rev. D* **85** (Mar, 2012) 062001.

[49] K. Greisen, *The Extensive Air Showers*, *Prog. Cosmic Ray Phys.* **3** (1956) 1.

[50] K. Kamata and J. Nishimura, *The Lateral and the Angular Structure Functions of Electron Showers* , *Prog. Theor. Phys. Suppl.* **6** (1958) 93–155.

[51] F. Guo and W. G. Mathews, *The Fermi Bubbles. I. Possible Evidence for Recent AGN Jet Activity in the Galaxy*, *The Astrophysical Journal* **756** (sep, 2012) 181.

[52] F. Guo, W. G. Mathews, G. Dobler, and S. P. Oh, *The Fermi Bubbles. II. The*

potential roles of Viscosity and Cosmic-Ray Diffusion in Jet Models, The
Astrophysical Journal **756** (sep, 2012) 182.

[53] R. M. Crocker and F. Aharonian, *Fermi Bubbles: Giant, Multibillion-Year-Old
Reservoirs of Galactic Center Cosmic Rays*, Physical Review Letters **106** (mar,
2011) 101102.

[54] K.-S. Cheng, D. O. Chernyshov, V. A. Dogiel, C.-M. Ko, and W.-H. Ip, *Origin
of the Fermi Bubble*, The Astrophysical Journal **731** (apr, 2011) L17.

[55] G. Mou, F. Yuan, Z. Gan, and M. Sun, *The Accretion Wind Model of the
Fermi Bubbles. II. Radiation*, The Astrophysical Journal **811** (2015) 37.

[56] Y. Fujita, Y. Ohira, and R. Yamazaki, *The Fermi Bubbles as a Scaled-up
Version of Supernova Remnants*, The Astrophysical Journal Letters **775** (2013)
20–5.

[57] Y. Fujita, Y. Ohira, and R. Yamazaki, *A Hadronic-Leptonic Model for the
Fermi Bubbles: Cosmic Rays in the Galactic Halo and Radio Emission*, The
Astrophysical Journal **789** (2014), no. 8pp.

[58] R. Atkins, W. Benbow, D. Berley, et al., *Observation of TeV Gamma Rays
from the Crab Nebula with Milagro Using a New Background Rejection
Technique*, ApJ **595** (October, 2003) 803–811, [`arXiv/astro-ph/0305308`].

[59] K. Gorski, E. Hivon, A. Banday, et al., *HEALPix: A Framework for High-Resolution Discretization and Fast Analysis of Data Distributed on the Sphere*, *ApJ* **622** (April, 2005) 759, [`arXiv/astro-ph/0409513`].

[60] R.-z. Yang, F. Aharonian, and R. Crocker, *The Fermi Bubbles Revisited*, *A&A* **567** (2014) 8, [`arXiv:1402.0403`].

[61] O. Helene, *Upper Limit of Peak Area*, *Nucl. Instrum. Methods Phys. Res.* **212** (July, 1983) 319–322.

[62] V. L. Kashyap, D. A. van Dyk, A. Connors, P. E. Freeman, A. Siemiginowska, J. Xu, and A. Zezas, *On Computing Upper Limits to Source Intensities*, *The Astrophysical Journal* **719** (2010), no. 1 900.

[63] T. Kamae, N. Karlsson, T. Mizuno, et al., *Parameterization of γ, $e^{+/-}$, and Neutrino Spectra Produced by p-p Interaction in Astronomical Environments*, *ApJ* **647** (Aug., 2006) 692–708, [`astro-ph/0605581`].

[64] K. S. Cheng, D. O. Chernyshov, V. A. Dogiel, and C. M. Ko, *Multi-wavelength Emission from the Fermi Bubbles. III. Stocahstic (Fermi) Re-acceleration of Relativistic Electrons emitted by SNRs*, *The Astrophysical Journal* **804** (2015).

[65] M. Ahlers, S. Y. BenZvi, P. Desiati, et al., *A New Maximum-likelihood Technique for Reconstructing Cosmic-Ray Anisotropy at All Angular Scales*, *The Astrophysical Journal* **823** (2016), no. 1 10.

[66] V. L. Ginzburg and S. I. Syrovatskii, *The Origin of Cosmic Rays.* Springer, 1964.

[67] F. Aharonian, J. Buckley, T. Kifune, and G. Sinnis, *High energy astrophysics with ground-based gamma ray detectors*, *Reports on Progress in Physics* **71** (2008), no. 9 096901.

[68] J. Binney and M. Merrifield, *Galactic Astronomy* . Princenton series, 1998.

[69] S. Kelner, F. Aharonian, and V. Bugayov, *Energy spectra of gamma rays, electrons, and neutrinos produced at proton-proton interactions in the very high energy regime*, *Phys. Rev. D* (2006).

[70] E. F. Schlafly, G. Green, D. P. Finkbeiner, et al., *A Large Catalog of Accurate Distances to Molecular Clouds from PS1 Photometry*, *ApJ* **786** (2014), no. 1 29.

[71] T. M. Dame, H. Ungerechts, R. S. Cohen, et al., *A composite CO survey of the entire Milky Way*, *ApJ* **322** (Nov., 1987) 706–720.

[72] P. A. R. Ade et al., *Planck Intermediate Results.*, *A&A* **554** (2013) A139, [arXiv:1208.5483].

[73] **HAWC** Collaboration, A. Smith, *HAWC: Design, Operation, Reconstruction and Analysis*, in *Proc. 34th ICRC*, (The Hague, The Netherlands), August, 2015.

[74] S. Wilks, *The Large-Sample Distribution of the Likelihood Ratio for Testing Composite Hypotheses, Ann. Math. Statist.* **9** (1938) 60–62.

[75] A. A. Abdo, B. Allen, T. Aune, et al., *A Measurement of the Spatial Distribution of Diffuse TeV Gamma-Ray Emission from the Galactic Plane with Milagro, ApJ* **688** (2008) 1078–1083.

[76] A. E. Vladimirov, S. W. Digel, G. Johannesson, et al., *GALPROP WebRun: An internet-based service for calculating galactic cosmic ray propagation and associated photon emissions, Elsevier Computer Physics Communications* **182** (2011) 1156–1161.

[77] G. Dobler, *A Last Look at the Microwave Haze/Bubbles with WMAP, The Astrophysical Journal* **750** (2012), no. 1 17.

[78] C. Lunardini and S. Razzaque, *High Energy Neutrinos from the Fermi Bubbles,*
.

[79] M. Amenomori and others., *Search for steady emission of 10-TeV gamma rays from the Crab Nebula, Cygnus X-3, and Hercules X-1 using the Tibet air shower array, Phys. Rev. Lett.* **69** (Oct, 1992) 2468–2471.

[80] e. a. R. Becker-Szendy, *Calibration of the IMB detector, NIM* (1995).

[81] A. W. Strong, J. B. G. M. Bloemen, T. M. Dame, et al., *The radial distribution of galactic gamma rays. IV - The whole galaxy, AAP* **207** (Dec., 1988) 1–15.

[82] B. A. Wilson, T. M. Dame, M. R. W. Masheder, and P. Thaddeus, *A uniform CO survey of the molecular clouds in Orion and Monoceros, AAP* **430** (Feb., 2005) 523–539, [`astro-ph/0411089`].

Appendix A

Figure Copyright Permissions

A.1 Figure 1.1

Image credit: NASA. Public domain.Retrieved from : `http://imagine.gsfc.nasa.gov/science/toolbox/emspectrum1.html`

A.2 Figure 1.6

Image credit: NASA. Public domain. Retrieved from: `http://apod.nasa.gov/apod/ap091025.html`

A.3 Figure 2.5

Image credit: Milagro Collaboration.

A.4 Figure 4.6

Image credit: Co-authored with Hao Zhou. From [5]

A.5 Figure 4.8

Image credit: Co-authored with Hao Zhou. From [5]

A.6 Figure 5.1

Image credit: NASA/DOE/Fermi LAT/D. Finkbeiner et al. Public domain. Retrieved from `https://www.nasa.gov/mission_pages/GLAST/news/new-structure.html`